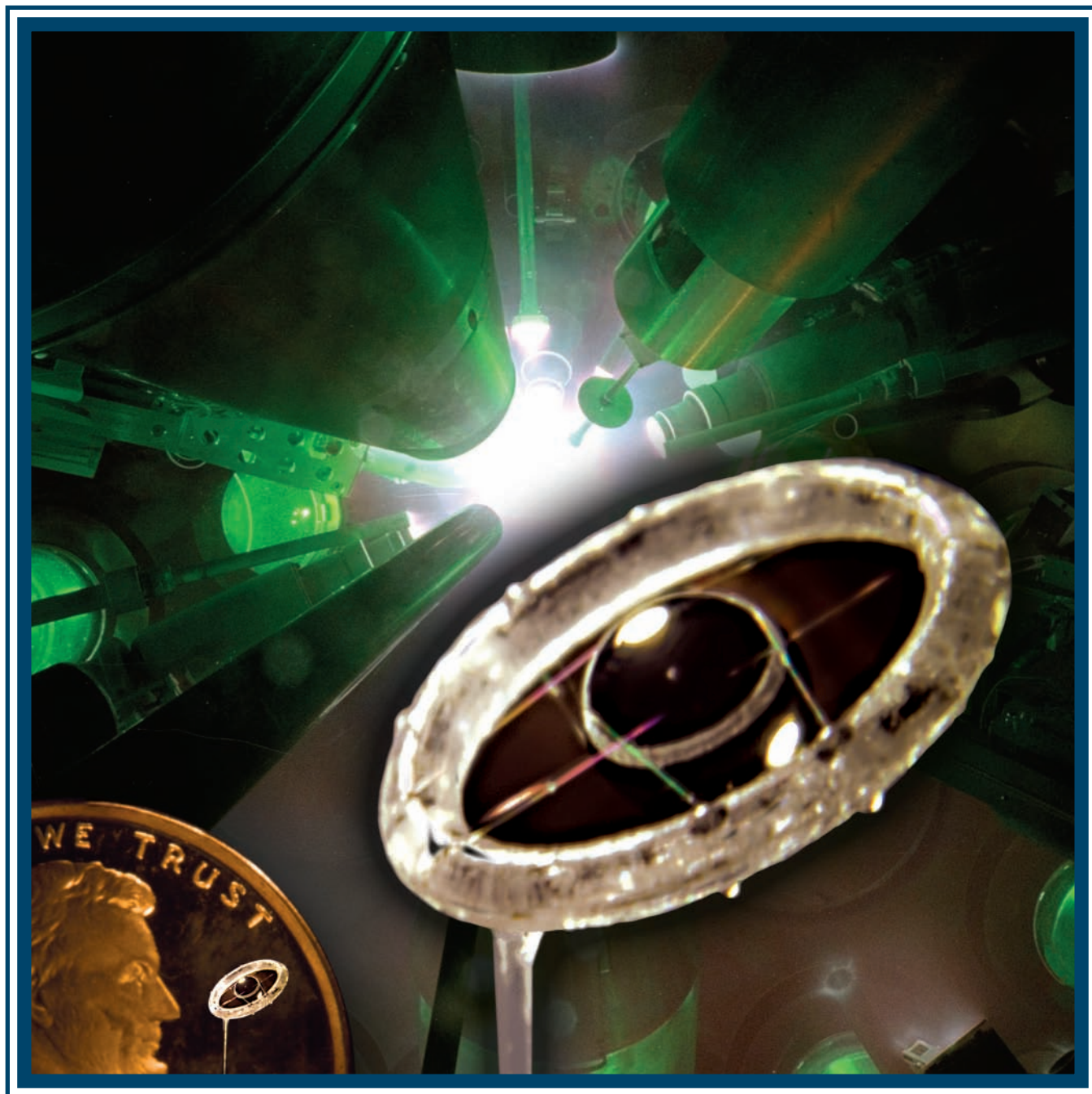


# LLE Review

## Quarterly Report





## About the Cover:

Polar direct drive (PDD) shows promise for achieving direct-drive ignition while the National Ignition Facility is in its initial indirect-drive configuration. The front cover shows a photograph of a Saturn target comprising a fusion-fuel-containing capsule surrounded by a ring. Eight spider silk strands position the capsule at the center of the ring. The entire target is compared with a penny in the lower left-hand corner. The plasma formed around the low-atomic-number ring refracts the illuminating beams near the equator and permits time-dependent tuning of the capsule drive uniformity. Both experiment and theory suggest that Saturn targets can be tuned to permit highly symmetric PDD implosions.

This report was prepared as an account of work conducted by the Laboratory for Laser Energetics and sponsored by New York State Energy Research and Development Authority, the University of Rochester, the U.S. Department of Energy, and other agencies. Neither the above named sponsors, nor any of their employees, makes any warranty, expressed or implied, or assumes any legal liability or responsibility for the accuracy, completeness, or usefulness of any information, apparatus, product, or process disclosed, or represents that its use would not infringe privately owned rights. Reference herein to any specific commercial product, process, or service by trade name, mark, manufacturer, or otherwise, does not necessarily constitute or imply its endorsement, recommendation, or favoring by

the United States Government or any agency thereof or any other sponsor. Results reported in the LLE Review should not be taken as necessarily final results as they represent active research. The views and opinions of authors expressed herein do not necessarily state or reflect those of any of the above sponsoring entities.

The work described in this volume includes current research at the Laboratory for Laser Energetics, which is supported by New York State Energy Research and Development Authority, the University of Rochester, the U.S. Department of Energy Office of Inertial Confinement Fusion under Cooperative Agreement No. DE-FC52-92SF19460, and other agencies.

Printed in the United States of America  
Available from  
National Technical Information Services  
U.S. Department of Commerce  
5285 Port Royal Road  
Springfield, VA 22161

Price codes: Printed Copy A04  
Microfiche A01

For questions or comments, contact Walter T. Shmayda, *Editor*, Laboratory for Laser Energetics, 250 East River Road, Rochester, NY 14623-1299, (585) 275-5769.

Worldwide-Web Home Page: <http://www.lle.rochester.edu/>

# LLE Review

## Quarterly Report



### Contents

In Brief .....	iii
The Saturn Target for Polar Direct Drive on the National Ignition Facility .....	61
Polar Direct Drive—Proof-of-Principle Experiments on OMEGA and Prospects for Ignition on the National Ignition Facility .....	67
Direct-Drive, Cryogenic Target Implosions on OMEGA .....	78
Stopping, Straggling, and Blooming of Directed Energetic Electrons in Hydrogenic Plasmas .....	87
Multidimensional Analysis of Direct-Drive, Plastic-Shell Implosions on OMEGA .....	92
Effects of Temporal Density Variation and Convergent Geometry on Nonlinear Bubble Evolution in Classical Rayleigh–Taylor Instability .....	104
Publications and Conference Presentations	



## In Brief

This volume of the LLE Review, covering January–March 2005, features, in the first two articles, recent investigations of the new “Saturn” target design concept for use in polar direct drive for the National Ignition Facility. In the first article (p. 61), R. S. Craxton and D.W. Jacobs-Perkins discuss a new target design concept that is proposed for direct-drive implosions on National Ignition Facility (NIF) while the facility is in its initial, indirect-drive configuration. The concept differs from earlier polar-direct-drive designs by adding a low- $Z$  ring around the capsule equator. Refraction in the plasma formed around this ring permits time-dependent tuning of the capsule drive uniformity. An optimized simulation shows an implosion-velocity nonuniformity at the end of the laser pulse of  $\sim 1\%$  rms for a cryogenic DT shell, enhancing the prospects for an early direct-drive ignition demonstration on the NIF.

In the second article (p. 67), R. S. Craxton, F. J. Marshall, M. J. Bonino, R. Epstein, P. W. McKenty, S. Skupsky, J. A. Delettrez, I. V. Igumenshchev, D. W. Jacobs-Perkins, J. P. Knauer, J. A. Marozas, P. B. Radha, and W. Seka report the results for proof-of-principle, polar-direct-drive (PDD) experiments on OMEGA and prospects for ignition on the National Ignition Facility. Experiments that have been carried out using 40 repointed beams of the 60-beam OMEGA laser system to approximate the NIF PDD configuration. Backlit x-ray framing-camera images of  $D_2$ -filled spherical CH capsules show a characteristic nonuniformity pattern that is in close agreement with predictions. Saturn targets increase the drive on the equator, suggesting that highly symmetric PDD implosions may be possible with appropriate tuning. Two-dimensional simulations reproduced the approximately threefold reduction in yield found for the non-Saturn PDD capsules. Preliminary simulations for a NIF Saturn design predict a high gain close to the 1-D prediction. These results increase the prospects of obtaining direct-drive ignition with the initial NIF configuration.

Additional research developments presented in this issue include the following:

- F. J. Marshall, R. S. Craxton, J. A. Delettrez, D. H. Edgell, L. M. Elasky, R. Epstein, V. Yu. Glebov, V. N. Goncharov, D. R. Harding, R. Janezic, R. L. Keck, J. D. Kilkenny, J. P. Knauer, S. J. Loucks, L. D. Lund, R. L. McCrory, P. W. McKenty, D. D. Meyerhofer, P. B. Radha, S. P. Regan, T. C. Sangster, W. Seka, V. A. Smalyuk, J. M. Soures, C. Stoeckl, and S. Skupsky along with J. A. Frenje, C. K. Li, R. D. Petrasso, and F. H. Séguin of the Plasma Science and Fusion Center of MIT (p. 78) discuss direct-drive, spherical, cryogenic,  $D_2$ -filled capsules that are illuminated using the 60-beam OMEGA laser system. The targets are energy scaled from the baseline ignition design developed for the National Ignition Facility. Thin-walled ( $\sim 4\text{-}\mu\text{m}$ ),  $\sim 860\text{-}\mu\text{m}$ -diam deuterated (CD) polymer shells are permeation filled with  $D_2$  gas and cooled to the triple point ( $\sim 18.7\text{ K}$ ). Cryogenic ice layers with a uniformity of  $\sim 2\text{-}\mu\text{m}$  rms are formed and maintained. The targets are imploded with high-contrast pulse shapes using full single-beam smoothing (1-THz bandwidth, two-dimensional smoothing by spectral dispersion with polarization smoothing) to study the effects of the acceleration- and deceleration-phase Rayleigh–Taylor growth on target performance. Two-dimensional simulations show good agreement with experimental observations. Scattered-light and neutron-burn-history measurements are consistent with predicted absorption and hydrodynamic coupling calculations. Time-resolved and static x-ray images show the progress of the imploding shell, shape, and temperature of the stagnating core. Particle-based instruments measure the fusion yield and rate, the

ion temperature in the core, and the fuel areal density at the time of neutron production. These experiments have produced fuel areal densities up to  $\sim 100 \text{ mg/cm}^2$ , primary neutron yields  $\sim 4 \times 10^{10}$ , and secondary neutron yields 1% to 2% of the primary yield. These results validate the hydrocode predictions for the direct-drive, ignition-point design, giving increasing confidence in the direct-drive approach to inertial confinement fusion ignition.

- C. K. Li and R. D. Petrasso, of the Plasma Science and Fusion Center at MIT (p. 87), discuss the interaction of directed energetic electrons with hydrogenic plasmas analytically modeled from fundamental principles. The effects of stopping, straggling, and beam blooming are rigorously treated in a unified approach for the first time. Enhanced energy deposition, which occurs in the latter portion of beam penetration, is inextricably linked to straggling and beam blooming. Both effects asymptotically scale with the square root of the linear penetration. Eventually they dominate over all other sources of beam divergence; therefore, understanding their effects is critical for evaluating the requirements of fast ignition.
- P. B. Radha, T. J. B. Collins, J. A. Delettrez, R. Epstein, V. Yu. Glebov, V. N. Goncharov, R. L. Keck, J. P. Knauer, J. A. Marozas, F. J. Marshall, R. L. McCrory, P. W. McKenty, D. D. Meyerhofer, S. P. Regan, T. C. Sangster, W. Seka, S. Skupsky, and C. Stoeckl along with Y. Elbaz, D. Shvarts, Y. Srebro of the Negev Research Center (p. 92) provide a multidimensional analysis of direct-drive, plastic-shell implosions on OMEGA. Direct-drive, plastic-shells imploded on the OMEGA laser system with a 1-ns square pulse are simulated using the multidimensional hydrodynamic code *DRACO*. Yield degradation in “thin” shells is primarily caused by shell breakup during the acceleration phase due to short-wavelength ( $\ell > 50$ , where  $\ell$  is the Legendre mode number) perturbation growth, whereas “thick” shell performance is influenced primarily by long and intermediate modes ( $\ell \leq 50$ ). Simulation yields, temporal history of neutron production, areal densities, and x-ray images of the core compare well with experimental observations. In particular, the thin-shell neutron production history falls off less steeply than one-dimensional predictions due to shell-breakup induced under compression and delayed stagnation. Thicker, more-stable shells show burn truncation due to instability-induced mass flow into the colder bubbles. Estimates of small-scale mix indicate that turbulent mixing does not influence primary neutron yields.
- V. N. Goncharov and D. Li (p. 104) present the effects of temporal density variations and convergent geometry on nonlinear bubble evolution in classical Rayleigh–Taylor instability. Effects of temporal density variation and spherical convergence on the nonlinear bubble evolution of single mode, classical Rayleigh–Taylor instability are studied using an analytical model based on Layzer’s theory. When the temporal density variation is included, the bubble amplitude in the planar geometry asymptotes to a fixed value that depends on the Layzer bubble velocity, the fluid density, and a factor to account for the two- and three-dimensional geometries. The model can be applied to spherical geometries to predict the nonlinear bubble amplitude.

Walter T. Shmayda  
*Editor*

# The Saturn Target for Polar Direct Drive on the National Ignition Facility

Direct-drive illumination plays a significant role in plans to achieve ignition on the National Ignition Facility (NIF).<sup>1</sup> Ignition requires the uniform implosion of a fuel capsule containing a deuterium–tritium mixture with intense laser beams, using either direct laser illumination of the capsule<sup>2</sup> or indirect drive,<sup>3</sup> in which laser beams focused into a hohlraum generate x rays to drive the capsule. The baseline NIF target chamber geometry requires that all the NIF beams be incident through 48 beam ports, known as the “indirect-drive” ports, located in rings with angles varying from 23.5° to 50° with respect to the vertical (pole). Additional beam ports near the equator, at an angle of 77.45°, allow symmetric direct-drive illumination to be accommodated at a later time by rerouting half of the beams to these ports.<sup>4</sup> Considerable interest has been stimulated by the recent reconsideration<sup>5–8</sup> of direct drive using the indirect-drive ports with the beams repointed toward the equator, a concept once dismissed as ineffective because of the difficulty of ensuring uniformity on the imploding critical surface<sup>9</sup> and now known as polar direct drive (PDD).<sup>6</sup> PDD may allow direct-drive ignition and possibly high gain to be achieved on the NIF many years earlier than would otherwise be possible.

This article reports on a new PDD target design concept that promises to improve the drive uniformity on the capsule compared with the previous (“standard PDD”) designs of Refs. 6–8. The new “Saturn” design, whose distinctive feature is a low-Z ring placed in the equatorial plane of the capsule (Fig. 102.1), is applied to the “all-DT” design of Refs. 10 and 11. The Saturn design can result in a DT shell that is imploding at the end of the laser pulse with a velocity uniform to a little over 1% (rms), close to the uniformity expected for the “symmetric” design that uses the direct-drive ports with all beams pointed to the capsule center.<sup>11</sup>

The next article (“Polar Direct Drive—Proof-of-Principle Experiments on OMEGA and Prospects for Ignition on the National Ignition Facility,” which begins on p. 67) describes PDD experiments that validate both hydrodynamic PDD simulations and the Saturn concept. It also presents a simulation of the NIF Saturn design that results in high gain close to the prediction from an ideal one-dimensional calculation. These results increase the prospects of obtaining direct-drive ignition with the initial NIF configuration.

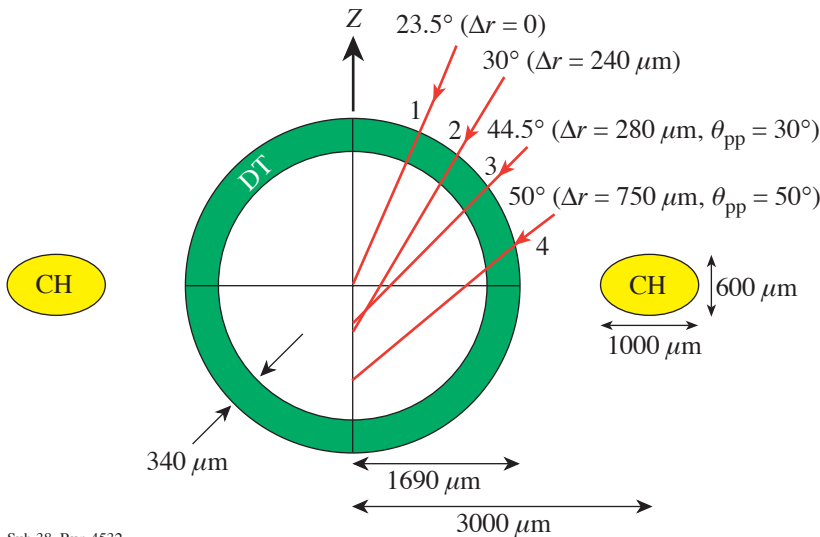


Figure 102.1  
Vertical cross section of a Saturn target for direct drive on the NIF. The capsule (the “all-DT” design of Ref. 11) is a 340- $\mu\text{m}$  layer of cryogenic DT supported in a thin (few- $\mu\text{m}$ ) plastic shell. It is irradiated using the four rings of indirect-drive ports in each hemisphere and the indicated repointings. The capsule is surrounded by a low-Z (CH) ring whose plasma provides time-dependent pointing correction for ring-4 beams.

Sub 38, Run 4532  
TC6654

The primary limitation on the uniformity attainable with standard PDD arises because extra laser power needs to be focused near the equator to compensate for the oblique angle of incidence, but the radius of the critical surface (near which most absorption occurs) decreases significantly during the laser pulse. Since the NIF laser beams cannot be dynamically repointed, two methods have hitherto been proposed to minimize this effect: careful optimization of the beam pointings<sup>6-8</sup> and the use of different pulse shapes for the different rings of beams.<sup>6</sup> The essence of the Saturn design is that a plasma forms around the low-Z ring from laser rays refracted from the capsule plasma and from rays on the edges of ring-4 beams (those incident at 50° in Fig. 102.1) that clip the low-Z ring. The ring plasma has little impact on the capsule irradiation pattern at early times, but later expands into the path of a significant portion of ring-4 rays, deflecting them to strike the imploding critical surface near the equator. Optimum designs match the expansion of the ring plasma to the implosion of the capsule plasma.

Figure 102.1 gives the main parameters of the Saturn design. Three of the four rings of beams in each hemisphere (the lower-hemisphere beams are not shown) are repointed toward the equator with the specified distances  $\Delta r$  measured perpendicular to the beam axes. Rings 3 and 4 use “elliptical phase plates,” whose focal spot is shortened in the vertical direction by a factor of  $\cos \theta_{pp}$ . Prior to this shortening, all beams have super-Gaussian target-plane spatial shapes with the intensity proportional to  $\exp-(r/r_0)^{2.5}$  with  $r_0 = 1200 \mu\text{m}$ . The capsule is a thick shell (340  $\mu\text{m}$ ) of cryogenic DT ice contained within a thin (few- $\mu\text{m}$ ) plastic shell of 1690- $\mu\text{m}$  outer radius.<sup>11</sup> The low-Z ring, made of CH to minimize radiation preheat, has a major radius  $R_{\text{major}}$  of 3000  $\mu\text{m}$  and an elliptical cross section. While the parameters listed in Fig. 102.1 were selected as a result of numerous two-dimensional (2-D) simulations, improvements are likely because of the large range of possible parametric variations.

The Saturn design is compared with standard PDD and symmetric designs obtained using similar optimizations and the same super-Gaussian profiles. The pointings used for standard PDD are  $\Delta r = 100, 290, 380,$  and  $750 \mu\text{m}$ , respectively, for rings 1-4 and  $\theta_{pp} = 30^\circ$  and  $60^\circ$ , respectively, for rings 3 and 4 (as in Ref. 8).

The target is irradiated by the incident laser temporal pulse shape taken from Ref. 11 and shown in Fig. 102.2 as the upper curve. The total incident energy is 1.53 MJ, less than the nominal total NIF energy<sup>1</sup> of 1.8 MJ. All beams have the same power history, maximizing the available on-target energy. The

other curves in Fig. 102.2 give the absorbed laser power for the three cases. The overall absorption for standard PDD (63%) is only slightly less than the 66% of the symmetric case because the elliptical phase plates compensate for the absorption loss of the repointed beams. The inset in Fig. 102.2 shows the elliptical 10% intensity contour (the outer ellipse) in the target plane of a ring-4 beam pointed 750  $\mu\text{m}$  below the target center together with the initial and final critical surface radii. The Saturn capsule absorbs slightly more (70%), and just under half of the energy refracted from the capsule is absorbed in the CH ring (bottom curve).

The simulations reported here used the 2-D Eulerian hydrodynamics code *SAGE*, which includes fully self-consistent, 3-D laser ray tracing.<sup>12</sup> Each of the eight rings (four per hemisphere) is represented by a single beam whose incoming cross section is broken into a grid of  $\sim 1000$  rays (shown schematically in the inset in Fig. 102.2). Each ray is traced through an  $(x,y,z)$  coordinate system, with  $z$  vertical, and the energy at each step is deposited by inverse bremsstrahlung onto the spherical  $(r,\theta)$  simulation grid at radius  $r = (x^2 + y^2)^{1/2}$ . This

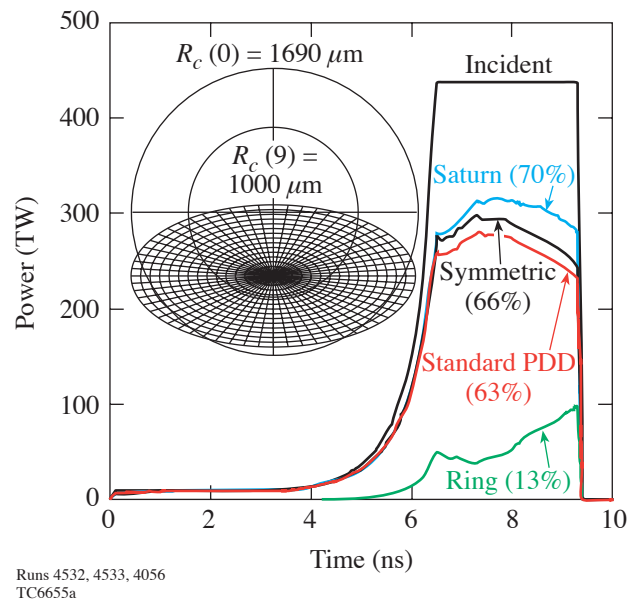


Figure 102.2 Incident and capsule-absorbed laser power as a function of time for three cases: “symmetric,” “standard PDD,” and Saturn. The bottom curve applies to the ring of the Saturn target. The time-integrated absorption fractions are given in parentheses. Inset: The critical surface of the capsule at 0 and 9 ns (radii  $R_c = 1690$  and  $1000 \mu\text{m}$ , respectively) viewed along the axis of the ring-4 beam for the standard-PDD design, together with the elliptical far field (out to the 10% intensity contour) centered 750  $\mu\text{m}$  below the target center. The grid indicates starting points for the simulation ray trace.

is equivalent to averaging the deposited energy in the azimuthal ( $\phi$ ) direction. The azimuthal variations due to the finite number of beams in each NIF ring are expected to be smaller than the variations in  $\theta$  due to the PDD geometry.

Typical plots of density contours and ray trajectories [projected into the  $(r, \theta)$  plane] are shown in Fig. 102.3 for the Saturn and standard-PDD cases, at 5.8 ns (close to the time that the initial shock reaches the inner DT surface) and at 9 ns

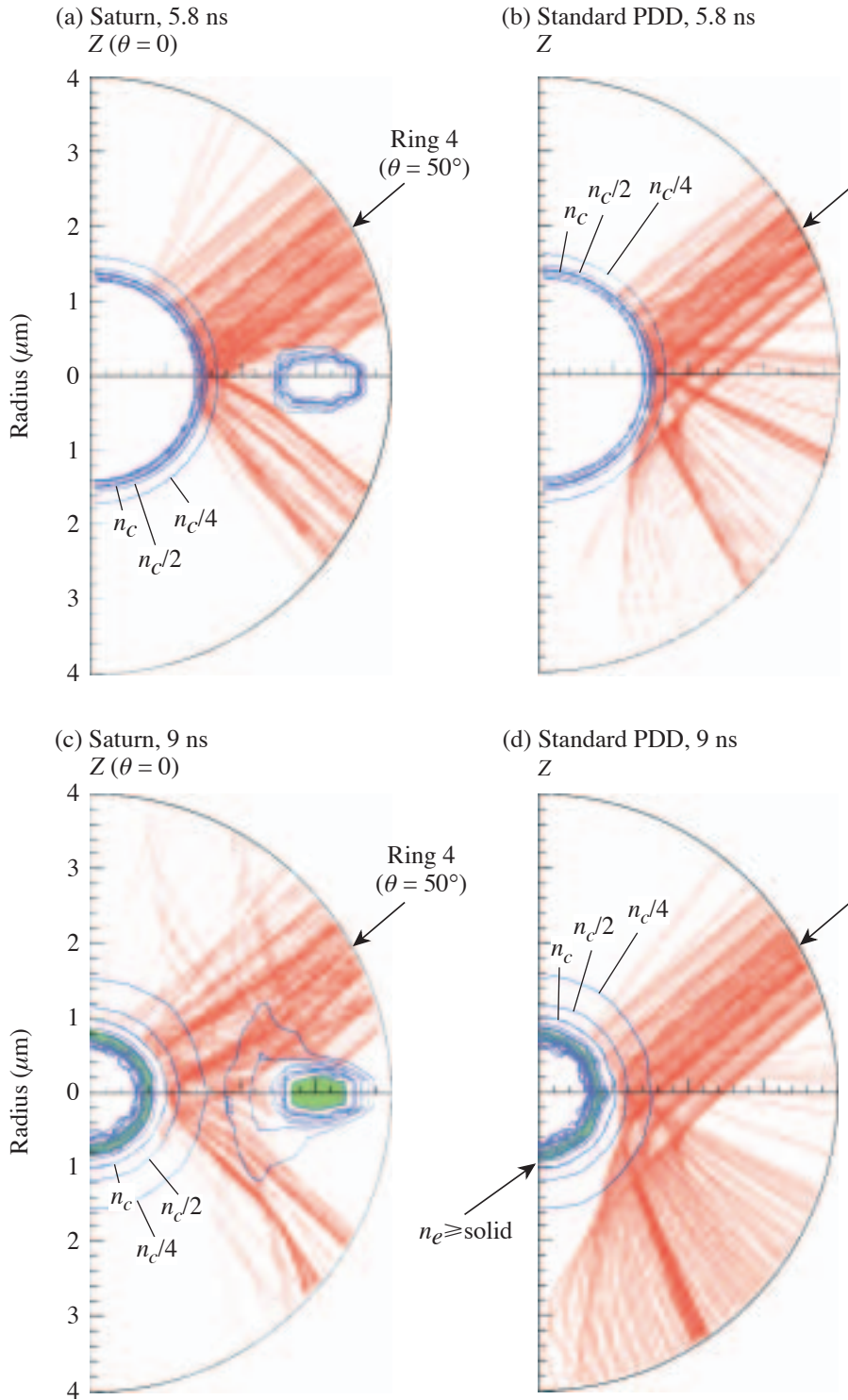


Figure 102.3  
Electron-density contours (some of which are labeled as fractions of the critical electron density  $n_c$ ) and a representative subset of ring-4 ray trajectories projected into the  $(r, z)$  plane for a Saturn target and a standard PDD target, at the time of shock breakout (5.8 ns) and at the end of the laser pulse (9 ns). In the Saturn design, the central group of rays refract in the ring plasma at the later time (c) toward the capsule equator. The shaded areas at 9 ns represent material above solid density.

Run 4532=4341, 4056  
TC6848

(roughly the end of the laser pulse). For clarity, only a small fraction of the ring-4 rays are shown. At 5.8 ns, the plasma forming around the CH ring is not large enough to significantly deflect the central rays (marked with arrows). At 9 ns, however, significant refraction of the central group of rays toward the capsule equator is evident in the Saturn case, while these rays pass significantly below the equator in the standard-PDD case. An additional effect included in the simulations is tamping of the blowoff by the CH ring that may also enhance the pressure near the equator.

The deviations of the center-of-mass radius and radial velocity ( $V_r$ ) of the imploding shell at 9 ns are shown in Fig. 102.4 for the three cases. The standard-PDD case shows significant structure, in particular a large radius and small velocity near the equator. The Saturn case reduces the rms velocity variation to 1.3%, close to the 1.0% predicted for the symmetric case. A uniform  $V_r$  is critical to a uniform implosion, and the target designs were chosen to minimize the rms of this quantity. The quoted rms values are probably upper bounds since the simulations, which should be symmetric about  $\theta = 90^\circ$ , include some numerical noise. The Saturn-design  $V_r$  nonuniformity is dominated by Legendre modes  $\ell = 2$  and 4 (1.1% in these modes), with the other 0.2% attributable to noise. The predominantly low- $\ell$  content in the Saturn case provides a significant advantage compared with the standard-PDD case, as the all-DT capsule design is more tolerant of low- $\ell$  modes.<sup>11</sup> Figure 102.4 also shows that the DT shell in the Saturn case moves approximately the same distance and acquires the same velocity as for the symmetric target, indicating (consistently with Fig. 102.2) that there is no energy penalty associated with the Saturn design even though the laser energy, incident more obliquely, is on average absorbed farther from the critical surface.

The standard-PDD pointings provide excessive drive on the equator at early times to compensate for the reduced drive at later times. This produces increased pressure gradients and motion in the  $\theta$  direction. The rms  $V_r$  is 7.2% at 5.8 ns, compared with 2.5% for Saturn, and the rms  $V_\theta$  at 9 ns is  $1.4 \times 10^6$  cm/s, compared with  $9 \times 10^5$  cm/s ( $\sim 3\%$  of  $V_r$ ) for Saturn. The Saturn design thus enables slightly smaller repointings to be used for rings 1–3 to provide better early time uniformity. The simulations all used a flux limiter<sup>13</sup>  $f$  of 0.06, broadly consistent with the observed absorption and drive in current OMEGA experiments.<sup>14</sup> The parameters  $\Delta r$  and  $\theta_{pp}$  needed to optimize the PDD designs are insensitive to  $f$ .

Some simulation results of the parametric sensitivities of the designs are shown in Fig. 102.5, which gives the rms center-of-mass radius ( $\Delta R_{rms}$ ) and velocity ( $\Delta V_{rms}$ ) variations as functions of the pointing error of the most-sensitive laser ring for all three cases and as functions of  $R_{major}$  for the Saturn design. As in Fig. 102.4, the Saturn performance is close to that of the symmetric case. The NIF single-beam pointing tolerance of  $50\text{-}\mu\text{m}$  rms<sup>15</sup> should be adequate in all cases, especially as the calculations make the pessimistic assumption that all beams in the ring are displaced in unison. Figures 102.5(c) and 102.5(d) point to an optimum  $R_{major}$  of  $3100 \pm 100 \mu\text{m}$ . As the ring is moved away from the capsule,  $\Delta V_{rms}$  increases because fewer rays intersect the ring plasma. As the ring is moved toward the capsule,  $\Delta V_{rms}$  increases dramatically due to the capsule equator becoming shadowed by the ring. Adjustment of the ring parameters provides a means for tuning the time-dependent drive symmetry of different capsule designs. Such tuning may also be required because the ring plasma, whose rate of formation depends in part on the energy near the beam edges, may evolve differently than predicted here.

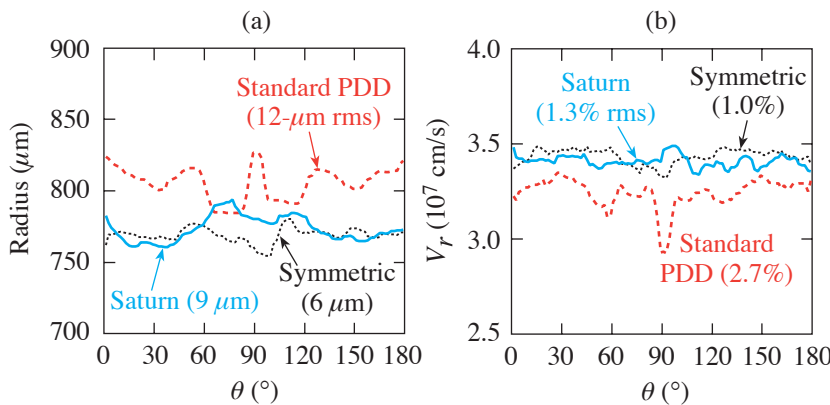


Figure 102.4  
(a) Center-of-mass radius and (b) radial velocity ( $V_r$ ) as a function of angle  $\theta$  from the vertical for the three cases — symmetric, standard PDD, and Saturn — at the end of the laser pulse (9 ns).

Runs 4533, 4056, 4532=4341  
TC6656

From other sensitivity studies, the positioning tolerances of (a) the capsule with respect to the target chamber center and (b) the CH ring with respect to the capsule in the  $z$  direction are critical: preliminary results suggest that these should each be less than  $50\ \mu\text{m}$ , preferably by a factor of 2. Capsule-mounting schemes taking advantage of the Saturn design must provide accurate centering of the capsule within the ring.

The optimization process that led to the Saturn design started with the investigation of target-plane profiles of the form  $I(r) \propto \exp-(r/r_0)^n$  for the symmetric case. Obtaining a smooth overlap of deposited energy profiles from neighboring laser rings for all critical-surface radii between the initial and final becomes hard when  $n$  increases above 2.5, as the edge of the profile steepens. For smaller  $n$ , an energy penalty results from rays near the edge of the beam missing the target. For  $r_0 < 1200\ \mu\text{m}$ , nonuniformities result from the deposition being too localized, while for larger  $r_0$ , the uniformity remains good but energy is lost. For the PDD designs, the same  $n$  and  $r_0$  are used on the assumption that this will provide comparable azimuthal uniformity to the symmetric case. The values of  $\Delta r$  and  $\theta_{pp}$  are chosen to spread the deposited laser energy as uniformly as possible around the capsule surface. The CH-ring

parameters are chosen on the basis of surveys such as shown in Fig. 102.5.

Experimental investigations of PDD on the OMEGA laser system and extended simulations of the Saturn design to examine the implosion physics beyond the end of the laser pulse are reported in the next article and in Ref. 16. Preliminary results demonstrate that the Saturn ring does indeed increase the drive on the equator. Issues for future investigation include characterization of the evolution and azimuthal symmetry of the Saturn ring plasma.

In conclusion, the Saturn concept will enable direct-drive implosions to be carried out on the NIF, using only the indirect-drive ports, with a uniformity approaching that of the symmetric configuration. A low- $Z$  ring placed around the capsule provides time-dependent correction of critical laser ray trajectories to ensure adequate drive on the capsule equator at all times. Preliminary parameter surveys indicate that the tolerances necessary to ensure this high level of uniformity are reasonable. The prospects for an early ignition demonstration on the NIF using direct drive are thus greatly enhanced.

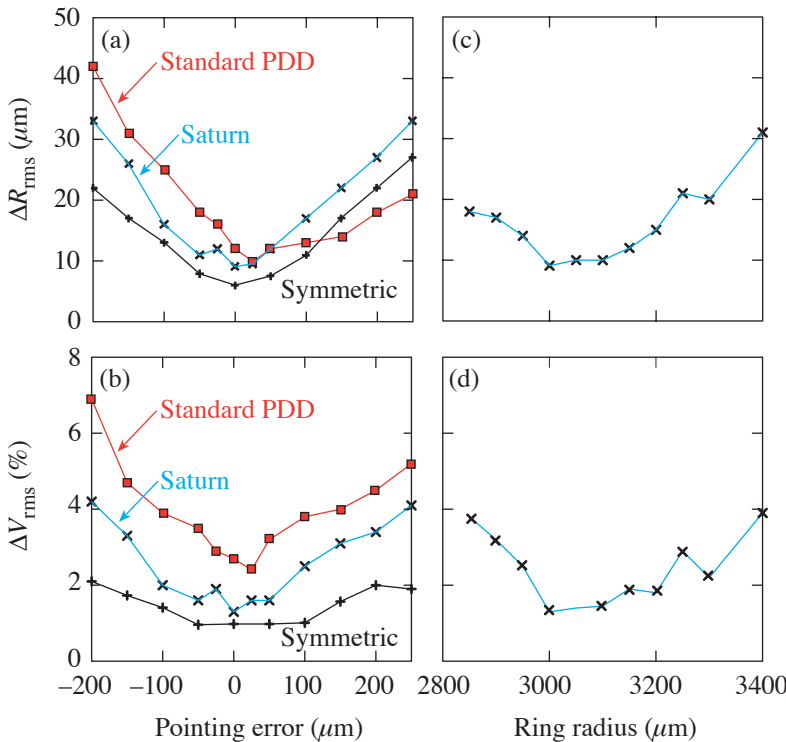


Figure 102.5  
Dependence of (a) the rms center-of-mass radius variation  $\Delta R_{\text{rms}}$  and (b) the rms radial velocity variation  $\Delta V_{\text{rms}}$  at 9 ns on the pointing error of the ring of beams with the greatest sensitivity (ring 2 for the symmetric case, ring 4 for the others). The same quantities are plotted against the low- $Z$  ring's major radius in (c) and (d) for the Saturn design. Each symbol corresponds to a 2-D simulation; the thin lines serve only to guide the eye.

Sub 39  
TC6649

## ACKNOWLEDGMENT

This work was supported by the U.S. Department of Energy Office of Inertial Confinement Fusion under Cooperative Agreement No. DE-FC52-92SF19460, the University of Rochester, and the New York State Energy Research and Development Authority. The support of DOE does not constitute an endorsement by DOE of the views expressed in this article.

## REFERENCES

1. E. M. Campbell and W. J. Hogan, *Plasma Phys. Control. Fusion* **41**, B39 (1999).
2. J. Nuckolls *et al.*, *Nature* **239**, 139 (1972).
3. J. D. Lindl, *Inertial Confinement Fusion: The Quest for Ignition and Energy Gain Using Indirect Drive* (Springer-Verlag, New York, 1998), Chap. 6, pp. 61–82.
4. D. Eimerl, J. Rothenberg, M. Key, S. Weber, C. Verdon, S. Skupsky, J. Soures, and S. Craxton, in *First Annual International Conference on Solid State Lasers for Application to Inertial Confinement Fusion*, edited by M. André and H. T. Powell (SPIE, Bellingham, WA, 1995), Vol. 2633, pp. 170–182.
5. J. D. Kilkenny, Laboratory for Laser Energetics, private communication (2002).
6. S. Skupsky, J. A. Marozas, R. S. Craxton, R. Betti, T. J. B. Collins, J. A. Delettrez, V. N. Goncharov, P. W. McKenty, P. B. Radha, T. R. Boehly, J. P. Knauer, F. J. Marshall, D. R. Harding, J. D. Kilkenny, D. D. Meyerhofer, T. C. Sangster, and R. L. McCrory, *Phys. Plasmas* **11**, 2763 (2004).
7. R. S. Craxton, presented at the 33rd Anomalous Absorption Conference, Lake Placid, NY, 22–27 June 2003 (Paper WO3).
8. R. S. Craxton, *Bull. Am. Phys. Soc.* **48**, 56 (2003).
9. D. Eimerl, ed., Lawrence Livermore National Laboratory, Livermore, CA, UCRL-ID-120758 (1995).
10. C. P. Verdon, *Bull. Am. Phys. Soc.* **38**, 2010 (1993).
11. P. W. McKenty, V. N. Goncharov, R. P. J. Town, S. Skupsky, R. Betti, and R. L. McCrory, *Phys. Plasmas* **8**, 2315 (2001).
12. R. S. Craxton and R. L. McCrory, *J. Appl. Phys.* **56**, 108 (1984).
13. R. C. Malone, R. L. McCrory, and R. L. Morse, *Phys. Rev. Lett.* **34**, 721 (1975).
14. J. A. Delettrez, Laboratory for Laser Energetics, private communication (2004).
15. R. A. Zacharias *et al.*, in *Optical Engineering at the Lawrence Livermore National Laboratory II: The National Ignition Facility*, edited by M. A. Lane and C. R. Wuest (SPIE, Bellingham, WA, 2004), Vol. 5341, pp. 168–179.
16. R. S. Craxton, F. J. Marshall, M. Bonino, R. Epstein, P. W. McKenty, S. Skupsky, J. Delettrez, I. V. Igumenshchev, D. W. Jacobs-Perkins, J. P. Knauer, J. A. Marozas, P. B. Radha, and W. Seka, “Polar Direct Drive—Proof-of-Principle Experiments on OMEGA and Prospects for Ignition on the NIF,” to be published in *Physics of Plasmas*.

---

# Polar Direct Drive—Proof-of-Principle Experiments on OMEGA and Prospects for Ignition on the National Ignition Facility

## Introduction

This article supports the preceding article (“The Saturn Target for Polar Direct Drive on the National Ignition Facility,” p. 61) by presenting recent experimental and simulation results indicating that ignition may be feasible on the National Ignition Facility (NIF)<sup>1</sup> using polar direct drive (PDD).<sup>2</sup>

Since the recent suggestion<sup>3</sup> that the PDD option be reconsidered on account of the cost and complexity of rerouting half of the NIF beams, a number of two-dimensional (2-D) hydrodynamic PDD simulations have been reported. Simulations<sup>4,5</sup> of the all-DT capsule design of Refs. 6 and 7 were carried out using the hydrodynamics code *SAGE*, which includes fully self-consistent 3-D ray tracing.<sup>8</sup> These simulations used sets of optimized repointings of the four rings of NIF beams and elliptical far-field focal spots for some rings to increase the drive on the capsule equator. Skupsky *et al.*<sup>2</sup> used the 2-D code *DRACO*<sup>9,10</sup> to examine PDD designs for wetted-foam capsules,<sup>11</sup> which are attractive because of increased laser absorption. They concluded that PDD enhances the capability of the NIF to explore ignition conditions and found that the primary cause of gain reduction was the time-dependent drive deficit on the equator due to target compression.<sup>12</sup> The previous article (p. 61) describes simulations of a new “Saturn” target concept for PDD in which a low-*Z* ring is placed around the capsule in the equatorial plane. The plasma produced around the ring (by a combination of light refracted from the capsule and light directly intercepted by the ring) grows so that, at later times, laser rays that would otherwise miss the critical surface in the equatorial region of the capsule are now refracted by the ring plasma to provide stronger irradiation of this region. With appropriately chosen ring dimensions, the capsule can be driven with a uniformity (~1%) approaching that of a symmetrically driven capsule.

The success of PDD on the NIF depends, to a large extent, on the accuracy with which the drive uniformity resulting from proposed laser-beam repointings can be predicted and diagnosed. Two initial series of PDD experiments have been

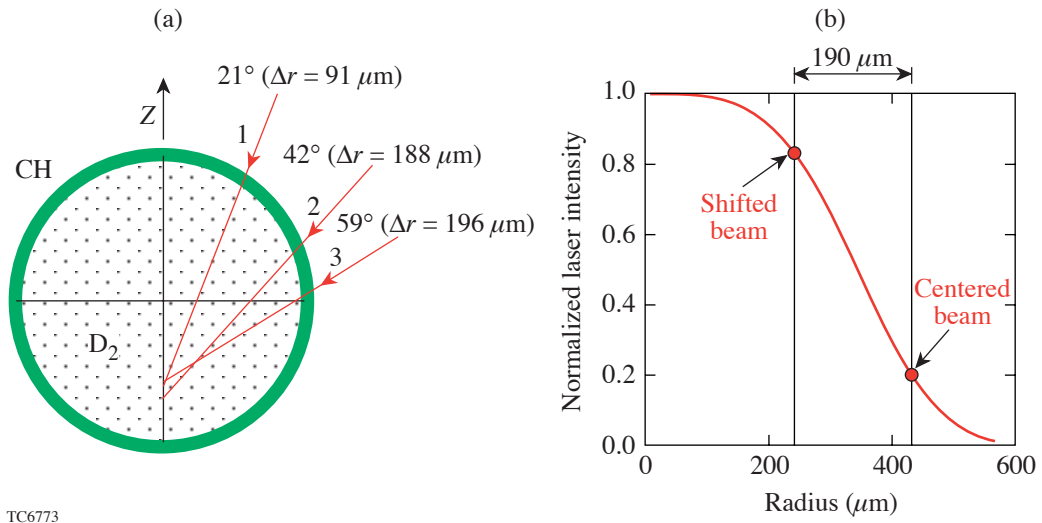
carried out using the 60-beam OMEGA Laser Facility to address these issues. To approximate the NIF irradiation configuration, 40 OMEGA beams are used to irradiate the capsule, with the 20 beams near the equator omitted from the laser drive (some of these beams are used for backlighting).

The optimum repointings for the experiments were calculated on the basis of numerous 2-D *SAGE* simulations for different combinations of these parameters. In every case, the drive was found to be too low on the equator. The optimum repointings minimized the overall rms nonuniformity in the center-of-mass velocity of the imploding shell at the end of the laser pulse, producing a predicted  $\ell = 4$  pattern with the drive low at both the equator and the poles. Both experimental series showed this  $\ell = 4$  pattern with the predicted amplitude, confirming the simulations as well as the pointing accuracy and reproducibility of the OMEGA system.

The low drive on the equator can be understood as follows: Since the central portion of the OMEGA on-target beam profile is fairly flat, the intensity incident from a beam with the largest angle ( $59^\circ$ ) to the vertical is larger at the point on the capsule ( $\theta = 59^\circ$ ) irradiated at normal incidence than at the equator, which sees a flux reduced by  $\cos(31^\circ)$ . Two other factors further reduce the equatorial drive: (a) the absorption falls off as the angle of incidence increases, and (b) once a plasma has formed around the capsule, the energy deposited from obliquely incident rays is spread over a curved path. To provide compensation for all of these factors, the beams aimed at the equator would need more tightly focused spatial profiles (as proposed for the NIF<sup>4,5</sup>).

In the second series of experiments, three Saturn targets were imploded on OMEGA. For these targets, the framed x-ray backlighting results showed a clear  $\ell = 2$  drive nonuniformity, with an enhanced drive at the equator that was greater than predicted. These results are very encouraging and suggest that it should be possible to move some of the beam pointings back toward the poles to remove the  $\ell = 2$  mode.

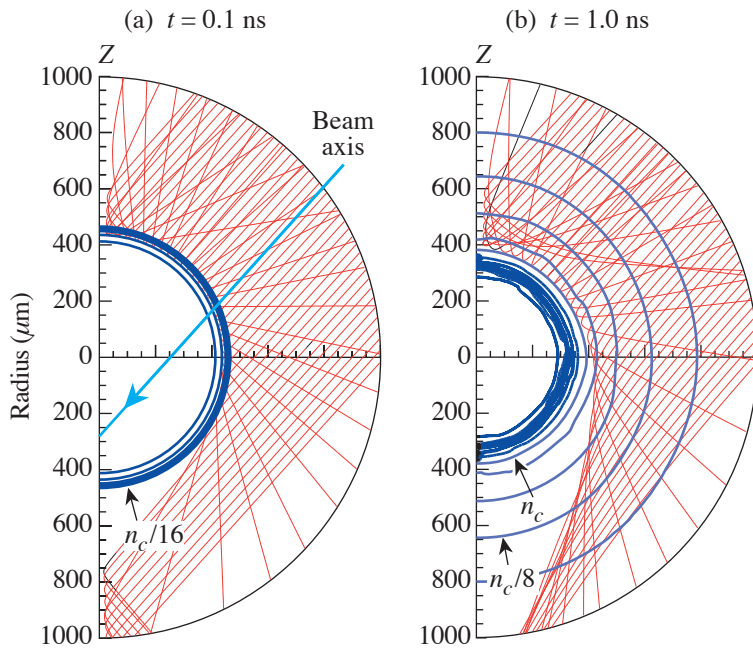




TC6773

Figure 102.7

(a) Repointings  $\Delta r$  used for the three rings of OMEGA laser beams, measured perpendicular to the beam axes. The capsule is a  $20\text{-}\mu\text{m}$ -thick CH shell of  $865\text{-}\mu\text{m}$  diameter filled with 15 atm of  $D_2$ . (b) Target-plane intensity distribution for an OMEGA beam. The solid circles indicate the intensities and radii of rays that can miss the initial target edge for shifted and centered beams.



Run 4187  
TC6525

Figure 102.8

Electron-density contours (heavy lines) and a selection of ring-2 ray trajectories in the plane containing the laser axis and the  $z$  axis (thin lines), (a) near the start and (b) near the end of the laser pulse. The contour spacing is a factor of 2 in density. The energy loss due to PDD is less than might be expected from Fig. 102.7(b) because of absorption in the expanding plasma.

The time dependence of the predicted absorption is quantified in Fig. 102.9. The incident laser pulse is represented as a 1-ns flat pulse with a linear rise and fall, producing a nominal 16 kJ on target (400 J per beam). The absorbed power rises in time as the coronal scale length increases. The standard-PDD target is predicted to absorb 66% of the incident laser energy, compared with 75% for the 1-D (center-pointed) case. This is roughly equivalent to a 10% incident energy reduction, used when the 1-D code *LILAC* simulates the PDD implosions. The curve labeled “1-D” corresponds to this case and is quite close to the standard-PDD curve.

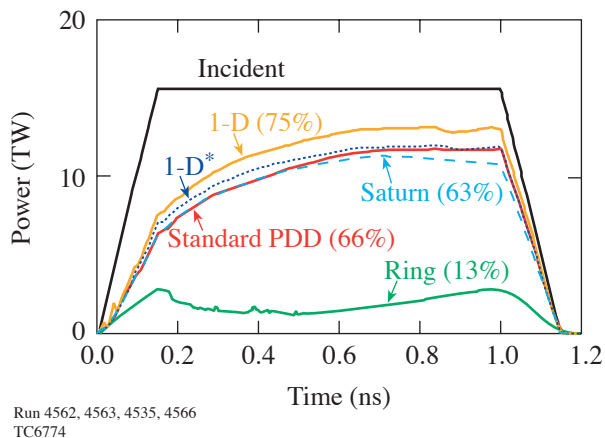


Figure 102.9

Incident and absorbed power as a function of time for several *SAGE* simulations with 16 kJ of incident laser energy, the time-integrated absorption fractions given in parentheses. The curves labeled 1-D are for symmetric irradiation, with 1-D\* indicating a 10% reduction of incident energy. For the Saturn simulation, the upper and lower curves apply to the capsule and ring, respectively.

The highly anisotropic distribution of unabsorbed light predicted for PDD makes it difficult to measure the laser absorption using the small number of scattered-light calorimeters on the OMEGA target chamber, as does the material blowoff from the backlighting targets. A separate absorption experiment was carried out to test the modeling of obliquely incident beams. This was done in a symmetric way by taking advantage of the grouping of the OMEGA beams into 12 pentagonal faces of five beams each.<sup>2</sup> Each beam was repositioned so that its axis intersected a 1600- $\mu\text{m}$ -diam, solid-CH target at the point where the axis of its first or second nearest neighbor would normally intersect. This is illustrated in the inset to Fig. 102.10 for a single move around the group (corresponding to  $\Delta r = 335 \mu\text{m}$ ). Targets were also shot for a double move ( $\Delta r =$

514  $\mu\text{m}$ ). Large targets were used for this experiment to minimize the transmission of laser energy into the opposing beam ports. The absorption fractions determined by a pair of full-aperture backscatter calorimeters, shown in Fig. 102.10, agree very closely with the *SAGE* predictions, providing confidence in the absorption modeling of obliquely incident beams.

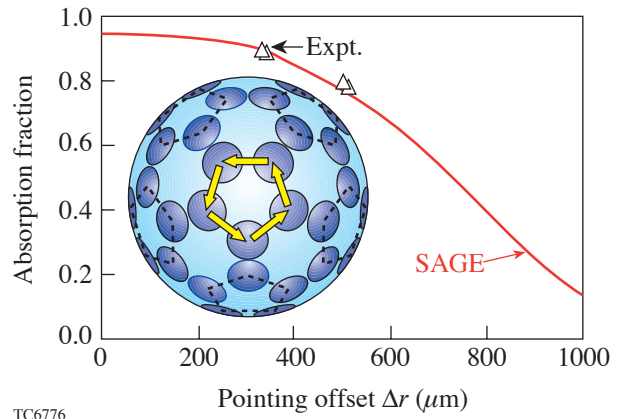


Figure 102.10

Experimental and simulated absorption as a function of pointing offset  $\Delta r$  on large, 1600- $\mu\text{m}$ -diam solid CH targets. Each beam was repositioned either one position (as shown in the inset) or two positions around its pentagonal ring on the OMEGA target chamber to allow the effect of oblique incidence to be studied with the minimum loss of uniformity.

Framed x-ray backlighting was the primary diagnostic used for the implosion experiments. A set of four images at 250-ps intervals, integrated over 50-ps frame times, is shown in Fig. 102.11. The framing camera was timed to diagnose the implosion from the end of the laser pulse to  $\sim 1$  ns later. The first frame, at 1.0 ns (around the end of the laser pulse), showed a ring of coronal self-emission that extended beyond the x-ray emission spot from the gold backlighter foil. This self-emission was also observed by an imaging streak camera. Each of the later images shows a ring of x-ray absorption that becomes smaller as the target implodes. The rings are almost round, indicating that the PDD drive is nearly uniform, but with some low-mode structure analyzed in detail below. The position of the ring relative to the backlighting spot varies due to parallax. Simulations show that, for the first three images, the x-ray absorption minimum is virtually independent of x-ray wavelength in the relevant 2- to 3-keV range and is located very close to the inner surface of the imploding shell, whereas the self-emission ring comes from the corona on the outside of the target. (The fourth image is harder to interpret since it depends on the profiles near stagnation.)

Experimental determinations of the average shell radius as a function of time are shown in Fig. 102.12. The imaging streak camera provided data up to the end of the laser pulse. The average radii from framing-camera images were available through most of the implosion (although not up to peak compression). The horizontal error bars on these data points indicate the timing uncertainty and the vertical error bars represent the accuracy with which the shell radius can be determined. The experimental data were simulated in 1-D by *LILAC* (postprocessed using Spect3D<sup>19</sup>) and *SAGE*, both codes using a flux limiter<sup>20</sup>  $f$  of 0.06. The lowest-order shell motion is modeled well by both codes, with a small timing difference evident with respect to the framing-camera data.

The main result of the experiment is provided by the solid points and curves of Fig. 102.13, which gives the x-ray absorption radius  $R_{\text{abs}}$  as a function of  $\theta$  at two successive times during the early stages of the implosion [corresponding to Figs. 102.11(b) and 102.11(c)]. To obtain  $R_{\text{abs}}(\theta)$ , the positions of the absorption maximum at points around the ring were visually determined, a circle was fit through these positions,

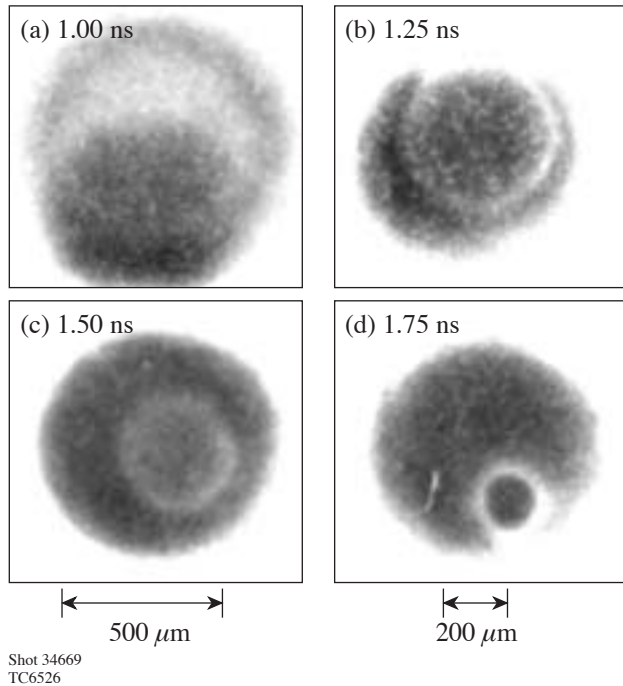


Figure 102.11  
A sequence of four backlit x-ray images at successive times. The first image (at the end of the laser pulse) shows a ring due to self-emission from the corona. The following images show distinct rings of x-ray absorption, corresponding roughly to the inner edge of the imploding CH shell.

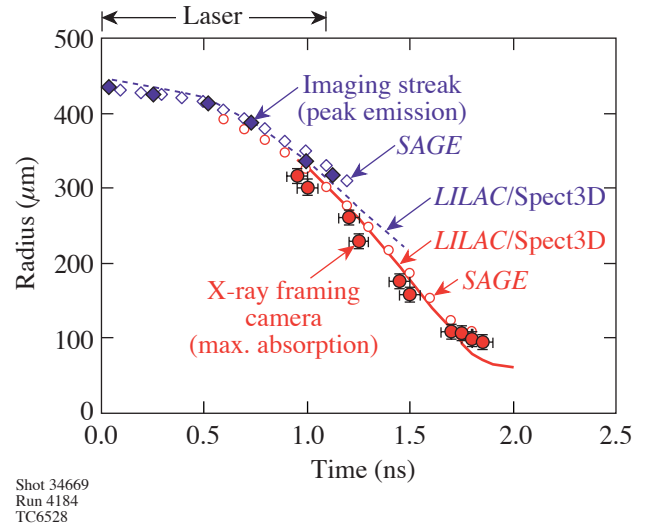


Figure 102.12  
Measured and simulated trajectory of the imploding CH shell. The radius of maximum self-emission from the imaging streak camera (solid diamonds) is compared with *SAGE* predictions (open diamonds) and predictions from *LILAC* postprocessed by Spect3D (dotted line). The radius of maximum x-ray absorption (solid circles) is compared with *SAGE* (open circles) and *LILAC*/Spect3D (solid line). Both simulations assume 1-D symmetric irradiation with the incident laser energy reduced by 10%.

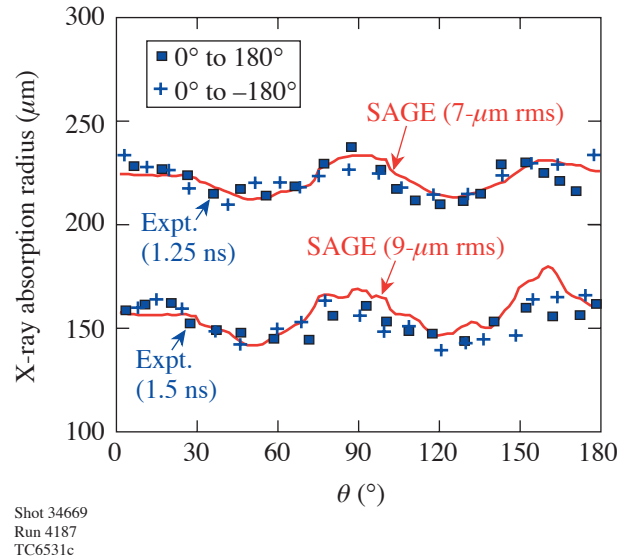


Figure 102.13  
Experimental radii of maximum x-ray absorption  $R_{\text{abs}}$  obtained from the framing-camera images of Fig. 102.11 at 1.25 and 1.5 ns, plotted as a function of angle from the vertical. Squares (pluses) indicate clockwise (counterclockwise) scans from the top of the images. The solid lines are the *SAGE* predictions of  $R_{\text{abs}}$  based on the calculated center-of-mass location  $R_{\text{cm}}$ , with minor adjustments for the viewing angle and the difference between  $R_{\text{cm}}$  and  $R_{\text{abs}}$ .

and the center of this circle was used as a reference point. No corrections were made for nonuniformities in the backlighter. The different symbols in Fig. 102.13 correspond to scanning around the images from top to bottom in the two angular directions. These are equivalent for an azimuthally symmetric implosion; the good agreement is consistent with good azimuthal symmetry and also indicates that errors associated with nonuniformities in the backlighter are minimal. The calculated curves are based on the center-of-mass radius  $R_{\text{cm}}$  of the imploding shell, adjusted by estimates of the distance to the x-ray minimum ( $14 \mu\text{m}$  at  $1.25 \text{ ns}$  and  $24 \mu\text{m}$  at  $1.5 \text{ ns}$ ). This method proved more robust than direct comparison with the calculated x-ray minimum, whose exact location was subject to some numerical noise. The calculated curves are taken at times ( $0.15 \text{ ns}$  later than the nominal experimental times) that allow comparison to be made of the  $\theta$  variations at the same values of the average shell radius. The  $0.15\text{-ns}$  offset represents a combination of the experimental timing uncertainty and the observation that the agreement between simulation and experiment for the lowest-order shell motion (Fig. 102.12), while very close, is not exact. Deviations from symmetry about  $\theta = 90^\circ$  in the simulations, in particular the peak at  $160^\circ$  at the later time, are due to numerical noise that grows at later times. The best indication of the PDD drive nonuniformity is provided at the earlier time when the noise is small.

Figure 102.13 shows that the rms perturbation amplitude increased from  $7 \mu\text{m}$  to  $9 \mu\text{m}$  as the shell radius decreased from  $\sim 225 \mu\text{m}$  to  $\sim 150 \mu\text{m}$  (compared with an initial radius of  $\sim 430 \mu\text{m}$ ). At both times the experimental mode structure and amplitude agree well with the simulations, with the drive weak at the equator and at the poles. This agreement provides confidence that the beam pointings for optimum uniformity can be accurately predicted. This is important for the NIF, where a limited number of shots will be available for tuning the drive uniformity.

The compressed core was imaged using a time-integrating Kirkpatrick–Baez (KB) microscope with  $\sim 3\text{-}\mu\text{m}$  spatial resolution, filtered to look at x rays from 3 to 7 keV.<sup>21</sup> Shot 34644 (60 beams, each with  $2/3$  of the nominal beam energy of 400 J pointed to target chamber center) and shot 34668 (40 PDD beams) are compared in Figs. 102.14(a) and 102.14(b). The core in the PDD case was less spherical, and the neutron yield  $Y_{\text{DD}}$  was reduced by a factor of about 3.

The evolution of the shell nonuniformity observed in Fig. 102.13 was consistent with the center-of-mass velocity nonuniformity at the end of the laser pulse ( $1.1 \text{ ns}$ ), shown in

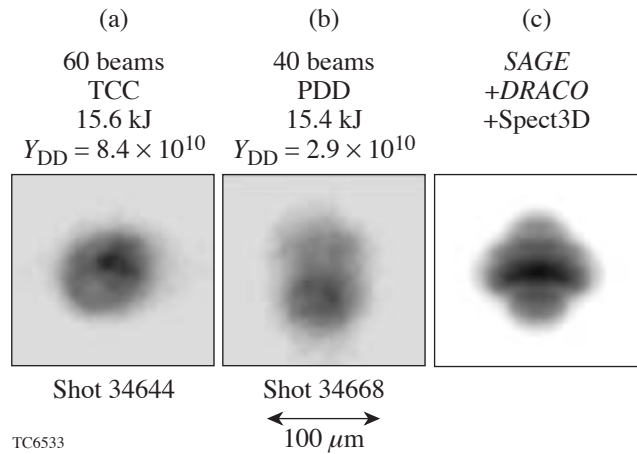


Figure 102.14

Time-integrated KB microscope images for (a) a target irradiated symmetrically with 60 beams, each with  $2/3$  nominal energy, pointed at target chamber center (TCC), (b) a 40-beam PDD target, and (c) a simulation of (b). While all images share the same spatial scale, care should be exercised when comparing (b) and (c) because of the different gray scales used.

Fig. 102.15(a). The minimum at the equator (and, indeed, the falloff from  $\theta = 60^\circ$  to  $\theta = 90^\circ$ ) is found for all feasible combinations of ring pointings. The optimum overall rms nonuniformity of 3.8% is obtained by reducing the drive at the poles. The low drive pressure at the equator causes mass to flow toward the equator. Figure 102.15(b) shows the transverse velocity  $V_\theta$ , positive between  $\theta = 60^\circ$  and  $\theta = 90^\circ$  and negative from  $90^\circ$  to  $120^\circ$ . This small velocity (whose rms is  $\sim 2.5\%$  of  $V_r$ ) can lead to increasing transverse mass flow toward the equator as the implosion proceeds.

To follow the implosion from the end of the laser pulse, low- $\ell$  fits to the *SAGE* center of mass  $V_r$  and  $V_\theta$  were used to perturb a hitherto uniform *DRACO* simulation. Even values of  $\ell$  were used for  $V_r$  and odd for  $V_\theta$  (as  $V_\theta$  results from gradients in the  $\theta$  direction). *DRACO* contours of mass density  $\rho$  and electron temperature  $T_e$  at the time of peak neutron production are given in Figs. 102.15(c) and 102.15(d), respectively. The solid line indicates the CH/D<sub>2</sub> interface. The  $\ell = 4$  perturbation continues throughout the implosion. The calculated neutron yield was  $5.4 \times 10^{10}$ , reduced from  $1.3 \times 10^{11}$  for a comparison unperturbed simulation by a factor of 0.42, close to the experimental reduction factor of 0.35, suggesting that the experimental reduction can be explained mainly by the imposed low- $\ell$  perturbations. (Similar yield reductions have been obtained in full *DRACO* simulations using its approximate ray-trace option.)

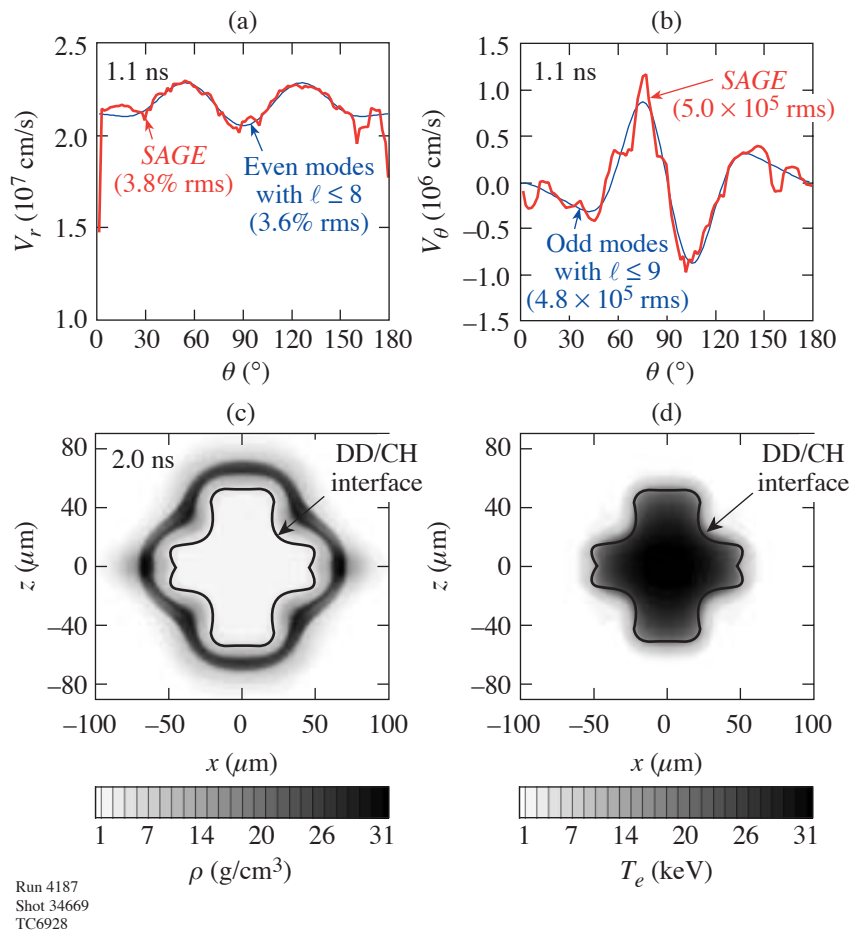


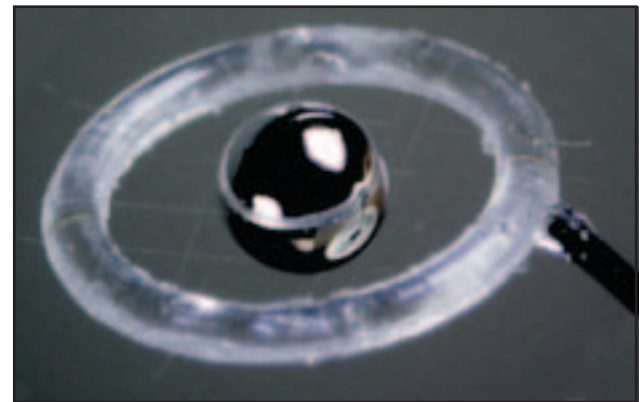
Figure 102.15

*SAGE/DRACO* simulation of a PDD implosion. Low- $\ell$  Legendre fits to (a) the center-of-mass radial velocity  $V_r$  and (b) the transverse velocity  $V_\theta$  calculated by *SAGE* at the end of the laser pulse (1.1 ns) were used to perturb a hitherto symmetric *DRACO* simulation. The density  $\rho$  and electron temperature  $T_e$  contours at the time of peak neutron production are given in (c) and (d), respectively.

The *DRACO* profiles were postprocessed by Spect3D to form the time-integrated x-ray image shown in Fig. 102.14(c). The experimental image shows a lower intensity in the upper half as indicated in the calculated image. This is ascribed to mass that has accumulated near the equator, partially obstructing the view of the core taken from  $15.6^\circ$  below the equator.<sup>22</sup>

### Saturn Experiments on OMEGA

The first Saturn target implosion experiments have been performed on OMEGA. Standard OMEGA capsules (20- $\mu\text{m}$  CH shells filled with 15 atm of  $\text{D}_2$ ) were supported using spider silk on a CH ring of 1100- $\mu\text{m}$  major radius and 150- $\mu\text{m}$  minor radius (see Fig. 102.16). The capsule was centered in the ring to an accuracy usually better than 40  $\mu\text{m}$ . While the calculated optimum pointing called for the ring-1  $\Delta r$  to be changed from 90  $\mu\text{m}$  to 30  $\mu\text{m}$ , to give a stronger drive at the poles, the actual experimental pointing was unchanged to isolate the change of uniformity induced by the ring.<sup>23</sup> The backlighting configuration was modified from that shown in Fig. 102.6 to include a second framing camera viewing from  $26.6^\circ$  above the equator, to avoid obscuration by the ring.



TC6659

Figure 102.16

A Saturn target shot on OMEGA. Using eight strands of spider silk, a standard 865- $\mu\text{m}$ -diam capsule is mounted on a CH ring of major radius 1100  $\mu\text{m}$  and minor radius 150  $\mu\text{m}$ .

The ring plasma forms mainly in the later part of the laser pulse, as in the NIF design described in the preceding article. Predicted density contours at two times are shown in Fig. 102.17. A “bow shock” is observed where the ring plasma and capsule plasma collide. The absorbed power in the capsule was almost the same as in the standard-PDD case (see Fig. 102.9) and that in the ring was fairly constant.

Figure 102.18(a) shows a time-integrated pinhole-camera image of the target, viewed  $10.8^\circ$  above the equator. The ring appears as a shadow obscuring some of the plasma. There is evidence of the bow shock near the inner edge of the ring. The imploded core is heavily overexposed. A better-filtered image of the core, obtained from the KB microscope and dominated by emission from the CH/D<sub>2</sub> interface, shows prolate core emission [Fig. 102.18(b)].

Framing-camera images of the imploding shell obtained from the  $26.6^\circ$  view [Figs. 102.18(c)–102.18(e)] show a clear  $\ell = 2$  mode, evident from the earliest time. The x-ray absorption radii from the first two images, whose times correspond to the standard-PDD data shown in Fig. 102.13, are plotted in Fig. 102.19 along with predictions corrected for the viewing angle (i.e., around a great circle in a plane tipped  $26.6^\circ$  from the vertical). The predictions (solid curves) show an  $\ell = 4$  pattern with slightly reduced amplitude compared with the standard-PDD case (dotted curves). The Saturn data show an  $\ell = 2$  mode with the strongest drive on the equator, larger than predicted.

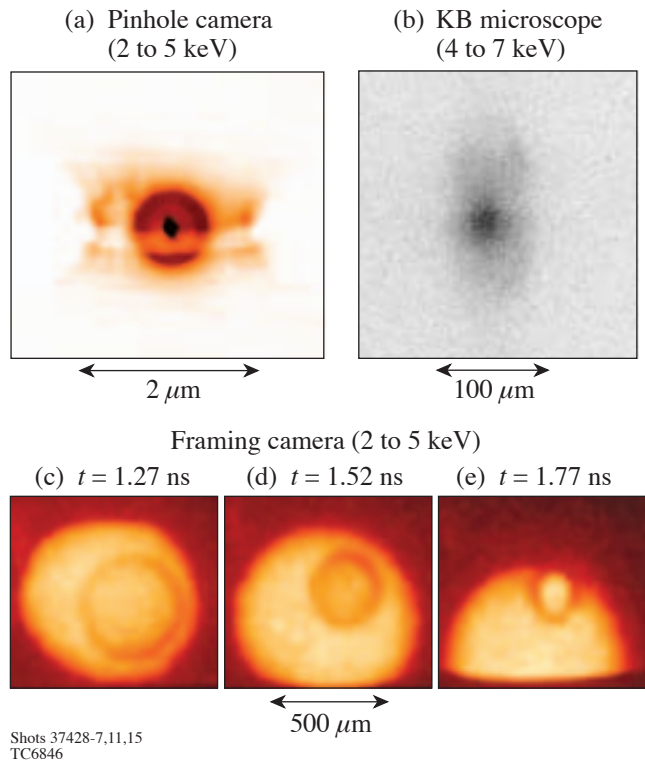


Figure 102.18 X-ray images of Saturn-target implosions. (a) Time-integrated pinhole-camera image, from  $10.8^\circ$  above the equator, including self-emission, the shadow of the ring, the bow shock, and a prolate core (saturated). (b) Time-integrated KB microscope image of the core. (c)–(e) Framing-camera backlit images of the imploding shell viewed  $26.6^\circ$  above the equator.

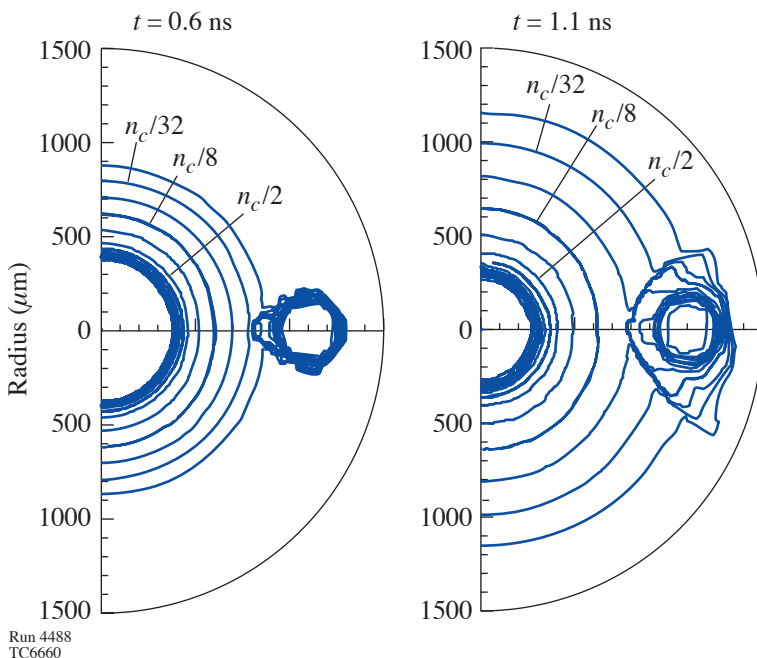


Figure 102.17 Simulated electron-density contours at 0.6 and 1.1 ns for the Saturn target. The ring plasma grows primarily in the second half of the laser pulse, forming a “bow shock” where it collides with the plasma ablating from the capsule.

The primary reason for this disagreement is believed to be radiation from the ring plasma to the capsule, not included in the simulations. In addition, it is possible that the ring plasma is not behaving as modeled. Much of the laser energy absorbed by the ring comes from rays near the edge of the beam profile, which may contain more energy than implied by the super-Gaussian fit. The ring may not be azimuthally symmetric: while it is probably irradiated uniformly by the light from all beams that is refracted from the capsule plasma, it is also irradiated directly in localized regions by the edges of the ring-3 beams. Such asymmetries would lead to a more rapid local growth of the ring plasma.

The Saturn target that came closest to design specifications yielded  $1.8 \times 10^{10}$  DD neutrons, slightly less than two standard-PDD targets shot immediately prior to the Saturn targets that yielded  $2.1$  and  $2.4 \times 10^{10}$  neutrons, respectively. This is consistent with the greater low- $\ell$  drive variations seen in Fig. 102.19, suggesting that removal of the strong  $\ell = 2$  non-uniformity would improve the Saturn yield. This can be accomplished by changing some of the repointings  $\Delta r$  to shift some of the drive back toward the poles or by increasing the major radius (or decreasing the minor radius) of the ring.

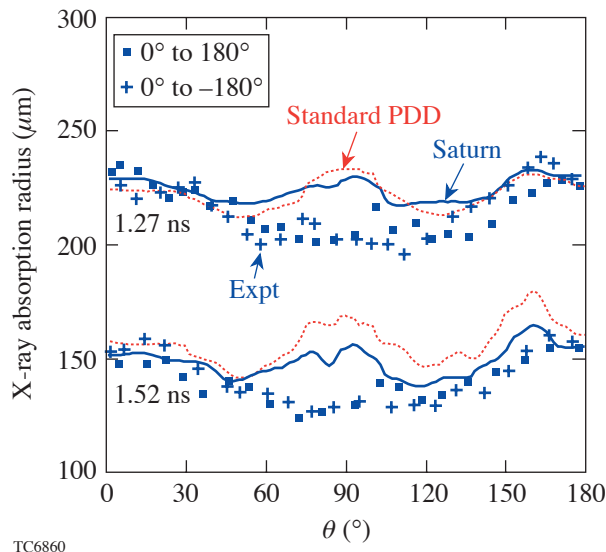


Figure 102.19  
X-ray absorption radius as a function of angle  $\theta$  around the image obtained from the 1.27-ns and 1.52-ns Saturn-target images in Fig. 102.18 together with *SAGE* predictions obtained as in Fig. 102.13 (solid curves). The dotted curves are taken from Fig. 102.13 for a standard-PDD target. The experimental data indicate that the increase in equatorial capsule drive is greater than predicted.

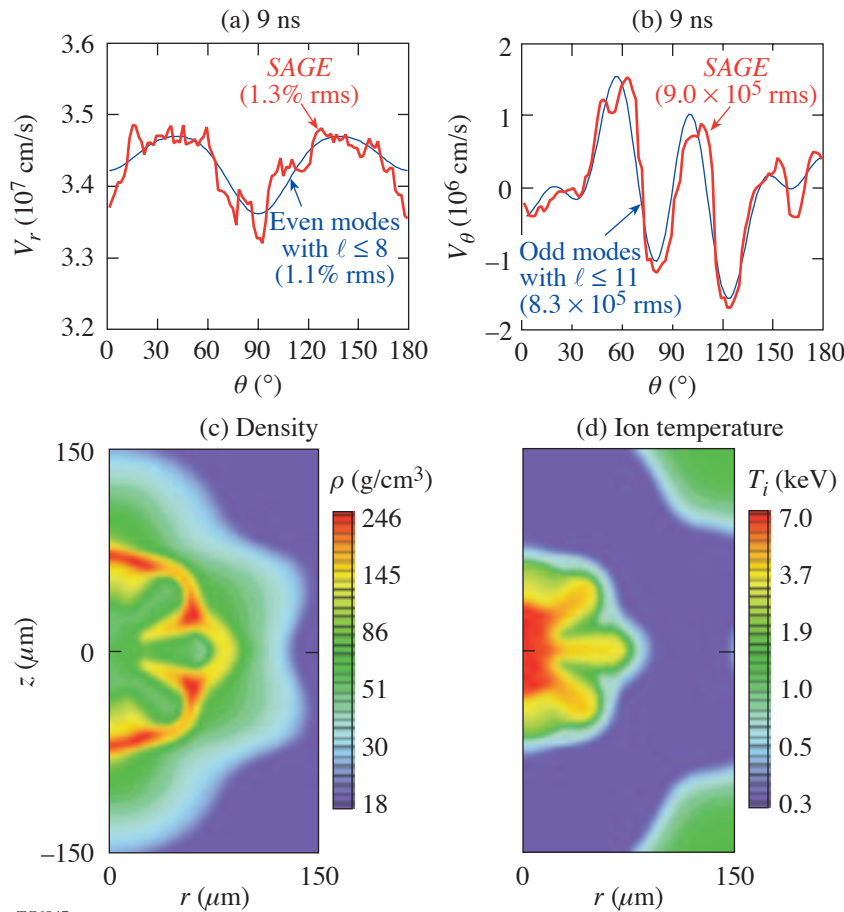
### High-Gain Saturn Design for the NIF

In the preceding article, a Saturn design for the NIF was calculated up to the end of the laser pulse and optimized for minimum rms center-of-mass nonuniformity. In this section the subsequent implosion of this design is modeled using the *SAGE/DRACO* technique described above.

The Saturn ignition design adds a CH ring of 3000- $\mu\text{m}$  major radius to the all-DT capsule described in Ref. 7 and repoints the beams incident at  $30^\circ$ ,  $44.5^\circ$ , and  $50^\circ$  with  $\Delta r = 240 \mu\text{m}$ ,  $280 \mu\text{m}$ , and  $750 \mu\text{m}$ , respectively. The  $44.5^\circ$  and  $50^\circ$  beams use “elliptical” phase plates whose target-plane profiles are reduced in the  $z$  direction by factors of  $\cos(30^\circ)$  and  $\cos(50^\circ)$ , respectively. The center-of-mass velocity perturbations  $V_r$  and  $V_\theta$  near the end of the laser pulse are shown in Figs. 102.20(a) and 102.20(b), together with low-mode Legendre fits. Of the 1.3% calculated rms  $V_r$  perturbation, 1.1% can be accounted for by modes 2 and 4 (the difference largely being due to noise in the simulation). An initially symmetric *DRACO* simulation was perturbed with the Legendre fits and was continued through the thermonuclear burn phase. (More-accurate simulations would also transfer the 9- $\mu\text{m}$ -rms center-of-mass modulations in shell excursion at this time and modulations in mass per solid angle, both considered to be small.) Contours of density and ion temperature from *DRACO* are shown in Figs. 102.20(c) and 102.20(d) at the onset of ignition. The imposed  $\ell$ -mode pattern is maintained through the coasting and deceleration stages. This nonuniformity is sufficiently small to allow ignition to occur, with little effect on the propagating burn wave. The resulting gain is 38, close to the 1-D gain of 45. This result is consistent with the work of McKenty *et al.*,<sup>7</sup> who found that low- $\ell$  perturbations have less effect on the gain of the all-DT design than higher- $\ell$  perturbations ( $\ell \geq 10$ ) of the same amplitude. Consistently, other *SAGE/DRACO* calculations with similar rms nonuniformities imposed in higher- $\ell$  modes ( $\sim 8$ ) perform less well. Inner-ice roughness and imprint, not included in the simulation presented here, are likely to result in similar ( $\sim 30\%$ ) reductions in yield as for symmetrically driven capsules.<sup>7</sup>

### Conclusions

Experiments on OMEGA have confirmed that reasonably symmetric implosions can be carried out using 40 of the 60 beams in a polar configuration. Further, the drive perturbations can be diagnosed with amplitudes and mode structure that are in good agreement with simulations.



TC6847

Figure 102.20

*SAGE/DRACO* simulation of the NIF Saturn target. Low- $\ell$  fits to (a) the *SAGE*-calculated center-of-mass radial velocity  $V_r$  and (b) the transverse velocity  $V_\theta$  were used to perturb a symmetric *DRACO* simulation. The density  $\rho$  and ion temperature  $T_i$  contours at the time of ignition are given in (c) and (d), respectively. The gain of 38 is close to 1-D.

The Saturn implosions reported here demonstrated that a low- $Z$  ring can be used to increase the drive on the equator. Indeed, the maximum drive was observed at the equator, which, according to calculations, cannot happen for standard-PDD targets on the OMEGA laser system. The prospects for improving the uniformity of Saturn targets are excellent, with the possibilities including changes to the beam pointings and ring dimensions. Subsequent OMEGA experiments and modeling, to be reported in a future issue of the LLE Review, have shown that the implosion symmetry and yield can be improved by readjusting the beam pointings and that radiation is indeed the primary cause of the discrepancy between experiment and simulations. Further experiments will provide a better understanding of the formation and evolution of the ring plasma and its azimuthal symmetry, and the physics of the bow shock and its contribution to x-ray emission from the ring remains to be explored. These experiments will enable more-accurate calculations to be made of Saturn targets for the NIF.

Hydrodynamic modeling of the standard-PDD experiments using a combination of *SAGE* and *DRACO* led to a yield reduction close to that observed experimentally. Similar modeling was applied to the Saturn design for the NIF and led to a predicted gain close to 1-D. This result is very encouraging since it improves the prospects of obtaining direct-drive ignition and high gain on the NIF many years before conversion of the NIF to the direct-drive configuration. This work will be published in Ref. 24.

#### ACKNOWLEDGMENT

The authors are grateful to Dr. David Meyerhofer for a careful review of the manuscript and many helpful suggestions. This work was supported by the U.S. Department of Energy Office of Inertial Confinement Fusion under Cooperative Agreement No. DE-FC52-92SF19460, the University of Rochester, and the New York State Energy Research and Development Authority. The support of DOE does not constitute an endorsement by DOE of the views expressed in this article.

## REFERENCES

1. E. M. Campbell and W. J. Hogan, *Plasma Phys. Control. Fusion* **41**, B39 (1999).
2. S. Skupsky, J. A. Marozas, R. S. Craxton, R. Betti, T. J. B. Collins, J. A. Delettrez, V. N. Goncharov, P. W. McKenty, P. B. Radha, T. R. Boehly, J. P. Knauer, F. J. Marshall, D. R. Harding, J. D. Kilkenny, D. D. Meyerhofer, T. C. Sangster, and R. L. McCrory, *Phys. Plasmas* **11**, 2763 (2004).
3. J. D. Kilkenny, Laboratory for Laser Energetics, private communication (2002).
4. R. S. Craxton, presented at the 33rd Anomalous Absorption Conference, Lake Placid, NY, 22–27 June 2003 (Paper WO3).
5. R. S. Craxton, *Bull. Am. Phys. Soc.* **48**, 56 (2003).
6. C. P. Verdon, *Bull. Am. Phys. Soc.* **38**, 2010 (1993).
7. P. W. McKenty, V. N. Goncharov, R. P. J. Town, S. Skupsky, R. Betti, and R. L. McCrory, *Phys. Plasmas* **8**, 2315 (2001).
8. R. S. Craxton and R. L. McCrory, *J. Appl. Phys.* **56**, 108 (1984).
9. P. B. Radha, T. J. B. Collins, J. A. Delettrez, D. Keller, P. W. McKenty, and R. P. J. Town, presented at the 30th Annual Anomalous Absorption Conference, Ocean City, MD, 21–26 May 2000 (Paper 2P11).
10. P. B. Radha, V. N. Goncharov, T. J. B. Collins, J. A. Delettrez, Y. Elbaz, V. Yu. Glebov, R. L. Keck, D. E. Keller, J. P. Knauer, J. A. Marozas, F. J. Marshall, P. W. McKenty, D. D. Meyerhofer, S. P. Regan, T. C. Sangster, D. Shvarts, S. Skupsky, Y. Srebro, R. P. J. Town, and C. Stoeckl, *Phys. Plasmas* **12**, 032702 (2005).
11. S. Skupsky, R. Betti, T. J. B. Collins, V. N. Goncharov, D. R. Harding, R. L. McCrory, P. W. McKenty, D. D. Meyerhofer, and R. P. J. Town, in *Inertial Fusion Sciences and Applications 2001*, edited by K. Tanaka, D. D. Meyerhofer, and J. Meyer-ter-Vehn (Elsevier, Paris, 2002), pp. 240–245.
12. D. Eimerl, ed., Lawrence Livermore National Laboratory, Livermore, CA, UCRL-ID-120758 (1995).
13. S. G. Gledinning, Lawrence Livermore National Laboratory, private communication (2003).
14. G. A. Kyrala *et al.*, *Laser Part. Beams* **23**, 207 (2005).
15. F. J. Marshall, J. A. Delettrez, R. Epstein, R. Forties, R. L. Keck, J. H. Kelly, P. W. McKenty, S. P. Regan, and L. J. Waxer, *Phys. Plasmas* **11**, 251 (2004).
16. S. Skupsky and R. S. Craxton, *Phys. Plasmas* **6**, 2157 (1999).
17. T. R. Boehly, V. A. Smalyuk, D. D. Meyerhofer, J. P. Knauer, D. K. Bradley, R. S. Craxton, M. J. Guardalben, S. Skupsky, and T. J. Kessler, *J. Appl. Phys.* **85**, 3444 (1999).
18. F. J. Marshall, J. A. Delettrez, R. Epstein, R. Forties, V. Yu. Glebov, J. H. Kelly, T. J. Kessler, J. P. Knauer, P. W. McKenty, S. P. Regan, V. A. Smalyuk, C. Stoeckl, J. A. Frenje, C. K. Li, R. D. Petrasso, and F. H. Séguin, *Bull. Am. Phys. Soc.* **48**, 56 (2003).
19. Prism Computational Sciences, Inc., Madison, WI, Report No. PCS-R-041, Ver. 3.0 (2002). See also J. J. MacFarlane *et al.*, in *Inertial Fusion Sciences and Applications 2003*, edited by B. A. Hammel, D. D. Meyerhofer, J. Meyer-ter-Vehn, and H. Azechi (American Nuclear Society, La Grange Park, IL, 2004), pp. 457–460.
20. R. C. Malone, R. L. McCrory, and R. L. Morse, *Phys. Rev. Lett.* **34**, 721 (1975).
21. M. C. Richardson, P. W. McKenty, F. J. Marshall, C. P. Verdon, J. M. Soures, R. L. McCrory, O. Barnouin, R. S. Craxton, J. Delettrez, R. L. Hutchison, P. A. Jaanimagi, R. Keck, T. Kessler, H. Kim, S. A. Letzring, D. M. Roback, W. Seka, S. Skupsky, B. Yaakobi, S. M. Lane, and S. Prussin, in *Laser Interaction and Related Plasma Phenomena*, edited by H. Hora and G. H. Miley (Plenum Publishing, New York, 1986), Vol. 7, pp. 421–448.
21. F. J. Marshall and Q. Su, *Rev. Sci. Instrum.* **66**, 725 (1995).
22. R. Epstein, R. S. Craxton, J. A. Delettrez, F. J. Marshall, J. A. Marozas, P. W. McKenty, P. B. Radha, and V. A. Smalyuk, *Bull. Am. Phys. Soc.* **49**, 180 (2004).
23. The second series of standard-PDD experiments and the Saturn targets used  $\Delta r = 90 \mu\text{m}$ ,  $180 \mu\text{m}$ , and  $180 \mu\text{m}$  for rings 1–3, respectively, not significantly different from the values for the first series indicated in Fig. 102.7.
24. R. S. Craxton, F. J. Marshall, M. Bonino, R. Epstein, P. W. McKenty, S. Skupsky, J. Delettrez, I. V. Igumenshchev, D. W. Jacobs-Perkins, J. P. Knauer, J. A. Marozas, P. B. Radha, and W. Seka, “Polar Direct Drive—Proof-of-Principle Experiments on OMEGA and Prospects for Ignition on the NIF,” to be published in *Physics of Plasmas*.

---

# Direct-Drive, Cryogenic Target Implosions on OMEGA

## Introduction

Thermonuclear ignition via direct-drive, laser-driven, inertial confinement fusion<sup>1</sup> (ICF) will be accomplished by the near-uniform illumination of spherical cryogenic deuterium–tritium (DT) fuel-bearing capsules with high-power laser beams. Achieving thermonuclear ignition and gain will require symmetric compression of the DT-fuel hot spot to high areal densities ( $\sim 0.3 \text{ g/cm}^2$ ) with a temperature of  $\sim 10 \text{ keV}$ . The baseline target consists of either a pure cryogenic DT layer formed on the inside of a thin plastic shell<sup>2</sup> or a DT-filled foam shell.<sup>3</sup> Target imperfections and laser illumination non-uniformities lead to Rayleigh–Taylor unstable growth of fuel-layer perturbations during the implosion and must be minimized. The minimum energy required for ignition scales as  $\sim \alpha^{1.8}$  (Refs. 4–6), where  $\alpha$  is the fuel adiabat, the ratio of the local pressure to the Fermi-degenerate pressure. It has been shown that the ablation velocity, the main contributor to the stabilization of Rayleigh–Taylor unstable growth, scales as  $\sim \alpha^{0.6}$  (Ref. 4). Traditionally, direct-drive ICF has had to balance target performance and stability by a careful choice of the target adiabat. This task has been made easier with the application of adiabat shaping.<sup>7</sup> The ablation region is placed on a high adiabat for stability while maintaining the main fuel layer on a low adiabat, preserving compressibility for good target performance.

The experiments described in this work were performed on LLE’s 60-beam, 30-kJ UV OMEGA laser system.<sup>8</sup> The three major requirements to achieve ignition-scaled conditions in the fuel have been met: (1) near-uniform cryogenic layers, (2) near-uniform laser illumination, and (3) a high-contrast pulse shape maintaining the fuel layer on a low adiabat ( $\alpha \sim 4$ ). The resulting high fuel areal densities ( $\rho R \sim 100 \text{ mg/cm}^2$ ), ion temperature ( $kT_i \sim 2$  to  $3 \text{ keV}$ ), and fusion yield [ $\sim 20\%$  of predicted by one-dimensional (1-D) simulations and in agreement with two-dimensional (2-D) simulations] give increasing confidence to the direct-drive approach to ICF ignition.

This work describes recent progress in direct-drive, cryogenic target implosions on OMEGA. The following sections

(1) describe the experimental conditions and observations, (2) compare the observations with 2-D numerical simulations, and (3) present our conclusions.

## Experiments

This section describes the experimental conditions, including target and laser performance, and the primary experimental observations.

### 1. Targets

The targets used in these experiments were  $\text{D}_2$ -filled, deuterated, strong GDP (a high-strength, glow-discharge polymer) shells with outer diameters of  $\sim 865 \mu\text{m}$ , shell thicknesses of  $\sim 3.7$  to  $4.0 \mu\text{m}$ , and a density of  $1.09 \text{ g/cm}^3$ . The shells were permeation filled with  $\sim 1000 \text{ atm}$  of  $\text{D}_2$  gas in the Fill/Transfer Station (FTS)<sup>9</sup> and then slowly cooled to below the triple point ( $18.7 \text{ K}$ ). The targets were then transported to a characterization station for layer formation and then to the OMEGA target chamber for implosion.

The formation of a near-uniform layer is accomplished in a layering sphere<sup>9</sup> using an IR laser tuned to the  $\text{D}_2$ -ice absorption band at a wavelength of  $3.16 \mu\text{m}$ . The residual inner-ice-surface nonuniformities, after careful layer preparation, are determined using the shadowgraphic technique described in Stoeckl *et al.*<sup>10</sup> and shown in Fig. 102.21. This technique has been extended to map the inner surface of the ice layer in 3-D by combining layer-thickness measurements from multiple views (48 typically, consisting of 24 orthogonal pairs). In addition to the inner-ice-surface roughness, the outer-surface roughness of the CH shell is also determined. The mean inner-ice roughness for the target experiments included in this work was  $5 \mu\text{m}$  (rms) with the best being  $1.3 \mu\text{m}$ . Three-dimensional (3-D) reconstructions of the ice layer from these multiple views were used as input to the 2-D hydrodynamic simulations described in **Comparison of Experimental Results and 2-D Simulations** (p. 82).

The standard deviation of the mean layer thickness from individual views is typically  $\leq 2 \mu\text{m}$ . However, there are other

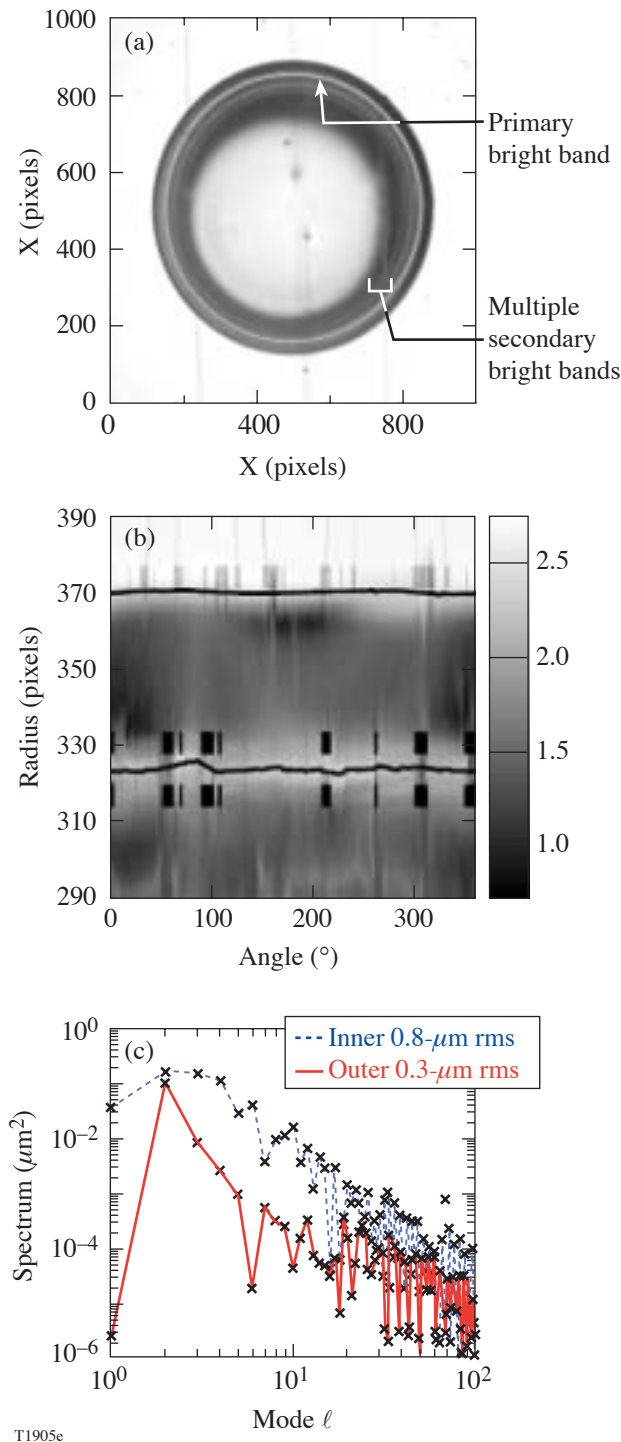


Figure 102.21  
Cryogenic target layer characterization. (a) A single shadowgraph, (b) layer-thickness measurements, and (c) resultant mode spectrum.

ways to characterize the errors of the ice-layer nonuniformity. For example, the ice layer for shot 35713 had a 4.2- $\mu\text{m}$  mean rms, predominately in the four lowest  $\ell$  modes. Based on the 3-D reconstruction of the ice layer, a peak-to-valley of  $\pm 10 \mu\text{m}$  existed over  $\sim 1\%$  of the surface. These larger variations will likely affect target performance to a greater degree than represented by the standard deviation of the mean of the individual measurements. An effort is underway to more accurately determine the mean ice-roughness error and its impact on target performance and simulations.

## 2. Laser System Conditions

Cryogenic capsules were imploded with pulse shapes ranging from a high-adiabat ( $\alpha \sim 25$ ), 23-kJ, 1-ns square pulse to a low-adiabat ( $\alpha \sim 4$ ), 17-kJ, 2.5-ns shaped pulse. The fuel adiabat at the end of the acceleration phase is determined by using the pulse shape, as measured by a high-bandwidth streak camera,<sup>11</sup> as input to the 1-D hydrocode *LILAC*.<sup>12</sup> Full beam smoothing, including distributed phase plates (DPP's),<sup>13</sup> polarization smoothing with distributed polarization rotators (DPR's),<sup>14</sup> and 2-D, single-color-cycle, 1-THz smoothing by spectral dispersion (SSD),<sup>15</sup> was used for these experiments. Recent experiments ( $\alpha \sim 4$ ) were performed with a new set of DPP's<sup>16</sup> with a 95% enclosed energy diameter of 865  $\mu\text{m}$  and a "super-Gaussian" order  $n = 3.7$ . The new DPP's reduce the need to use enhanced fluence balance.<sup>17</sup> Beam mispointing is reduced from an average of  $\sim 20\text{-}\mu\text{m}$  rms to an average of  $\sim 10\text{-}\mu\text{m}$  rms by active repointing requiring two pointing shots.<sup>16,17</sup> These combined effects have reduced the long-wavelength nonuniformities of the laser system from  $\sim 3\%$  to  $\sim 1.3\%$ . This condition was applied to all  $\alpha \sim 4$  implosions in this work. The largest contribution to the long-wavelength nonuniformities is the location of the target with respect to the center of the target chamber (TCC offset) at shot time.

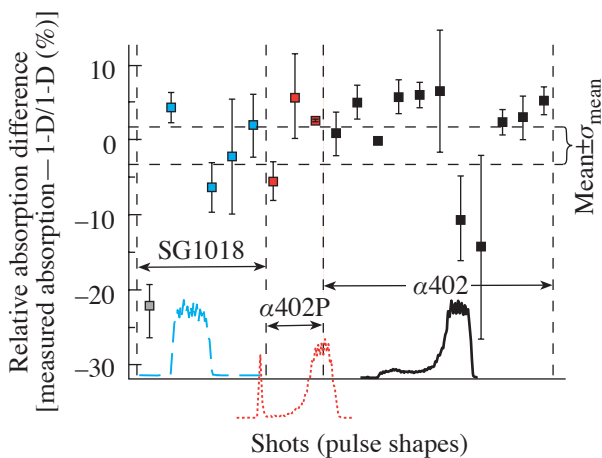
## 3. Absorption Measurements

The scattered light was measured by calorimeters in two full-aperture-backscatter stations (FABS's). These calorimeters sample the light backscattered through two OMEGA focusing lenses. Extensive 2-D ray-tracing simulations using 1-D hydrodynamic code predictions for the time-varying plasma density and temperature profiles have shown that the scattered light variations around the target are within  $\sim 3\%$  of perfect uniformity. Spot measurements with calorimeters between the OMEGA focusing lens positions have confirmed these predictions. Nevertheless, random shot-to-shot fluctuations in the various calorimeter measurements can be as high as 7% rms per shot. These fluctuations are thought to be due to target centering and subtle beam-pointing issues. In contrast,

the shot-to-shot reproducibility of the average calorimeter reading is typically within 2% to 3%, inspiring confidence in the validity of the average scattered-light measurements. Since the long-term calibration stability of the scattered-light calorimeters between the focusing lenses is difficult to ascertain, we use only scattered-light energies measured at the two FABS's and extrapolate them to  $4\pi$ . These data yield a good measure for the total absorbed energy.

Reliable measurements of absorbed energy in spherical target implosions are essential for quantitative comparison with hydrodynamic code simulations. The absorption predicted by these codes is based primarily on 2-D ray tracing and inverse bremsstrahlung absorption and depends sensitively on the electron thermal transport. The latter is typically modeled using flux-limited diffusion.<sup>18,19</sup> A flux limiter  $f = 0.06$  was used for all simulations in this work.

Figure 102.22 shows the fractional difference of the measured absorption from *LILAC* predictions for a series of cryogenic implosions with the pulse shapes shown as insets. Error bars represent the difference of the two FABS measurements. The agreement between the measurements and the 1-D *LILAC* predictions is excellent (horizontal dashed lines in Fig. 102.22) when averaged over all shots. We have also made time-resolved scattered-light measurements (and, consequently, time-resolved absorption measurements) that are in equally good agreement over the entire pulse shape for all of the pulse shapes.<sup>20</sup>



E13392

Figure 102.22  
Absorption fraction measurements shown as percent variation from 1-D predicted value.

Determination of the fuel adiabat depends on the detailed time history of the absorbed energy, requiring precision measurement of the laser pulse shape. Using P510 streak cameras<sup>11</sup> with a demonstrated bandwidth of  $\sim 20$  GHz in the UV in selected channels, the simulations are provided with pulse shapes that include an initial low-intensity rise of  $\sim 40$  ps/decade for all pulse shapes. These rise times were measured using 1-ns square pulses best suited for this purpose. The same pulse switching provides the initial rise for all other pulse shapes. Details of the initial rise are of importance to simulations. With these inputs, optimum zoning strategies were developed for the *LILAC* simulations that led to improved absorption calculations<sup>7</sup> in the leading edge of the strongly shaped  $\alpha 401$ ,  $\alpha 402$ , and  $\alpha 402P$  (with picket) pulses. All of these improvements have led to better agreement between the measured and simulated time-integrated and time-resolved absorption fractions, as well as improved estimates for the fuel adiabat during the implosion phase. Thus, previously predicted  $\alpha \sim 4$  pulses were found to produce slightly higher calculated adiabats ( $\alpha \sim 6$ ). New pulse shapes, incorporating better design of the leading edge, have been incorporated into current OMEGA experiments.

#### 4. Fusion Yield

The fusion reaction rate for these experiments is determined by the neutron temporal diagnostic (NTD),<sup>21</sup> with the absolute rate obtained by normalizing with the neutron yield. Figure 102.23 shows the NTD measured and simulated neutron rate for a low-adiabat ( $\alpha \sim 4$ ) implosion. The duration and peak time are seen to fall within the absolute measurement uncertainty ( $\pm 0.1$  ns). The integrated yield for this implosion was  $1.6 \times 10^{10}$ , while the *LILAC* prediction was  $9.1 \times 10^{10}$  [yield over calculated (YOC) = 18%]. The coincidence of the measured and predicted peak burn times confirms the observations from the absorption measurements that the simulations are correctly predicting the absorption and hydrodynamic coupling in cryogenic targets.

#### 5. Fuel Areal Density

The total fuel areal density in cryogenic  $D_2$  implosions is inferred from the energy loss of secondary protons from the  $D^3He$  reaction. The secondary proton spectrum at birth is well defined by the kinematics of the  $D^3He$  reaction so that the average energy of the protons emerging from the dense fuel depends on the total burn-averaged areal density  $\langle \rho R \rangle_n$ . Wedge-range-filter spectrometers (WRF's)<sup>22</sup> measure the secondary proton spectrum along multiple lines of sight (generally four to six). These individual measures of the  $\rho R_n$  are averaged to obtain the reported  $\langle \rho R \rangle_n$ . The error associated with each

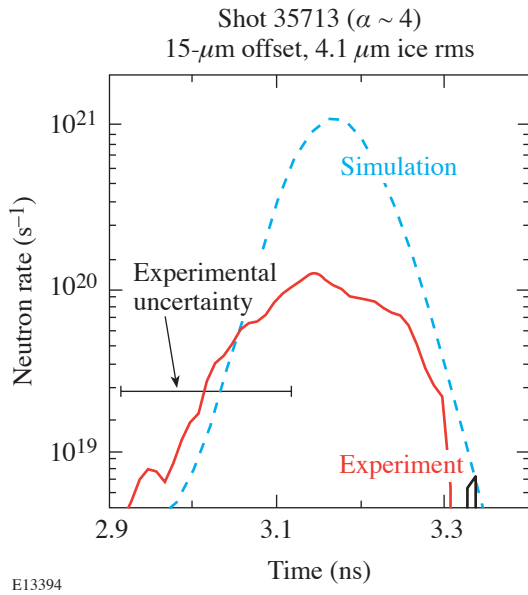


Figure 102.23  
NTD measurement of the fusion reaction rate for an  $\alpha \sim 4$  cryogenic target implosion (shot 35713). The 1-D simulated fusion rate is also plotted.

individual measure is approximately 5% (typically a 150-keV uncertainty out of a 3-MeV energy loss). However, the variation among the individual measurements is often quite large due to low-mode variations in the initial ice thickness and drive symmetry. The dominant factor in the drive asymmetry is the location of the capsule with respect to chamber center at shot time (the TCC offset discussed above).

Figure 102.24 shows the correlation between the experimentally inferred  $\langle \rho R \rangle_n$  and the value of  $\langle \rho R \rangle_n$  predicted by the 1-D hydrocode *LILAC* for all cryogenic implosions in which the offset from TCC was  $< 60 \mu\text{m}$  and the inner-ice-layer rms roughness was  $< 6 \mu\text{m}$ . The solid circles near 50  $\text{mg}/\text{cm}^2$  represent high-adiabat implosions ( $\alpha \sim 25$ ) driven by a 1-ns square pulse (see Fig. 102.22) and show near 1-D performance in the assembly of the fuel (typically, the primary neutron yields are 50% to 70% of 1-D). The open circles represent low-adiabat implosions using a high-contrast pulse shape similar to the one shown in Fig. 102.22. Although designed to put the fuel shell on an adiabat of 4, the actual shape of the drive pulse delivered to the capsules varied from shot to shot such that the calculated adiabat ranged from  $\sim 4$  to just over 6. In a few cases, the calculated adiabat ranged between 6 and 12. Therefore, the points are labeled as “mid- $\alpha$ ” and “ $\alpha \sim 4$  to 6” [a subset of these implosions is discussed later in **Comparison**

**of Experimental Results and 2-D Simulations** (p. 82)]. The key feature to note is that as the adiabat of the fuel decreases, the deviation of the experimentally inferred  $\langle \rho R \rangle_n$  from 1-D performance increases. This discrepancy is expected and discussed further in **Comparison of Experimental Results and 2-D Simulations** (p. 82).

The drive pulses for the most recent implosions (shots 37967 and 37968) were carefully tuned to obtain the desired adiabat in the fuel. These two points are labeled as “ $\alpha = 3.5$  to 3.8.” The  $\langle \rho R \rangle_n$  for shot 37968 was  $98 \pm 22 \text{ mg}/\text{cm}^2$ . The error here represents the standard deviation of the individual measurements (seven for this shot) and suggests a significant offset from TCC at shot time (the standard deviation is typically much larger than the errors associated with the individual measurements). For this shot, the measured offset was  $\sim 40 \mu\text{m}$ . The error bar is considerably smaller for shot 35713 and consistent with the much smaller offset at shot time, 15  $\mu\text{m}$ . This confirms that the variation among the individual measurements is dominated by the offset from TCC at shot time.

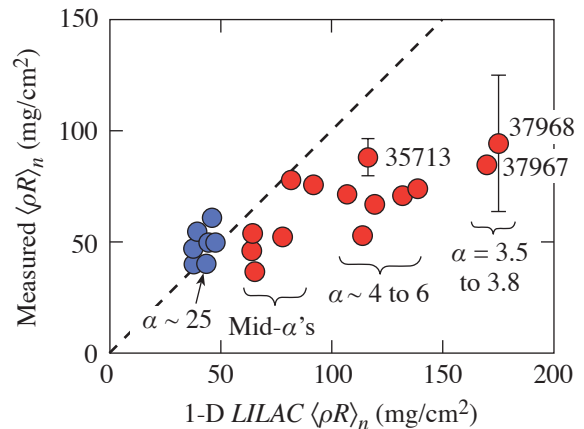


Figure 102.24  
Measured  $\langle \rho R \rangle_n$  as function of 1-D predicted value. The range of fuel adiabats is also indicated.

## 6. Stagnation

Peak density occurs in these implosions after the time of peak neutron production. Recent works<sup>23,24</sup> have shown that the time history of the fuel  $\rho R$  can be inferred from the combined measurements of the proton spectrum and the reaction rate history. The fuel  $\rho R$  increases until final stagnation, when the bulk of the fuel is heated to a lower temperature than the hot

core. At this point, the x-ray flux increases dramatically, allowing a diagnosis of stagnation by x-ray imaging. Figure 102.25 shows a pair of quasi-monochromatic x-ray images from a grating-dispersed Kirkpatrick–Baez (KB) microscope<sup>25</sup> [Fig. 102.25(a)] and an x-ray framing camera (XRFC) filtered to be sensitive to x rays in the range of 4 to 5 keV [Fig. 102.25(b)]. The KB microscope is time integrating, has a resolution of  $\sim 3 \mu\text{m}$ , and is dispersed by a transmission grating that convolves space and spectrum in the spectral direction.<sup>25</sup> The stagnation-region size as a function of mean wavelength can be measured in the perpendicular direction. The radial profile of this emission at 4 keV is shown in Fig. 102.25(c) along with the azimuthal average lineout from the XRFC image (frame closest to peak x-ray emission within  $\pm 50$  ps, and within a 50-ps time window). These are compared with the simulated time-integrated emission profile from a *LILAC* postprocessor. The good agreement between both measurements and the simulated profile indicates that the fuel-stagnation core size is close to the 1-D prediction. The absolute flux and slope of the continuum determined from the grating-dispersed KB image [Fig. 102.25(d)] also show close agreement with the 1-D postprocessor prediction. The inferred stagnation electron temperature is  $kT_e = 1.3$  keV (averaged over the time of the x-ray emission).

### Comparison of Experimental Results and 2-D Simulations

The goal of the OMEGA cryogenic implosion program is to validate the predicted performance of low-adiabat, ignition-scaled implosions on OMEGA. The first set of experiments in this phase employs an  $\alpha \sim 4$  pulse shape (shown as an inset in Fig. 102.22). Several  $\alpha \leq 4$  implosions (see Fig. 102.24) were undertaken using the OMEGA laser; for brevity, only a single implosion (35713) will be described in detail.

The target was  $870 \mu\text{m}$  in diameter with a  $3.8\text{-}\mu\text{m}$ -thick GDP shell, a  $95\text{-}\mu\text{m}$ -thick  $\text{D}_2$ -ice layer, and an interior-ice-surface roughness of  $4.2 \mu\text{m}$ . The power spectrum for this surface, as shown in Fig. 102.26(a), is heavily weighted toward low-order modes. The capsule was  $\sim 15 \mu\text{m}$  from target chamber center at the beginning of the implosion. The experimental neutron yield for this implosion was  $1.6 \times 10^{10}$ , which represents the highest-ever experimental yield obtained from a cryogenic  $\alpha \sim 4$  implosion (YOC  $\sim 18\%$ ). The ice-roughness spectrum from Fig. 102.26(a) and an initial 3.1%,  $\ell = 1$  illumination nonuniformity, due to the target offset, were used in a *DRACO* 2-D hydrodynamic simulation.<sup>26</sup> Laser imprint was modeled in these calculations with modes  $\ell = 2$  to 200. The simulated core can be seen in Fig. 102.26(b) to have

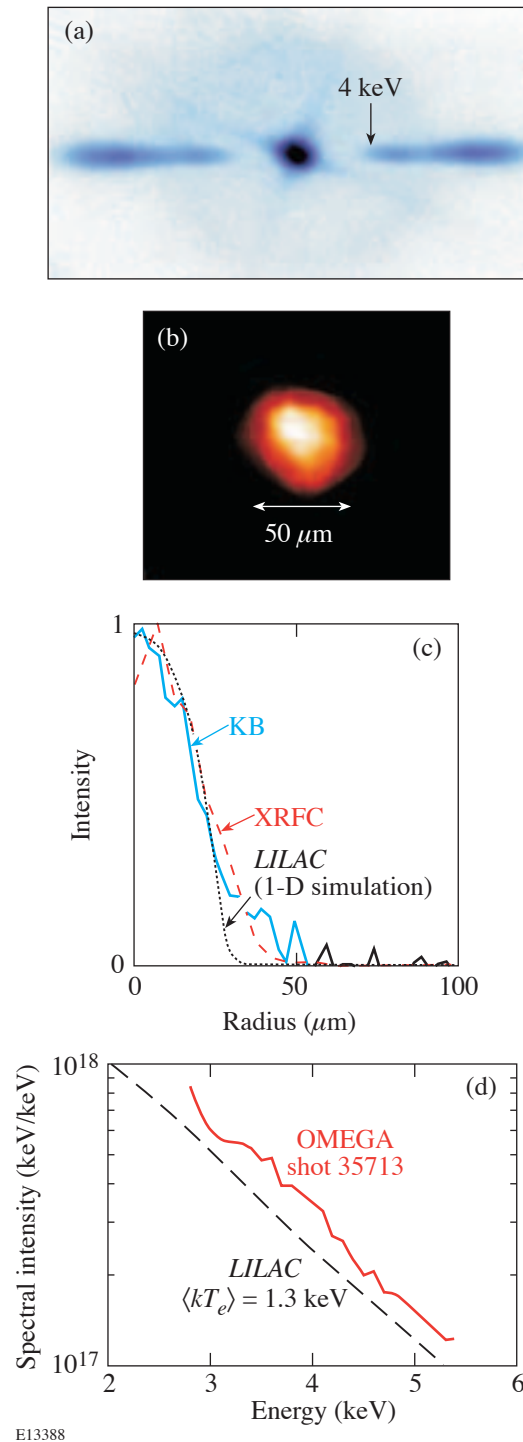


Figure 102.25

X-ray images of the fuel core at stagnation (shot 35713) from (a) a grating-dispersed KB and (b) an XRFC. (c) Radial profiles of images compared to 1-D prediction, and (d) absolute continuum x-ray spectrum (3 to 5 keV) obtained from a KB image of core emission compared to the 1-D prediction.

assembled slightly ( $\sim 10 \mu\text{m}$ ) off-axis due to the presence of the  $\ell = 1$  component of the initial inner-ice roughness and target offset, resulting in a 2-D simulated neutron yield of  $1.8 \times 10^{10}$ . Additional measurements and simulations are given in Fig. 102.26(c). The core performance, however, is not dominated by the  $\ell = 1$  perturbation, as has been the case with previous experiments, but is dominated by the presence of growing perturbations due to modes 6 to 10 from the illumination. The performance of this implosion was also seen to be somewhat sensitive to the presence of laser imprint, due to the stability characteristics of the  $\alpha \sim 4$  pulse. While the core does not appear to be influenced by the high-frequency modes, the presence of these modes is observed in the overdense regions of the shell near the corona. Simulations without laser imprint resulted in  $\sim 20\%$ - to  $25\%$ -higher neutron yields. The secondary-yield comparison also shows that the *DRACO* simulation is close to the experimental result. The simulated neutron-

averaged areal density [ $\langle \rho R \rangle_n$  (*DRACO*) =  $101 \text{ mg/cm}^2$ ] is close to the experimentally obtained value

$$[\langle \rho R \rangle_n (\text{expt.}) = 88 \pm 10 \text{ mg/cm}^2].$$

The angular variation of the simulation and the range of measured values are shown in Fig. 102.26(d).

It should be noted that the calculated and measured ion temperatures do not agree. The calculation of the ion temperature in the hydrocodes does not include the effect of the collective motion of the fuel. Furthermore, the calculation does not produce a thermally broadened neutron energy spectrum, which is what is used to experimentally infer the plasma ion temperature during the burn. This discrepancy will be addressed in the future.

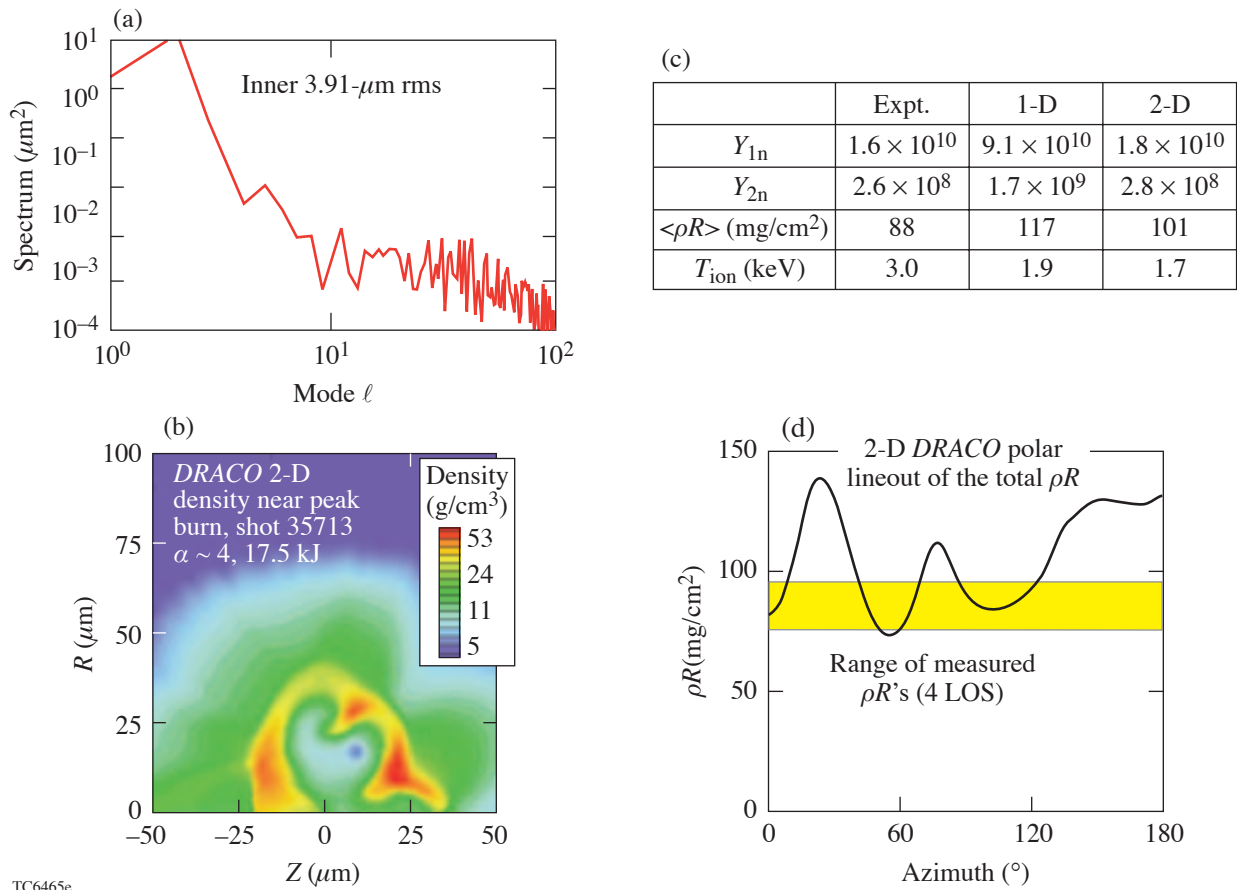


Figure 102.26

2-D *DRACO* simulation of shot 35713. (a) Spectrum of  $\text{D}_2$ -ice-surface roughness used as input, (b) isodensity contours at time of peak neutron-production rate, (c) table of measured and predicted primary and secondary yields,  $\langle \rho R \rangle_n$ , and ion temperature, and (d) angular variation of areal density from *DRACO* simulation with the range of measurements indicated by the shaded region.

Low-adiabat target performance has been previously presented<sup>2</sup> as a compilation of all perturbation sources using a sum-in-quadrature representation of each source’s contribution to the roughness of the inner ice layer at the end of the acceleration phase of the implosion. The scaling parameter  $\bar{\sigma}$  is defined as

$$\bar{\sigma}^2 = 0.06\sigma_{\ell(\ell < 10)}^2 + \sigma_{\ell(\ell > 10)}^2,$$

where  $\sigma_{\ell}$  is the rms roughness computed over the indicated mode range. At this time in the implosion, this surface decouples from the ablation region. The effects of all major sources of perturbation leading to the initial seed of the deceleration-phase Rayleigh–Taylor (RT) instability have then been set. An example of the  $\bar{\sigma}$  scaling determined from 2-D *DRACO* simulations is shown in Fig. 102.27, where a comparison is made between the NIF  $\alpha = 3$  and OMEGA  $\alpha = 4$  designs.

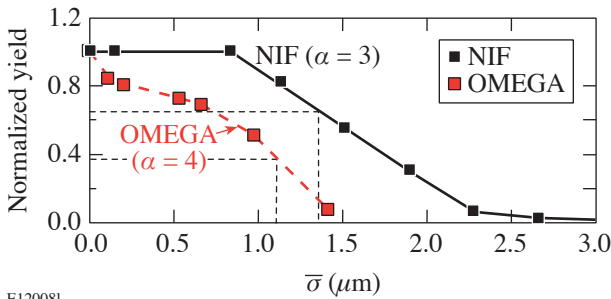


Figure 102.27 Comparison of the  $\bar{\sigma}$  stability analysis for OMEGA  $\alpha = 4$  and NIF  $\alpha = 3$  designs. All values were determined with the hydrocode *DRACO*.

From Fig. 102.27 it can be seen that the OMEGA implosions are more sensitive to the higher values of  $\bar{\sigma}$  than the NIF implosions. This is because the OMEGA targets have been energetically scaled from their NIF ignition counterparts. The physically smaller OMEGA targets are more sensitive than NIF targets when exposed to the same levels of nonuniformities. For identical values of  $\bar{\sigma}$ , the OMEGA implosions result in lower values of yield relative to 1-D simulations.

Using the  $\bar{\sigma}$  scaling with yield allows an experimental validation of the numerical modeling of current OMEGA experiments. This lends credibility to the ability of these numerical models to predict ignition for direct-drive target designs on the NIF. Using current NIF specifications for the allowed levels of perturbations (imprint, power imbalance,

and inner- and outer-surface roughness) results in a  $\bar{\sigma}$  value of  $\sim 1.4$  for the NIF capsule with a gain of  $\sim 30$  (see McKenty *et al.*<sup>2</sup>). The corresponding OMEGA implosion would have a  $\bar{\sigma}$  value of  $\sim 1.1$  and a performance YOC of  $\sim 40\%$ . These conditions are denoted as the dashed lines in Fig. 102.28, representing the performance of OMEGA implosions required for the validation of the ignition design.

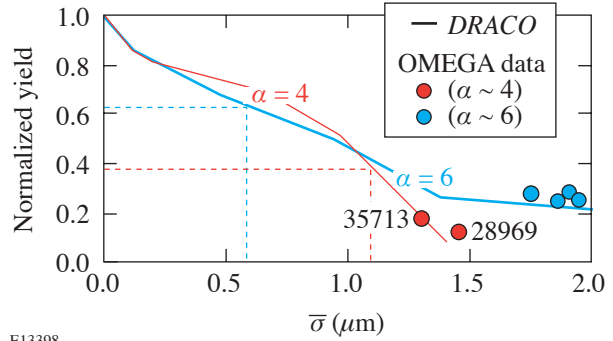


Figure 102.28 Comparison of *DRACO* predictions of yield reduction as a function of  $\bar{\sigma}$  for  $\alpha \sim 4$  and  $\alpha \sim 6$  experiments on OMEGA.

Figure 102.28 illustrates the  $\bar{\sigma}$  scaling for both the OMEGA  $\alpha \sim 4$  and previous  $\alpha \sim 6$  implosions. While it appears that  $\bar{\sigma}$  scales the same for the  $\alpha \sim 4$  and  $\alpha \sim 6$  implosions, one must remember that  $\bar{\sigma}$  represents the outcome of Rayleigh–Taylor growth of perturbation seeds during the acceleration phase of the implosion. Identical initial perturbations imposed during  $\alpha \sim 4$  and  $\alpha \sim 6$  target implosions will not result in the same  $\bar{\sigma}$  value. The separate stability characteristics of the two implosions determine the final  $\bar{\sigma}$  value for each target. As such, the  $\alpha \sim 6$  implosions, due to their enhanced stability relative to the  $\alpha \sim 4$  implosions, have resultant  $\bar{\sigma}$  values that are lower than  $\alpha \sim 4$  implosions with comparable initial conditions. The  $\bar{\sigma}$  parameter (extracted from *DRACO* simulations) has been used to plot the experimental yield performance on the graph in Fig. 102.28 for recent OMEGA experiments. The experimental points are in good agreement with the  $\bar{\sigma}$  scaling. As target-layer uniformity and OMEGA irradiation uniformity are improved, the  $\alpha \sim 4$  implosion experiments are expected to approach the  $\sim 40\%$  YOC goal.

Additional results obtained from all  $\alpha \sim 6$  and  $\alpha \sim 4$  implosions with ice quality better than  $5\text{-}\mu\text{m}$  rms and target offset  $< 42\ \mu\text{m}$  are shown in Fig. 102.29. The YOC for the experimen-

tal data is compared with the trends of two series of *DRACO* simulations run with varying initial ice roughness for no offset and for a 30- $\mu\text{m}$  offset from target chamber center. The effects of laser imprint are included in all of the *DRACO* simulations. The *DRACO* simulations are in good agreement with the YOC values and, therefore, explain yield reduction as due principally to the ice-layer roughness and target offset.

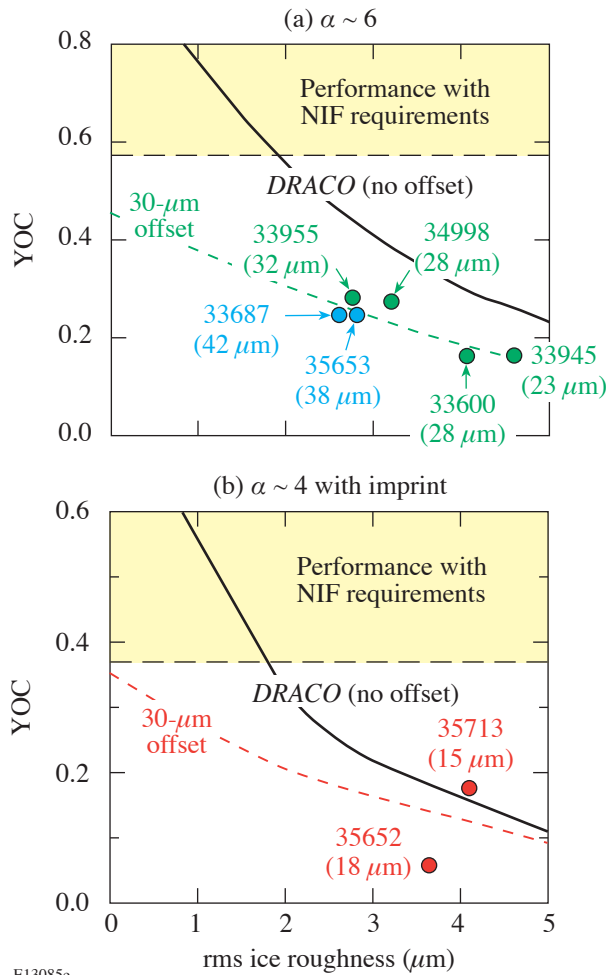


Figure 102.29 Comparison of YOC to *DRACO* predictions for (a)  $\alpha \sim 6$  and (b)  $\alpha \sim 4$  experiments on OMEGA as a function of ice roughness and target offset. Lower curves are *DRACO*-simulated YOC for a 30- $\mu\text{m}$  target offset.

## Conclusions

In summary, recent cryogenic,  $\text{D}_2$  direct-drive implosions on the OMEGA Laser System are showing good agreement with numerical simulations. Measurement and simulation of absorption agree closely (within  $\pm 2\%$ ), enabling the accurate

design of pulse shapes that maintain the fuel on a calculated adiabat of as low as  $\sim 4$ . Areal densities of as high as  $\sim 100 \text{ mg/cm}^2$  for temperatures of  $\sim 2$  to 3 keV result from implosions that have low ice roughness, low target offset, and low calculated fuel adiabat. Resulting fusion yields are well explained by 2-D simulations, and the expected reduction of yield from 1-D is currently limited by the ice roughness and target offset. Extrapolation to conditions on the NIF result in high gain ( $\geq 30$ ), increasing confidence in the direct-drive approach to ICF ignition.

## ACKNOWLEDGMENT

The authors are extremely grateful to the staff of the Laboratory for Laser Energetics for their tireless dedication to the cryogenic implosion program and the operation of the OMEGA laser system. In particular, the authors would like to acknowledge the efforts of the Cryogenic Target Fabrication Group for the production of layered and characterized capsules on a regular schedule. This work was supported by the U. S. Department of Energy Office of Inertial Confinement Fusion under Cooperative Agreement No. DE-FC52-92SF19460, the University of Rochester, and the New York State Energy Research and Development Authority. The support of the DOE does not constitute an endorsement by the DOE of the views expressed in this article.

## REFERENCES

1. J. Nuckolls *et al.*, *Nature* **239**, 139 (1972).
2. P. W. McKenty, V. N. Goncharov, R. P. J. Town, S. Skupsky, R. Betti, and R. L. McCrory, *Phys. Plasmas* **8**, 2315 (2001).
3. S. Skupsky, R. Betti, T. J. B. Collins, V. N. Goncharov, D. R. Harding, R. L. McCrory, P. W. McKenty, D. D. Meyerhofer, and R. P. J. Town, in *Inertial Fusion Sciences and Applications 2001*, edited by K. Tanaka, D. D. Meyerhofer, and J. Meyer-ter-Vehn (Elsevier, Paris, 2002), pp. 240–245.
4. R. Betti, V. N. Goncharov, R. L. McCrory, and C. P. Verdon, *Phys. Plasmas* **5**, 1446 (1998).
5. M. C. Herrmann, M. Tabak, and J. D. Lindl, *Nucl. Fusion* **41**, 99 (2001).
6. J. Meyer-ter-Vehn, *Nucl. Fusion* **22**, 561 (1982).
7. V. N. Goncharov, J. P. Knauer, P. W. McKenty, P. B. Radha, T. C. Sangster, S. Skupsky, R. Betti, R. L. McCrory, and D. D. Meyerhofer, *Phys. Plasmas* **10**, 1906 (2003).
8. T. R. Boehly, D. L. Brown, R. S. Craxton, R. L. Keck, J. P. Knauer, J. H. Kelly, T. J. Kessler, S. A. Kumpan, S. J. Loucks, S. A. Letzring, F. J. Marshall, R. L. McCrory, S. F. B. Morse, W. Seka, J. M. Soures, and C. P. Verdon, *Opt. Commun.* **133**, 495 (1997).
9. Laboratory for Laser Energetics LLE Review **81**, 6, NTIS document No. DOE/SF/19460-335 (1999). Copies may be obtained from the National Technical Information Service, Springfield, VA 22161.
10. C. Stoeckl, C. Chiritescu, J. A. Delettrez, R. Epstein, V. Yu. Glebov, D. R. Harding, R. L. Keck, S. J. Loucks, L. D. Lund, R. L. McCrory, P. W. McKenty, F. J. Marshall, D. D. Meyerhofer, S. F. B. Morse, S. P. Regan, P. B. Radha, S. Roberts, T. C. Sangster, W. Seka, S. Skupsky,

- V. A. Smalyuk, C. Sorce, J. M. Soures, R. P. J. Town, J. A. Frenje, C. K. Li, R. D. Petrasso, F. H. Séguin, K. Fletcher, S. Padalino, C. Freeman, N. Izumi, R. Lerche, and T. W. Phillips, *Phys. Plasmas* **9**, 2195 (2002).
11. W. R. Donaldson, R. Boni, R. L. Keck, and P. A. Jaanimagi, *Rev. Sci. Instrum.* **73**, 2606 (2002).
12. M. C. Richardson, P. W. McKenty, F. J. Marshall, C. P. Verdon, J. M. Soures, R. L. McCrory, O. Barnouin, R. S. Craxton, J. Delettrez, R. L. Hutchison, P. A. Jaanimagi, R. Keck, T. Kessler, H. Kim, S. A. Letzring, D. M. Roback, W. Seka, S. Skupsky, B. Yaakobi, S. M. Lane, and S. Prussin, in *Laser Interaction and Related Plasma Phenomena*, edited by H. Hora and G. H. Miley (Plenum Publishing, New York, 1986), Vol. 7, pp. 421–448.
13. T. J. Kessler, Y. Lin, J. J. Armstrong, and B. Velazquez, in *Laser Coherence Control: Technology and Applications*, edited by H. T. Powell and T. J. Kessler (SPIE, Bellingham, WA, 1993), Vol. 1870, pp. 95–104.
14. T. R. Boehly, V. A. Smalyuk, D. D. Meyerhofer, J. P. Knauer, D. K. Bradley, R. S. Craxton, M. J. Guardalben, S. Skupsky, and T. J. Kessler, *J. Appl. Phys.* **85**, 3444 (1999).
15. S. Skupsky, R. W. Short, T. Kessler, R. S. Craxton, S. Letzring, and J. M. Soures, *J. Appl. Phys.* **66**, 3456 (1989).
16. F. J. Marshall, J. A. Delettrez, R. Epstein, R. Forties, V. Yu. Glebov, J. H. Kelly, T. J. Kessler, J. P. Knauer, P. W. McKenty, S. P. Regan, V. A. Smalyuk, C. Stoeckl, J. A. Frenje, C. K. Li, R. D. Petrasso, and F. H. Séguin, *Bull. Am. Phys. Soc.* **48**, 56 (2003).
17. F. J. Marshall, J. A. Delettrez, R. Epstein, R. Forties, R. L. Keck, J. H. Kelly, P. W. McKenty, S. P. Regan, and L. J. Waxer, *Phys. Plasmas* **11**, 251 (2004).
18. R. C. Malone, R. L. McCrory, and R. L. Morse, *Phys. Rev. Lett.* **34**, 721 (1975).
19. J. Delettrez, *Can. J. Phys.* **64**, 932 (1986).
20. W. Seka, C. Stoeckl, V. N. Goncharov, R. E. Bahr, T. C. Sangster, R. S. Craxton, J. A. Delettrez, A. V. Maximov, J. Myatt, A. Simon, and R. W. Short, *Bull. Am. Phys. Soc.* **49**, 179 (2004).
21. C. Stoeckl, V. Yu. Glebov, S. Roberts, T. C. Sangster, R. A. Lerche, R. L. Griffith, and C. Sorce, *Rev. Sci. Instrum.* **74**, 1713 (2003).
22. R. D. Petrasso, J. A. Frenje, C. K. Li, F. H. Séguin, J. R. Rygg, B. E. Schwartz, S. Kurebayashi, P. B. Radha, C. Stoeckl, J. M. Soures, J. Delettrez, V. Yu. Glebov, D. D. Meyerhofer, and T. C. Sangster, *Phys. Rev. Lett.* **90**, 095002 (2003).
23. V. A. Smalyuk, P. B. Radha, J. A. Delettrez, V. Yu. Glebov, V. N. Goncharov, D. D. Meyerhofer, S. P. Regan, S. Roberts, T. C. Sangster, J. M. Soures, C. Stoeckl, J. A. Frenje, C. K. Li, R. D. Petrasso, and F. H. Séguin, *Phys. Rev. Lett.* **90**, 135002 (2003).
24. J. A. Frenje, C. K. Li, F. H. Séguin, J. Deciantis, S. Kurebayashi, J. R. Rygg, R. D. Petrasso, J. Delettrez, V. Yu. Glebov, C. Stoeckl, F. J. Marshall, D. D. Meyerhofer, T. C. Sangster, V. A. Smalyuk, and J. M. Soures, *Phys. Plasmas* **11**, 2798 (2003).
25. F. J. Marshall, J. A. Delettrez, R. Epstein, and B. Yaakobi, *Phys. Rev. E* **49**, 4381 (1994).
26. D. Keller, T. J. B. Collins, J. A. Delettrez, P. W. McKenty, P. B. Radha, B. Whitney, and G. A. Moses, *Bull. Am. Phys. Soc.* **44**, 37 (1999).

# Stopping, Straggling, and Blooming of Directed Energetic Electrons in Hydrogenic Plasmas

A basic problem in plasma physics is the interaction and energy loss of energetic, charged particles in plasmas,<sup>1–3</sup> including the effects of penetration, longitudinal straggling, and lateral blooming. This problem has traditionally focused on ions (i.e., protons, alphas, etc.), either in the context of heating and/or ignition in, for example, inertially confined plasmas (ICF)<sup>3–7</sup> or the use of these particles for diagnosing implosion dynamics.<sup>8</sup> More recently, prompted in part by the concept of fast ignition (FI) for ICF,<sup>9</sup> studies have begun to consider energy deposition from relativistic fast electrons in deuterium–tritium (DT) plasmas.<sup>9–14</sup> In this context, the mean penetration and stopping power for energetic electrons interacting with a uniform hydrogenic plasma of arbitrary density and temperature were recently calculated. Therein, the randomizing effect of electron scattering, which has a cumulative effect of bending the path of the electrons away from their initial direction, was linked to energy loss.<sup>14</sup> This article presents calculations that show, for the first time, the effects of longitudinal straggling and transverse blooming and their inextricable relationship with enhanced electron energy deposition. It is demonstrated that, while the initial penetration results in approximate uniform energy deposition, the latter penetration has mutual couplings of energy loss, straggling, and blooming that lead to an extended region of enhanced, nonuniform energy deposition. This present work is important for quantitatively evaluating the energy deposition in several current problems. In the case of FI, for example, no evaluations have treated either straggling or blooming upon the energy deposition; without evaluation no confident assessment of ignition requirements can be made. Therefore, the calculations in this article form the foundation for a baseline, at the very least, or an accurate assessment, at the very most, by which to evaluate these effects upon fast ignition. In addition to FI, these calculations are, in general, sufficient to be of relevance to other current problems, such as fast-electron preheat<sup>15</sup> in ICF, or to energy deposition of relativistic electrons in astrophysical jets.<sup>16</sup>

To delineate these processes, we calculate the different moments by analytically solving an integro-differential diffusion equation,<sup>17</sup> thereby rigorously determining the angular and spatial distributions of the scattered electrons:

$$\frac{\partial f}{\partial s} + \mathbf{v} \cdot \nabla f = n_i \int [f(\mathbf{x}, \mathbf{v}', s) - f(\mathbf{x}, \mathbf{v}, s)] \sigma(|\mathbf{v} - \mathbf{v}'|) d\mathbf{v}', \quad (1)$$

where  $f(\mathbf{x}, \mathbf{v}, s)$  is the distribution function,  $n_i$  is the number density of fully ionized plasma ions of charge  $Z$ ,  $\mathbf{x}$  is the position where scattering occurs,  $\sigma = \sigma_{ei} + Z\sigma_{ee}$  is the total scattering cross section with  $\sigma_{ei}$  the Rutherford  $e$ -ion cross section<sup>18</sup> and  $\sigma_{ee}$  the Møller  $e$ - $e$  cross section.<sup>19</sup> We solve this equation in cylindrical coordinates with the assumption that the scattering is azimuthally symmetric. After expanding the distribution in spherical harmonics and substituting into Eq. (1), two differential equations for the longitudinal and lateral distributions are obtained. For the longitudinal distribution,

$$\frac{\partial F_{\ell m}^n(s)}{\partial s} + \kappa_{\ell}(s) F_{\ell m}^n(s) - n \left[ \frac{\ell}{\sqrt{4\ell^2 - 1}} F_{\ell-1, m}^{n-1}(s) + \frac{\ell+1}{\sqrt{4(\ell+1)^2 - 1}} F_{\ell+1, m}^{n-1}(s) \right] = 0, \quad (2)$$

and for the lateral distribution,

$$\begin{aligned}
 & \frac{\partial F_{\ell m}^n(s)}{\partial s} + \kappa_{\ell}(s) F_{\ell m}^n(s) \\
 & - \frac{n}{2} \left[ \sqrt{\frac{(\ell+m)(\ell+m-1)}{4\ell^2-1}} F_{\ell-1, m-1}^{n-1}(s) \right. \\
 & + \sqrt{\frac{(\ell+m+2)(\ell+m+1)}{4(\ell+1)^2-1}} F_{\ell+1, m+1}^{n-1}(s) \\
 & - \sqrt{\frac{(\ell-m)(\ell-m-1)}{4\ell^2-1}} F_{\ell-1, m+1}^{n-1}(s) \\
 & \left. - \sqrt{\frac{(\ell-m+2)(\ell-m+1)}{4(\ell+1)^2-1}} F_{\ell+1, m+1}^{n-1}(s) \right] = 0, \quad (3)
 \end{aligned}$$

where the moments are defined as

$$F_{\ell m}^n(s) = \int_{-\infty}^{\infty} x_j^n f_{\ell m}(\mathbf{x}, s) d\mathbf{x} \quad (4)$$

and  $j=1, 2, 3$  represents  $x, y, z$ , respectively.

$$\kappa_{\ell}(s) = n_i \int \left( \frac{d\sigma}{d\Omega} \right) [1 - P_{\ell}(\cos\theta)] d\Omega, \quad (5)$$

where  $P_{\ell}(\cos\theta)$  is the Legendre polynomial and  $\kappa_{\ell}(s)$  is directly related to the basic transport cross section.<sup>2</sup> Equations (2) and (3) are coupled to adjacent orders in  $n$  and are solved with the boundary condition

$$F_{\ell m}^n(s) = \sqrt{\frac{2\ell+1}{4\pi}} \delta_{m0} \delta_{n0} \exp \left[ - \int_0^s \kappa_{\ell}(s') ds' \right], \quad (6)$$

where  $F_{\ell m}^n(0) = 0$  for  $n \neq 0$ . Solving for  $\kappa_1$  and  $\kappa_2$ ,

$$\kappa_1 = 4\pi n_i \left( \frac{r_0}{\gamma\beta^2} \right)^2 \left\{ Z^2 \ln \Lambda^{ei} + \frac{4(\gamma+1)^2}{\left[ 2\sqrt{(\gamma+1)/2} \right]^4} Z \ln \Lambda^{ee} \right\}; \quad (7)$$

and

$$\begin{aligned}
 \kappa_2 &= 12\pi n_i \left( \frac{r_0}{\gamma\beta^2} \right)^2 \\
 & \times \left\{ Z^2 \left( \ln \Lambda^{ei} - \frac{1}{2} \right) + \frac{4(\gamma+1)^2}{\left[ 2\sqrt{(\gamma+1)/2} \right]^4} Z \left( \ln \Lambda^{ee} - \frac{1}{2} \right) \right\}. \quad (8)
 \end{aligned}$$

$\kappa_1$  is related to the slowing-down cross section,<sup>2</sup> which characterizes the loss of directed velocity in the scattering, and  $\kappa_2$  is related to the deflection cross section, which represents the mean-square increment in the transverse electron velocity during the scattering process.<sup>2</sup>  $\beta = v/c$  and  $\gamma = (1 - \beta^2)^{-1/2}$ ;  $r_0 = e^2/m_0c^2$  is the classical electron radius. The appropriate Coulomb logarithms are evaluated in an earlier paper.<sup>14</sup> The angular distribution function is obtained from

$$\begin{aligned}
 f(\theta, E) &= \frac{1}{4\pi} \sum_{\ell=0}^{\infty} (2\ell+1) P_{\ell}(\cos\theta) \\
 & \times \exp \left[ - \int_{E_0}^E \kappa_{\ell}(E') \left( \frac{dE'}{ds} \right)^{-1} dE' \right], \quad (9)
 \end{aligned}$$

from which  $\langle P_{\ell}(\cos\theta) \rangle$  is calculated:

$$\langle P_{\ell}(\cos\theta) \rangle = \exp \left[ - \int_{E_0}^E \kappa_{\ell}(E') \left( \frac{dE'}{ds} \right)^{-1} dE' \right], \quad (10)$$

where  $dE/ds$  is plasma stopping power taken from Ref. 14. From these results, Eqs. (2) and (3) are solved, and basic moments required for the calculation of the longitudinal and lateral distributions are evaluated:

$$\langle x \rangle = \int_{E_0}^E \langle P_1(\cos\theta) \rangle \left( \frac{dE'}{ds} \right)^{-1} dE', \quad (11)$$

which was evaluated in previous work for the case of 1-MeV electron stopping in a 300-g/cm<sup>3</sup> DT plasma at 5 keV. This results in a penetration of 13.9  $\mu\text{m}$  (Ref. 14). For astrophysical jets, however, for which  $n_e \sim 10/\text{cm}^3$ , the penetration is  $\sim 10^4$  light years:

$$\begin{aligned} \langle x^2 \rangle &= \frac{2}{3} \int_{E_0}^E \langle P_1(\cos\theta) \rangle \left( \frac{dE'}{ds} \right)^{-1} \\ &\times \left[ \int_{E_0}^{E'} \frac{1 + 2 \langle P_2(\cos\theta) \rangle}{\langle P_1(\cos\theta) \rangle} \left( \frac{dE''}{ds} \right)^{-1} dE'' \right] dE', \quad (12) \end{aligned}$$

because of azimuthal symmetry,

$$\langle y \rangle = \langle z \rangle = 0, \quad (13)$$

and

$$\begin{aligned} \langle y^2 \rangle = \langle z^2 \rangle &= \frac{2}{3} \int_{E_0}^E \langle P_1(\cos\theta) \rangle \left( \frac{dE'}{ds} \right)^{-1} \\ &\times \left[ \int_{E_0}^{E'} \frac{1 - \langle P_2(\cos\theta) \rangle}{\langle P_1(\cos\theta) \rangle} \left( \frac{dE''}{ds} \right)^{-1} dE'' \right] dE'. \quad (14) \end{aligned}$$

Range or longitudinal straggling is defined by

$$\Sigma_R(E) = \sqrt{\langle x^2 \rangle - \langle x \rangle^2}. \quad (15)$$

Beam blooming is defined by

$$\Sigma_B(E) = \sqrt{\langle y^2 \rangle}. \quad (16)$$

Figure 102.30 shows the calculated straggling [Fig. 102.30(a)] and blooming [Fig. 102.30(b)] that result from the effects of scattering off electrons alone and off electrons plus ions. Energy deposition, toward the end of the penetration, is transferred to an extended region about the mean penetration of 13.8  $\mu\text{m}$ , specifically  $\sim \pm 3 \mu\text{m}$  longitudinally and  $\sim \pm 5 \mu\text{m}$  laterally. From a different point of view, Fig. 102.31 shows the

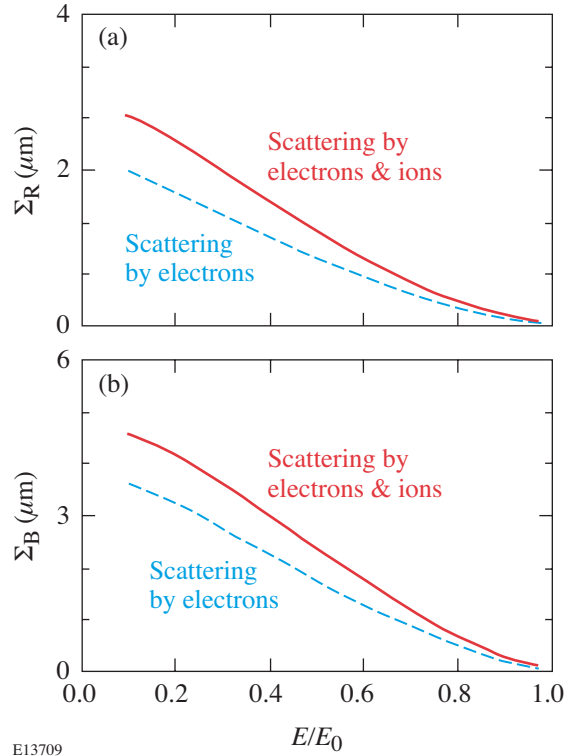
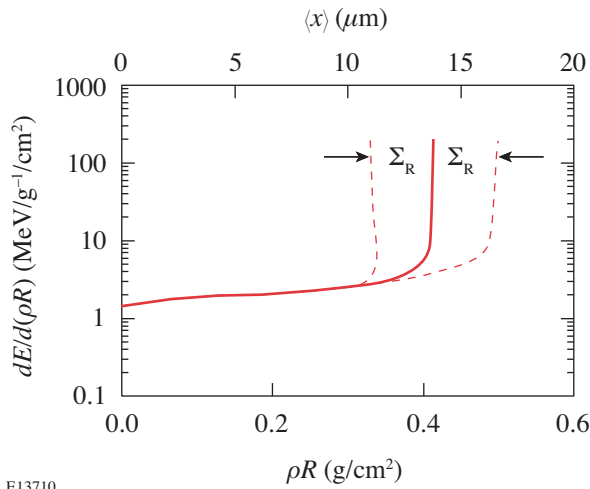


Figure 102.30  
For 1-MeV electrons in a DT plasma ( $\rho = 300 \text{ g/cm}^3$ ,  $T_e = 5 \text{ keV}$ ): (a) The calculated range straggling  $\Sigma_R(E)$  and (b) lateral blooming  $\Sigma_B(E)$  are plotted as functions of electron residual energy. For this case, the penetration  $\langle x \rangle$  is 13.9  $\mu\text{m}$  (Ref. 14).

enhancement of the stopping power in the extended region in which longitudinal straggling is important. Including the effects of blooming would effectively increase (decrease)  $\Sigma_R$  for values less (greater) than the mean penetration.



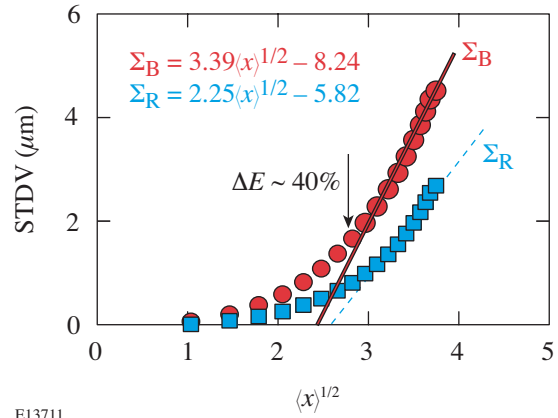
E13710

Figure 102.31

The stopping power, plotted as a function of the electron penetration. The solid line represents the mean energy loss, while the two dashed lines indicate the straggling range over which energy is effectively spread (in this plot, important contributions from blooming are not included; see text). As a result of the scattering, the energy transfer increases notably near the end of the penetration (i.e., an effective Bragg peak).

Figure 102.32 shows the effects of both straggling and blooming as a function of the square root of the penetration. Note that little straggling or blooming occurs until the 1-MeV electrons have traversed a significant portion of the final penetration (~60%, corresponding to only ~40% energy loss). Therefore, the assumption of uniform energy deposition, used in some previous calculations,<sup>11</sup> has some approximate justification for only the first ~40% of the energy loss. For energy loss greater than 40%, both straggling and blooming expand linearly with the square root of the penetration, an effect associated with the enhanced energy loss of the effective Bragg peak (Fig. 102.31). As a direct consequence of these multiple scattering effects, these results demonstrate the inextricable linkage between enhanced energy loss, straggling, and blooming.

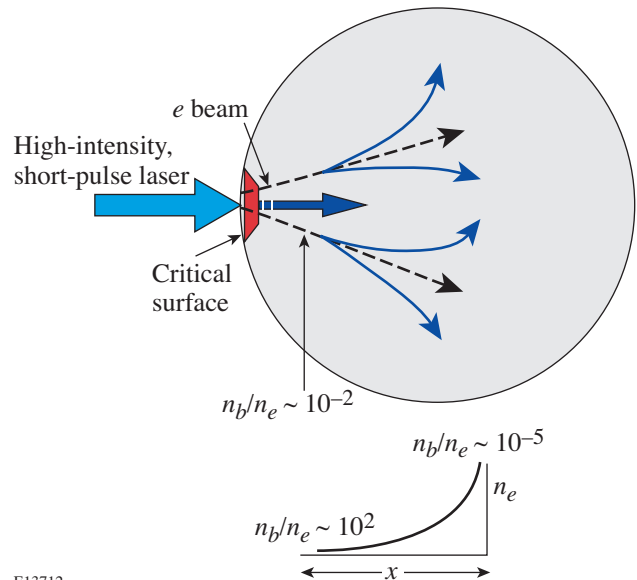
Figure 102.33 shows a schematic representation of an FI capsule. The relativistic electrons are generated by an intense laser interacting at the critical surface. As the electrons are initially generated and transported, they are subject to Weibel-like instabilities,<sup>20,21</sup> which can cause both spreading and



E13711

Figure 102.32

The longitudinal range straggling and lateral blooming of a 1-MeV electron beam, plotted as a function of the square root of the penetration ( $\langle x \rangle$ ), for conditions of Fig. 102.30. Note that when the electrons have lost more than ~40% of their energy, both  $\Sigma_R$  and  $\Sigma_B$  are approximately proportional to  $\sqrt{\langle x \rangle}$ . Equations listed in the figure are the results of fitting only this final portion of the penetration.



E13712

Figure 102.33

Schematic illustration of beam blooming in a precompressed FI capsule. Two distinct regions for electron transport are illustrated: first, when  $n_b/n_e > 10^{-2}$ , the electron transport is highly filamented due to Weibel-like instabilities that dominate energy loss and beam blooming; however, for  $n_b/n_e < 10^{-2}$ , which occurs as the beam penetrates farther into the denser portion of the capsule, Weibel-like instabilities are stabilized and the electrons are then subject to the multiple scattering, straggling, and blooming processes described herein. The dashed lines schematically indicate electron-beam trajectories without the effects of multiple scattering blooming and straggling (see text).

energy loss in this region. However, for electrons that transport farther into the increased-density portions of the capsule  $n_b/n_e < 10^{-2}$ , Weibel-like instabilities are stabilized and the electrons then become subject to the multiple scattering processes described herein. In this regime, the interaction can be envisioned as the linear superposition of individual, isolated electrons interacting with plasma. Therefore, these scattering processes, which involve energy loss, straggling, and beam blooming, become the ultimate mechanism that determines the details of energy deposition, whether in the dense core or outside, and ultimately determine the effectiveness of capsule ignition. From a different point of view, the extent of beam blooming and straggling is critical for FI target design since the finite size of the highly compressed core requires accurate understanding and control of beam divergence, which, if too severe, will preclude ignition.

In summary, from fundamental principles, the interaction of directed energetic electrons with hydrogenic plasmas is analytically modeled. For the first time, the effects of stopping, straggling, and beam blooming—a consequence of multiple scattering and energy loss—are rigorously treated from a unified approach. For fast ignition, enhanced energy deposition is found to be inextricably linked to beam blooming and straggling. We demonstrate that the mutual interaction of these effects will lead to an enhanced nonuniform region of energy deposition. Blooming and straggling effects will eventually dominate over all other sources of beam divergence and are therefore critical for evaluating the requirements of fast ignition.

#### ACKNOWLEDGMENT

This work was supported in part by U.S. Department of Energy Contract #DE-FG03-99SF21782, LLE subcontract #PO410025G, LLNL subcontract #B313975, and the Fusion Science Center for Extreme States of Matter and Fast Ignition Physics at University of Rochester.

#### REFERENCES

1. L. Spitzer, *Physics of Fully Ionized Gases*, 2nd rev. ed., Interscience Tracts on Physics and Astronomy (Interscience, New York, 1962).
2. B. A. Trubnikov, in *Reviews of Plasma Physics*, edited by M. A. Leontovich (Consultants Bureau, New York, 1965).
3. C. K. Li and R. D. Petrasso, *Phys. Rev. Lett.* **70**, 3063 (1993).
4. J. D. Lindl, *Inertial Confinement Fusion: The Quest for Ignition and Energy Gain Using Indirect Drive* (Springer-Verlag, New York, 1998).
5. J. D. Lindl, R. L. McCrory, and E. M. Campbell, *Phys. Today* **45**, 32 (1992).
6. S. Skupsky, *Phys. Rev. A* **16**, 727 (1977).
7. C. K. Li and R. D. Petrasso, *Phys. Rev. Lett.* **70**, 3059 (1993).
8. R. D. Petrasso, J. A. Frenje, C. K. Li, F. H. Séguin, J. R. Rygg, B. E. Schwartz, S. Kurebayashi, P. B. Radha, C. Stoeckl, J. M. Soures, J. Delettrez, V. Yu. Glebov, D. D. Meyerhofer, and T. C. Sangster, *Phys. Rev. Lett.* **90**, 095002 (2003); V. A. Smalyuk, P. B. Radha, J. A. Delettrez, V. Yu. Glebov, V. N. Goncharov, D. D. Meyerhofer, S. P. Regan, S. Roberts, T. C. Sangster, J. M. Soures, C. Stoeckl, J. A. Frenje, C. K. Li, R. D. Petrasso, and F. H. Séguin, *Phys. Rev. Lett.* **90**, 135002 (2003); F. H. Séguin, J. A. Frenje, C. K. Li, D. G. Hicks, S. Kurebayashi, J. R. Rygg, B.-E. Schwartz, R. D. Petrasso, S. Roberts, J. M. Soures, D. D. Meyerhofer, T. C. Sangster, J. P. Knauer, C. Sorce, V. Yu. Glebov, C. Stoeckl, T. W. Phillips, R. J. Leeper, K. Fletcher, and S. Padalino, *Rev. Sci. Instrum.* **74**, 975 (2003); J. A. Frenje, C. K. Li, and F. H. Séguin, *Phys. Plasmas* **11**, 2798 (2004).
9. M. Tabak *et al.*, *Phys. Plasmas* **1**, 1626 (1994).
10. C. Deutsch *et al.*, *Phys. Rev. Lett.* **77**, 2483 (1996); **85**, 1140 (E) (2000).
11. S. Atzeni, *Phys. Plasmas* **6**, 3316 (1999).
12. M. H. Key, M. D. Cable, T. E. Cowan, K. G. Estabrook, B. A. Hammel, S. P. Hatchett, E. A. Henry, D. E. Hinkel, J. D. Kilkenny, J. A. Koch, W. L. Kruer, A. B. Langdon, B. F. Lasinski, R. W. Lee, B. J. MacGowan, A. MacKinnon, J. D. Moody, M. J. Moran, A. A. Offenberger, D. M. Pennington, M. D. Perry, T. J. Phillips, T. C. Sangster, M. S. Singh, M. A. Stoyer, M. Tabak, G. L. Tietbohl, M. Tsukamoto, K. Wharton, and S. C. Wilks, *Phys. Plasmas* **5**, 1966 (1998).
13. C. Ren *et al.*, *Phys. Rev. Lett.* **93**, 185004 (2004).
14. C. K. Li and R. D. Petrasso, *Phys. Rev. E* **70**, 067401 (2004).
15. M. D. Rosen *et al.*, *Phys. Rev. A* **36**, 247 (1987).
16. P. A. Hughes, ed. *Beams and Jets in Astrophysics*, Cambridge Astrophysics Series (Cambridge University Press, Cambridge, England, 1991).
17. H. W. Lewis, *Phys. Rev.* **78**, 526 (1950).
18. N. F. Mott, *Proc. R. Soc. Lond. A, Math. Phys. Sci.* **A124**, 425 (1929); N. F. Mott, M. A. Gonville, and C. College, *Proc. R. Soc. Lond. A, Math. Phys. Sci.* **CXXXV**, 429 (1932).
19. Chr. Møller, *Ann. Phys.* **14**, 531 (1932).
20. E. S. Weibel, *Phys. Rev. Lett.* **2**, 83 (1959).
21. M. Honda, J. Meyer-ter-Vehn, and A. Pukhov, *Phys. Rev. Lett.* **85**, 2128 (2000).

---

# Multidimensional Analysis of Direct-Drive, Plastic-Shell Implosions on OMEGA

## Introduction

In direct-drive inertial confinement fusion (ICF),<sup>1</sup> nominally identical beams heat and compress a nearly spherical shell containing low-density gas. The high-density shell is unstable due to the Rayleigh–Taylor instability (RT)<sup>2</sup> at the ablation surface when the low-density blowoff plasma accelerates it. The target becomes RT unstable again, but at the inner fuel–shell interface or inner shell surface, later in the implosion when the lower-density gas decelerates the cold shell. Nonuniformities associated with the target, beam-to-beam power imbalance, and the individual beams seed this instability growth during both acceleration and deceleration phases. This compromises the uniformity of compression and degrades target performance.

Direct-drive-ignition designs require a cryogenic DT-ice layer imploded by a “shaped” pulse, with a long, low-intensity foot and a relatively slow rise to peak intensity.<sup>3</sup> This article discusses warm, plastic-shell targets<sup>4,5</sup> imploded on the OMEGA<sup>6</sup> laser with a 1-ns square pulse, characterized by an initial sharp rise to peak intensity. Plastic-shell implosions are more susceptible to instability growth than cryogenic targets during both the acceleration and deceleration phases. The in-flight aspect ratio (IFAR; defined as the ratio of the shell position to the shell thickness when the shell has moved about half the total acceleration distance) of plastic shells discussed in this article is between 80 and 110, significantly larger than the ignition-design IFAR of ~60 (Ref. 3). The number of  $e$ -foldings due to RT growth increases for a larger IFAR.<sup>7</sup> Consequently, plastic shells are more unstable during the acceleration phase than cryogenic shells. Plastic shells have two unstable surfaces during the deceleration phase: the gas–plastic (fuel–shell) interface whose growth dominates for all wavelengths, and the rear shell surface where short-wavelength growth is reduced due to a finite-density scale length. In contrast, during the deceleration phase, cryogenic targets are unstable only at the rear shell surface where finite density scale lengths and ablation<sup>8</sup> (in the case of ignition targets) can significantly reduce growth rates of  $\ell > 50$ , where  $\ell$  is the Legendre mode number. Implosions of warm plastic shells,

however, offer the advantage that complementary information of the compressed core can be obtained due to the variety of gas-fill types (D<sub>2</sub>, DT, D<sup>3</sup>He, etc.) and fill pressures. This variety is unavailable with ignition-scaled cryogenic targets. As a result, detailed verification of the multidimensional hydrodynamics due to the presence of target and laser asymmetries can be performed with plastic shells.

Experimental results from direct-drive plastic-shell implosions have been discussed previously in the literature. Meyerhofer *et al.*<sup>4</sup> first presented experimental results to infer core conditions. Radha *et al.*<sup>5</sup> first pointed out the presence of small-scale mix in these implosions. Complementary diagnostics<sup>6</sup> were employed to confirm this observation. However, the role of small-scale mix on target yields remained an outstanding question. Recently, 2-D simulations were employed by Radha *et al.*<sup>5</sup> to understand the role of laser and target nonuniformities on implosion performance. It was determined that small-scale mix is not the primary determinant of gross target performance as measured through yields. Instead, long ( $\ell \leq 10$ ) and intermediate ( $10 \leq \ell \leq 50$ ) wavelengths dominated performance for the thick, stable shells, and short wavelengths ( $\ell \leq 50$ ) determined target performance for the thin, unstable shells. In this article, this latter work has been extended to include a larger range of target types and fill pressures. In addition, a wider range of observables is compared to simulation results. This work summarizes simulations of plastic-shell implosions using the methods described in Ref. 5.

Imperfect illumination and target roughness seed the nonuniformity growth of hydrodynamic instabilities in direct-drive implosions. The incident laser irradiation on the target includes nonuniformities that result from energy and power imbalances among the beams and from nonuniformities within each beam. The former results in long-wavelength ( $\ell \leq 10$ , where  $\ell = 2\pi R/\lambda$  is the Legendre mode number,  $R$  is the target radius, and  $\lambda$  is the nonuniformity wavelength) perturbations that lead to deformations of the shell. The latter are manifest in the intermediate-wavelength ( $10 < \ell \leq 50$ ) and short-wavelength ( $\ell > 50$ ) nonuniformities that can lead to shell breakup

during the acceleration phase due to Rayleigh–Taylor growth. All of these sources of nonuniformity can lead to a disruption of final fuel assembly. Two-dimensional simulations of plastic-shell implosions that take these effects into account using the hydrodynamic code *DRACO*<sup>5</sup> are presented here. The modeling of multidimensional hydrodynamics is verified, leading to increased confidence in the predictions of direct-drive ignition<sup>3</sup> on the National Ignition Facility.<sup>9</sup> Simulation results are consistent with experimental observations.

The following sections (1) describe one-dimensional shell dynamics and laser drive, followed by nonuniformity seeding; (2) discuss the effect of short-wavelength growth on shell stability along with the effect of shell stability on experimental observables; (3) compare results from 2-D simulations to experimental results; and (4) present conclusions.

### Targets, Laser Drive, and Shell Dynamics

A variety of gas-filled plastic (CH) shells, with thicknesses varying from 15  $\mu\text{m}$  to 27  $\mu\text{m}$  [Fig. 102.34(a)], have been imploded on OMEGA. Four target configurations are primarily discussed in this article: 20- $\mu\text{m}$ -thick, 15-atm-fill; 20- $\mu\text{m}$ -thick, 3-atm-fill; 27- $\mu\text{m}$ -thick, 15-atm-fill; and 27- $\mu\text{m}$ -thick, 3-atm-fill. A 1-ns square pulse<sup>10</sup> [Fig. 102.34(b)] with  $\sim 23$  kJ of energy irradiates these targets with full beam smoothing [two-dimensional smoothing by spectral dispersion<sup>11</sup> (1-THz, 2-D SSD with one color cycle) with polarization smoothing (PS)<sup>12</sup>]. Simulations presented here are for targets irradiated using distributed phase plates (DPP's)<sup>13</sup> that have a super-Gaussian order  $\sim 2.26$  with a spot size (defined as the diameter that is  $1/e$  of peak intensity) of 616  $\mu\text{m}$  (SG3 phase plates).<sup>14</sup> More recently, phase plates on OMEGA have been upgraded to a super-Gaussian order  $\sim 4.12$  with a spot size of 716  $\mu\text{m}$  (SG4 phase plates) that primarily reduces the  $\ell \leq 50$  nonuniformity.<sup>14</sup> Comparison of observables between the SG3 and SG4 phase plates will also be presented to confirm the effect of laser nonuniformity on observables.

Plastic shells can be filled with a variety of gases at differing pressures that, during the implosion, provide a variety of nuclear and charged particles to diagnose implosion characteristics. Observables shown in this article include the primary neutron yield from the  $\text{D}_2$  reaction, the shell areal density ( $\rho R$ ) inferred from both the energy loss of the protons from the  $\text{D}^3\text{He}$  reaction<sup>15</sup> and the energy loss of the elastically scattered protons from the CH in DT-filled targets,<sup>16</sup> the neutron-averaged ion temperatures inferred from neutron time-of-flight measurements, and ion temperatures inferred from the ratio of the DD neutron to  $\text{D}^3\text{He}$  proton yields.<sup>15</sup> Time-resolved ob-

servations of neutron production rates<sup>17</sup> and x-ray image self-emission<sup>18</sup> are also routinely obtained. All of these experimental observables will be compared with results of simulations.

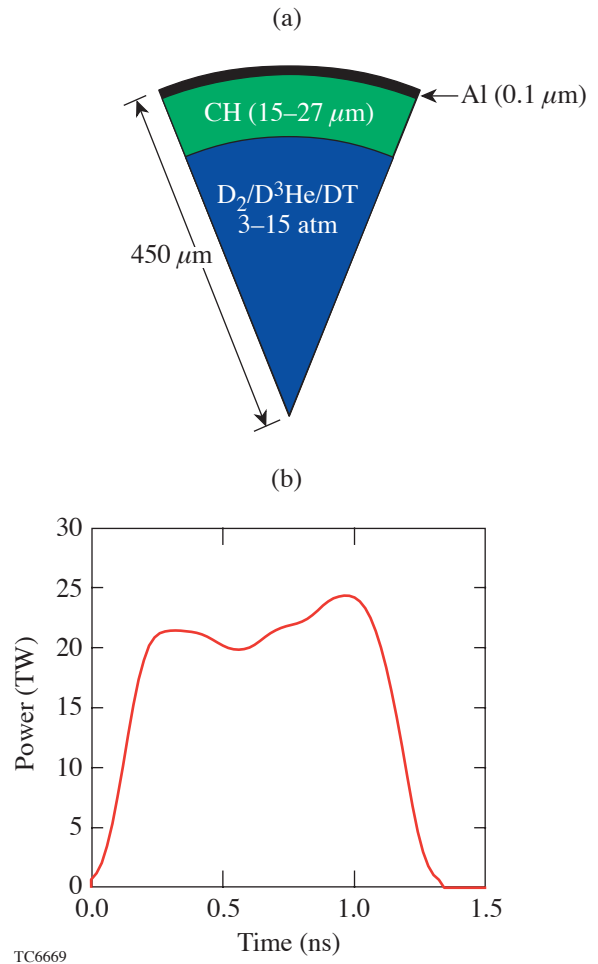


Figure 102.34

(a) Plastic-shell targets studied in this work. Two thicknesses—20  $\mu\text{m}$  and 27  $\mu\text{m}$ —with  $\text{D}_2$  fills at 3 and 15 atm are considered. (b) The pulse shape (1 ns square) used to irradiate these targets sets the shell on a relatively high adiabat ( $\sim 5$ ).

The one-dimensional (1-D) dynamics of plastic shells can be divided into four stages: shock transit, acceleration, coasting, and deceleration. Shock dynamics simulated using the 1-D hydrodynamic code *LILAC*<sup>19</sup> is shown in Fig. 102.35(a) as a contour plot of the gradient magnitude of the logarithm pressure,  $|\partial \ln P / \partial r|$ , as a function of Lagrangian coordinate and time. The target simulated in Fig. 102.35 has a shell thickness of 20  $\mu\text{m}$  and encloses  $\text{D}_2$  gas at a pressure of 15 atm. The dark lines correspond to shock trajectories. The dashed line is the trajectory of the fuel–shell interface. Since the rise

time of the laser is relatively fast ( $\sim 200$  ps), a strong shock is driven into the target. The rarefaction wave launched at the breakout of the shock ( $\sim 0.4$  ns) from the rear surface of the

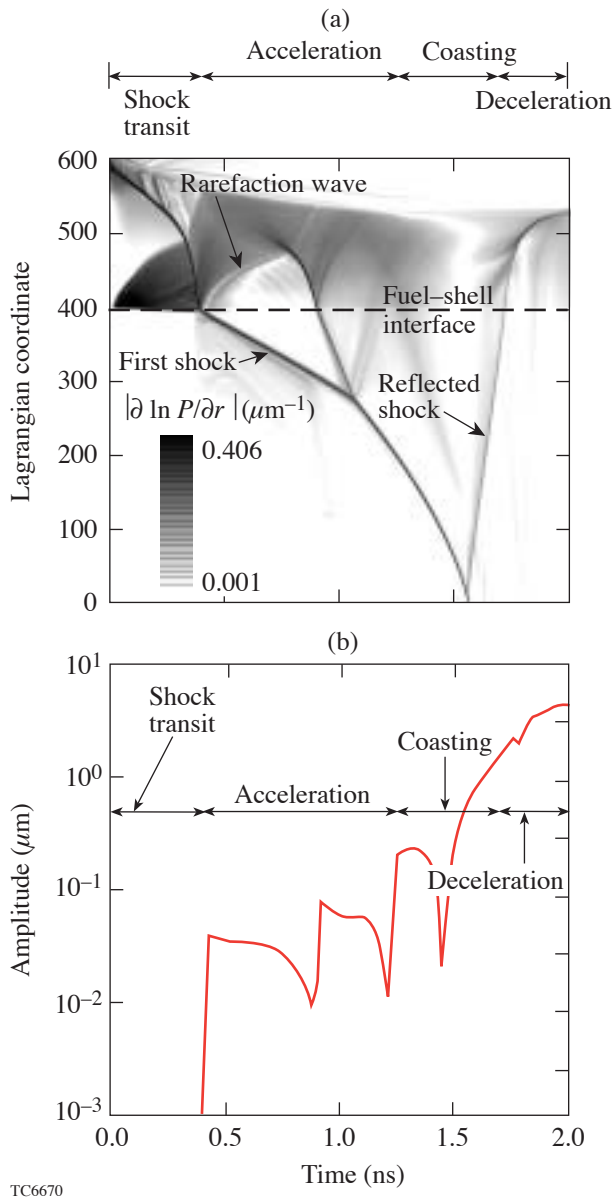


Figure 102.35

(a) Contour plot of the gradient magnitude of the natural log of the pressure for a  $20\text{-}\mu\text{m}$ -thick CH shell enclosing 15 atm of  $\text{D}_2$  gas. The y axis corresponds to the Lagrangian coordinate in the 1-D simulation. The darker contours correspond to shock trajectories. The dashed line is the fuel-shell interface. The duration of the four phases of the implosion (shock transit, acceleration, coasting, and deceleration) is also shown. (b) The growth of a single mode ( $\ell = 30$ ) at the fuel-shell interface through the implosion. The interface is seeded primarily by the shock and grows significantly during the coasting phase.

shell reaches the ablation surface, launching a compression wave into the target. At this time, the shell accelerates inward and the ablation surface is subject to RT growth.<sup>20</sup> The compression wave travels down the decreasing density gradient and breaks out of the rear surface of the shell as a shock (at  $\sim 0.8$  ns). The shocks meet in the gas (at  $\sim 1$  ns) before reaching the center.

The fuel-shell interface has a non-zero Atwood number ( $A_T = 0.18$  for  $\text{D}_2$  fills)<sup>5</sup> and is unstable for all wavelengths. The growth of a single mode at the fuel-shell interface simulated using the code *DRACO*<sup>5</sup> is shown in Fig. 102.35(b). The interface is primarily seeded by the shock ( $\sim 0.4$  ns). The acceleration phase occurs after shock transit until  $\sim 1.4$  ns, during which feedthrough from the RT growth at the ablation surface plays an important role in increasing the nonuniformity at the fuel-shell interface. For the mode  $\ell = 30$  [shown in Fig. 102.35(b)], the negative spikes for  $t < 1.4$  ns correspond to repeated shock interactions with the interface. Significant growth of the interface occurs after the acceleration phase and during the coasting phase due to Bell-Plesset<sup>21</sup> growth. This persists until the shock reflects from center and returns to the shell ( $\sim 1.75$  ns). This impulsive deceleration is followed by a period of continuous deceleration, when the fuel-shell interface is RT unstable due to pressure buildup in the gas. The RT-unstable interface distorts with bubbles of the lower-density fuel rising into the high-density plastic and spikes of the high-density CH falling into the lower-density fuel. Most observables for diagnosing implosion dynamics occur during this final phase of the implosion. Comparison of simulation to observations, therefore, provides an extremely stringent test of modeling perturbation growth and multidimensional fluid flow.

### Nonuniformity Seeding

The nonuniformity sources seeding the instabilities at the ablation surface and the fuel-shell interface can be divided into three wavelength ranges for the analysis of these implosions. Long-wavelength modulations ( $\ell \leq 10$ ) result in an overall deformation of the shell, whereas the intermediate ( $10 < \ell \leq 50$ ) and short wavelengths ( $\ell > 50$ ) result in a mass-modulated shell that can show considerable distortions including shell breakup. The time evolution of the long-wavelength nonuniformity sources due to imbalances between the OMEGA beams is modeled by overlapping the 60 beams on a sphere.<sup>5</sup> Beam mispointing ( $\sim 23\text{-}\mu\text{m}$  rms<sup>22</sup>), beam mistiming ( $\sim 12$ -ps rms is used in the calculation although  $\sim 9$ -ps rms<sup>23</sup> is more typical of OMEGA), energy imbalance ( $\sim 2.6\%$ <sup>22</sup>), and differences in the phase plates including azimuthal asymmetries are taken into account. These numbers are averaged over several

shots. The overlap is decomposed into spherical harmonics, and the amplitude of the corresponding Legendre mode is obtained by adding all the  $m$ -mode amplitudes in quadrature. The phase of the mode is chosen to be that of the  $m=0$  spherical harmonic. These time-dependent amplitudes are used as the laser modulation input to the 2-D axisymmetric hydrodynamic code *DRACO*.

The amplitudes of the dominant modes at the ablation surface (defined as the outer  $1/e$  point of maximum density) at the start of the acceleration phase are shown in Fig. 102.36(a). These amplitudes are seeds for RT growth during the acceleration phase. Also shown in Fig. 102.36(a) are the amplitudes due to target surface roughness<sup>24</sup> at the same time in the simulation. Figure 102.36(a) indicates that power imbalance is the larger of the two contributors to low-order nonuniformity.

Intermediate and shorter wavelengths are dominated by single-beam nonuniformity (through laser imprint<sup>25</sup>). An analytical model<sup>26</sup> describing the DPP's is used to modulate the laser illumination on target. In addition, polarization smoothing reduces the amplitudes by  $\sqrt{2}$  (Ref. 12), and smoothing by spectral dispersion<sup>11</sup> (1-THz, 2-D SSD with one color cycle) is also applied. These models are described in detail in Ref. 5. The resultant amplitudes at the ablation surface at the start of the acceleration phase are shown in Fig. 102.36(b). The ampli-

tudes decrease with increasing mode number. This is due to the earlier decoupling of the shorter wavelengths from the target and stabilization due to dynamic overpressure.<sup>25</sup>

**Effect of Shell Stability on Observables**

Figure 102.37 shows density contours from multimode simulations that include only the effect of single-beam nonuniformity ( $2 \leq \ell \leq 200$ ) for two CH-shell thicknesses [Fig. 102.37(a): 20  $\mu\text{m}$ ; Fig. 102.37(b): 27  $\mu\text{m}$ ]. These contours are shown at the end of the acceleration phase. The 20- $\mu\text{m}$ -thick shell, being less massive, has traveled a greater distance during acceleration and is considerably more distorted than the 27- $\mu\text{m}$ -thick CH shell. The peak-to-valley variation in the center-of-mass radius for the 20- $\mu\text{m}$ -thick shell is 6.6  $\mu\text{m}$  at the end of the acceleration phase, significantly greater than the calculated 1-D shell thickness (defined as the distance between the  $1/e$  points of maximum density in a spherically symmetric simulation) of  $\sim 5 \mu\text{m}$ , indicating shell breakup. The high-density regions are considerably distorted with portions of the shell at less than solid density. Therefore, short wavelengths play an important role in increasing the adiabat of the shell by introducing additional degrees of freedom for the fluid flow. This influences the compressibility of the shell and, therefore, quantities such as neutron yields and areal densities. In comparison, the 27- $\mu\text{m}$ -thick implosion has an integral shell at the end of the acceleration phase with a

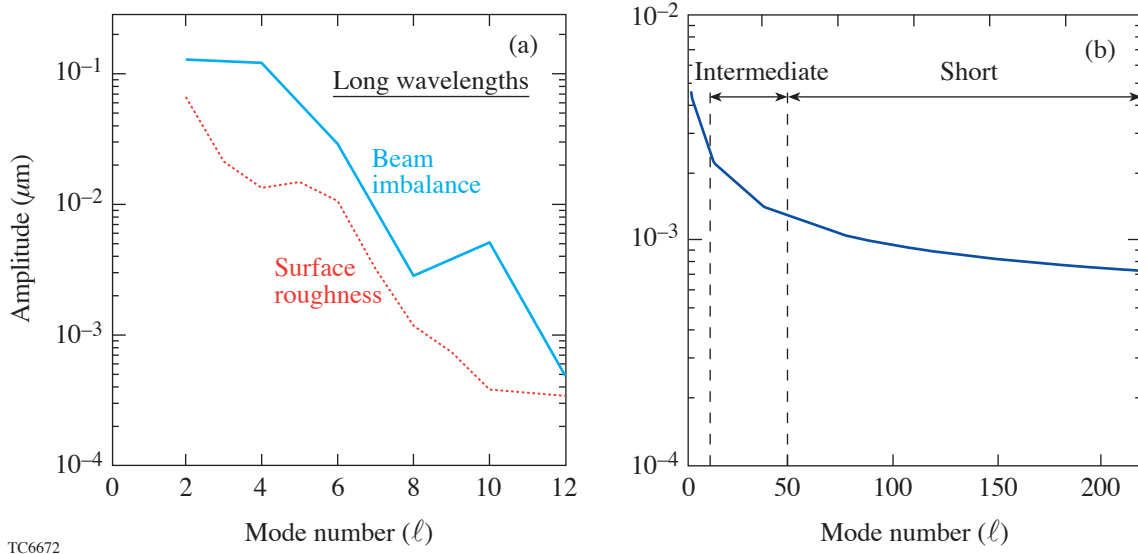


Figure 102.36 (a) Long-wavelength perturbations at the ablation surface due to beam imbalance (solid line) and surface roughness (dotted line) at the start of acceleration. Beam imbalance provides the larger contribution to long-wavelength nonuniformity seeds. (b) Imprint spectrum from single-mode simulations. Note that imprint efficiency decreases with increasing mode number.

peak-to-valley amplitude of  $3.4 \mu\text{m}$  in the center-of-mass radius compared to a 1-D shell thickness of  $\sim 6.8 \mu\text{m}$ . To realistically model the effect of laser imprint, modes resolved up to  $\ell \sim 400$  are required in the simulation.<sup>5</sup> A reliable simulation of this type is numerically challenging. Instead, a stability postprocessor<sup>27</sup> to *LILAC* is used to confirm that the qualitative conclusions do not change, i.e., the integrity of the 20- $\mu\text{m}$ -thick CH shell is severely compromised, whereas the 27- $\mu\text{m}$ -thick CH shell is essentially intact when the full range of modes is included.

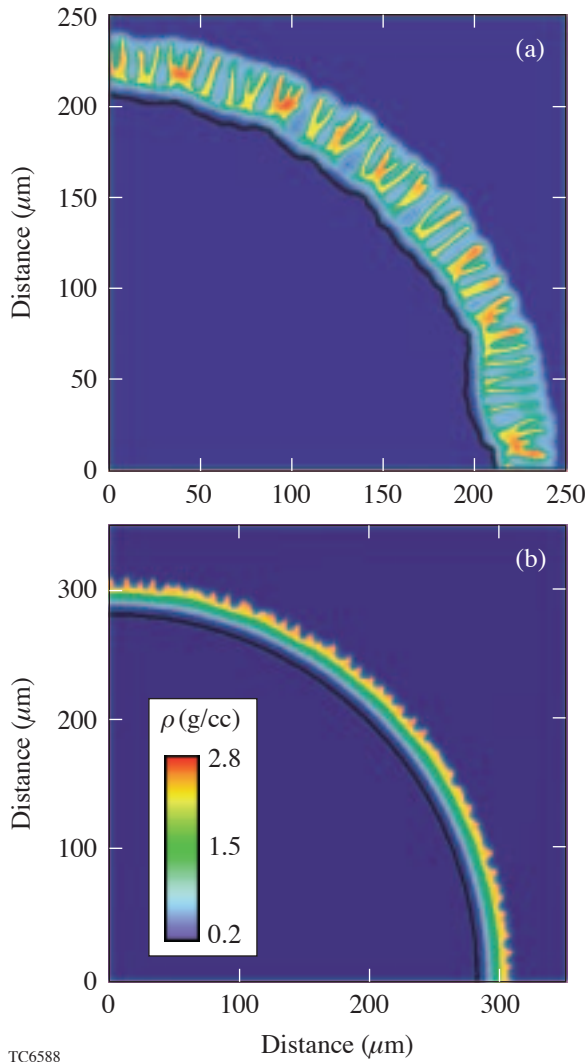


Figure 102.37 Density contours at the end of the acceleration phase for (a) a 20- $\mu\text{m}$ -thick CH shell and (b) a 27- $\mu\text{m}$ -thick CH shell from a multimode simulation of laser imprint. The solid lines correspond to the  $\text{D}_2$ -CH interface. Note that the shell (indicated by the higher-density contours) is significantly more distorted for the 20- $\mu\text{m}$  implosion than the 27- $\mu\text{m}$  implosion.

When the severely distorted 20- $\mu\text{m}$ -thick CH shell reassembles during the later stages of the implosion (around the time of the interaction of the reflected shock with the converging shell), the lower density due to shell breakup will result in a thicker shell than predicted with 1-D and a  $\rho R$  that is lower than 1-D predictions. The thicker shell will influence neutron production rates as follows: Between the time of peak neutron production and peak compression (shown schematically in Fig. 102.38), the neutron rate decreases due to the falling temperature in the gas because of heat conduction and radiative losses. The subsequent decrease in the neutron-production rate occurs due to shell disassembly. If the shell is thicker due to nonuniformity growth, disassembly occurs later in the implosion. The time between the interaction of the reflected shock (which is very similar for both integral and severely distorted shells) and the shock breakout of the shell is given by  $t_s = \Delta_{\text{sh}}/U_s$ , where  $\Delta_{\text{sh}}$  is the shell thickness and  $U_s$  is the shock speed. From Ref. 5,  $U_s = \sqrt{E_{\text{kin}}/R_{\text{hs}}^2 \Delta_{\text{sh}} \rho_{\text{sh}}}$ , where  $E_{\text{kin}}$  is the shell kinetic energy,  $R_{\text{hs}}$  is the radius of the hot spot, and  $\rho_{\text{sh}}$  is the shell density. Since  $E_{\text{kin}}$  is similar between the integral shell and the severely distorted shell implosion (only a small portion of the total energy goes into lateral flow in the

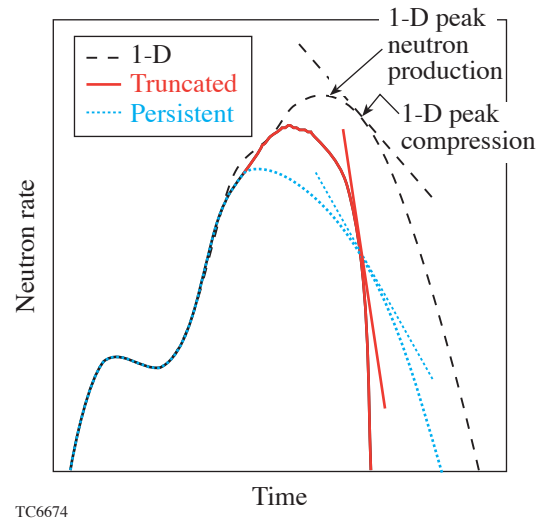


Figure 102.38 Schematics of a persistent neutron-production history and a truncated neutron-production history. In persistent neutron-production histories, burn follows 1-D (dashed) and then turns over (dotted). The rate of falloff near the peak is slower than in 1-D, as indicated by the lines drawn as tangents at peak compression. In truncated neutron-production histories, burn follows 1-D and then turns over rapidly near the peak with a distinct increase in the rate of falloff relative to 1-D (solid). The tangent line drawn at peak compression has a steeper slope compared to 1-D.

distorted shell implosion) and mass ( $\propto R_{\text{hs}}^2 \Delta_{\text{sh}} \rho_{\text{sh}}$ ) is conserved, the shock velocity is similar in both cases; therefore,  $t_s \propto \Delta_{\text{sh}}$  and is longer for the severely distorted shell, and disassembly is delayed. Consequently, neutron production falls less steeply than 1-D (Fig. 102.38, dashed line) in the implosion where shell stability is compromised (Fig. 102.38, dotted line). This is indicated in Fig. 102.38 by the decreased slope of the tangent line drawn at peak compression. For stable shells (27  $\mu\text{m}$ ), the shell thickness during neutron production is comparable to the 1-D thickness. In this case, the neutron-production rate will truncate (Fig. 102.38, solid line) primarily due to the RT-instability-induced mass flow into the colder bubbles near the fuel-shell interface.<sup>5</sup> This is indicated by the increased slope of the tangent line drawn at peak compression.

### Comparison of Simulations with Observables

The effect of the entire range of nonuniformities is modeled with two-mode simulations with mode numbers 4 and 20 used to represent the effect of long and intermediate wavelengths and three-mode simulations with modes 4, 20, and 200 used to represent all mode ranges. These simulations are performed on a 45° wedge. The initial amplitude for each mode is chosen from the amplitudes added in quadrature of a range of mode numbers (from the DPP and PS spectrum for  $\ell = 20$  using modes between 15 and 40 as the mode range and using modes between 100 and 300 as the mode range for  $\ell = 200$ , and from the initial power balance and surface-roughness data for modes  $2 < \ell \leq 10$  for mode  $\ell = 4$ ). SSD is applied to  $\ell = 200$  by reducing its initial amplitude by a factor  $\sqrt{(t_c/t_D)}$ , where  $t_c$  is the coherence time of mode 200 ( $\sim 2$  ps) and  $t_D$  is the decoupling time for this mode ( $\sim 16$  ps for the 1-ns square

pulse). This reduction factor is in agreement with measurements.<sup>28</sup> Density contours at peak neutron production in 2-D are shown for the two thicknesses in Fig. 102.39. The 2-D fuel-shell interface (solid black line) in both cases is significantly distorted compared to 1-D (dashed line). The peak density in the thinner shell is  $\sim 70\%$  of the 1-D peak density compared to nearly 100% for the thick shell. This undercompression is due to shell breakup during the acceleration phase, as discussed in the previous section.

Neutron-production rates from these simulations are compared against 1-D rates (solid line) in Fig. 102.40 [Fig. 102.40(a): 20- $\mu\text{m}$ -thick CH shell; Fig. 102.40(b): 27- $\mu\text{m}$ -thick CH shell]. With low and intermediate modes alone (dashed line), burn truncation is evident for both shell thicknesses. In this case, the in-flight shell thickness is the same as the 1-D shell thickness. The addition of the short wavelength (dotted line) significantly influences the neutron-production rate for the 20- $\mu\text{m}$  shell; the burn rate deviates from 1-D with a more gradual falloff. The short wavelength has only a marginal effect on the thicker shell. Similar trends are observed in experiments. The 1-D calculated and measured neutron-production rates are shown in Fig. 102.41 for three shell thicknesses. The 1-D neutron rates are temporally shifted to align the rise of neutron production with the rise of the measured rate curves. The required time shifts are within the uncertainties in absolute timing in the experiment. Burn truncation is evident for the thick shell case [Fig. 102.41(c)]; the tangent line has a steeper slope compared to 1-D, whereas, with decreasing shell thickness, neutron-production falls off less rapidly near the peak. Measurement and 1-D simulations from a 15- $\mu\text{m}$ -thick CH implosion are

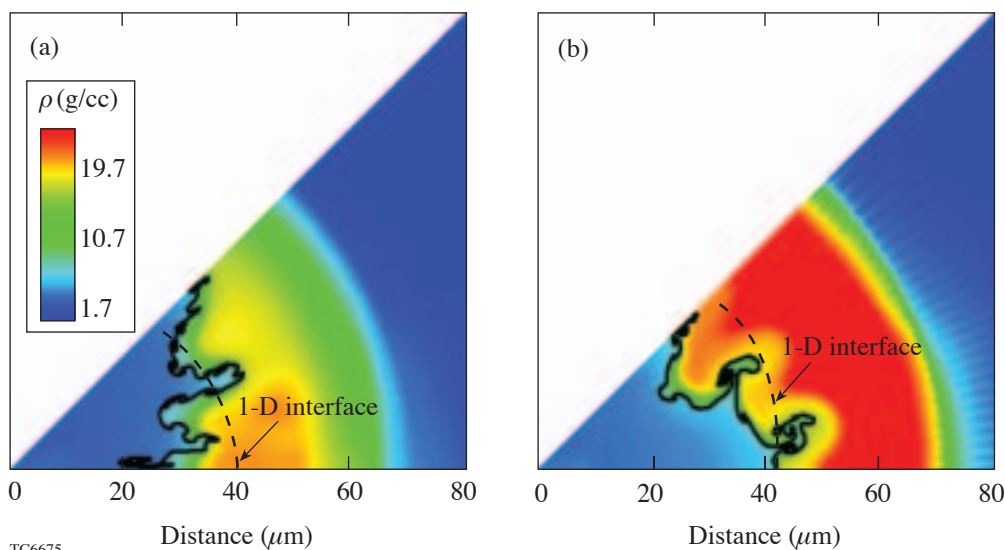


Figure 102.39  
Density contours for simulations including the effect of all mode ranges at peak neutron production for (a) the 20- $\mu\text{m}$ -thick CH shell and (b) the 27- $\mu\text{m}$ -thick CH shell. The solid line is the fuel-shell interface. The peak density in (a) is  $\sim 70\%$  of the 1-D peak density, whereas in (b) it is  $\sim 100\%$  of 1-D peak density. This undercompression in the 20- $\mu\text{m}$ -thick shell occurs due to shell instability during acceleration.

compared in Fig. 102.41(a). This shell should be even more compromised in its integrity than the 20- $\mu\text{m}$ -thick CH shell. The measured rates show the expected trend: a more gradual falloff near the peak.

Simulated neutron-production rates for the 20- $\mu\text{m}$ -thick CH shell with a 3-atm fill are shown in Fig. 102.42(a). Even though the shell is severely compromised during acceleration, burn truncation is evident in this case. Nonuniformity growth

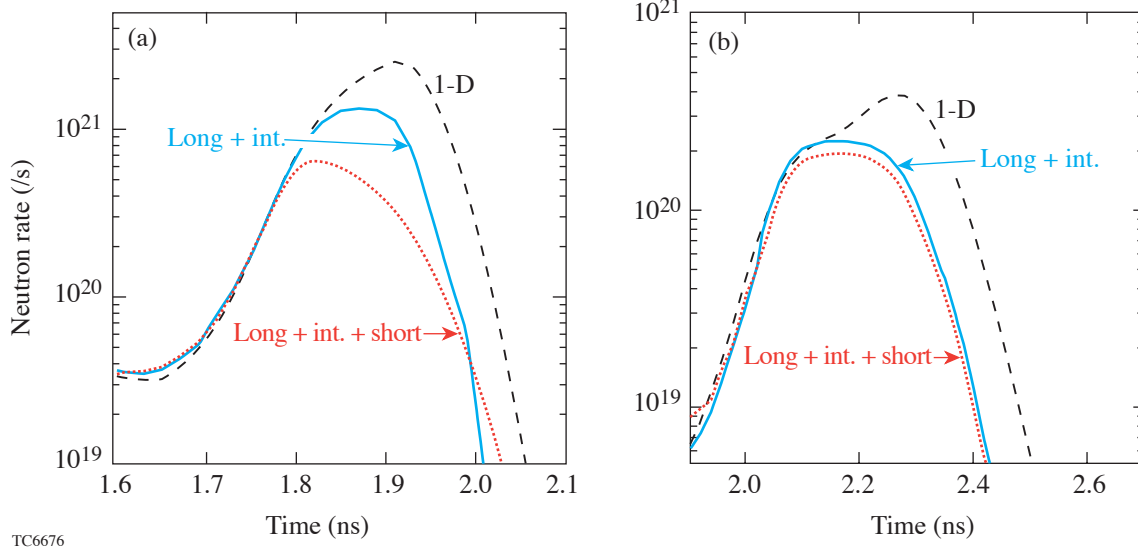


Figure 102.40 Neutron-production rates from the simulation including only low- and intermediate-mode numbers (dotted line) and the simulation including short wavelengths (solid line) compared to 1-D (dashed line) for (a) the 20- $\mu\text{m}$ -thick CH shell and (b) the 27- $\mu\text{m}$ -thick CH shell. Note that the inclusion of the shorter wavelengths in the simulation results in a less-steep fall of the neutron-production rate for the 20- $\mu\text{m}$  implosion and retains burn truncation for the 27- $\mu\text{m}$  case.

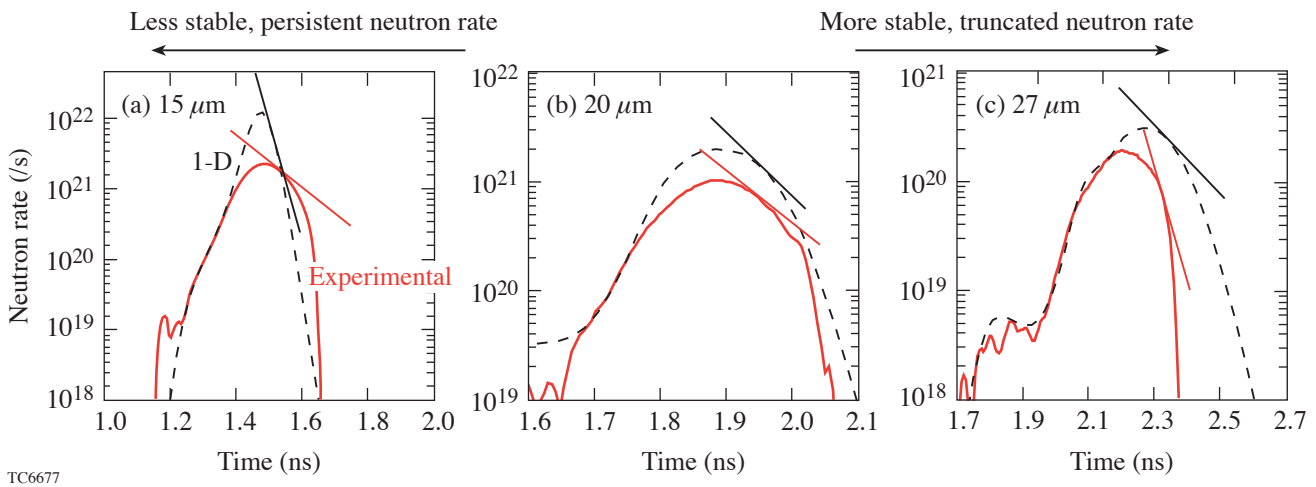


Figure 102.41 Comparison of calculated (1-D) neutron rates (dashed) with experiment (solid line) for (a) the 15- $\mu\text{m}$ -thick implosion (shot 36100), (b) the 20- $\mu\text{m}$ -thick implosion (shot 30628), and (c) the 27- $\mu\text{m}$ -thick implosion (shot 22088). All implosions have a 15-atm fill. Burn truncation is evident for the 27- $\mu\text{m}$ -thick implosion. The neutron-production rate persists and is almost as wide as 1-D for the 20- $\mu\text{m}$ -thick implosion and wider than 1-D for the 15- $\mu\text{m}$ -thick implosion.

at the interface compromises the core; at peak neutron production in 1-D (~1.85 ns), there is no clean core evident in the 2-D simulations, reducing the neutron rate significantly and resulting in truncation. Consistent with this simulation, burn truncation is evident in the measured neutron-production rates [Fig. 102.42(b)] when overlaid onto the 1-D simulation results.

Two-dimensional simulated primary neutron yields compare very favorably with measured values. Figure 102.43 shows the experimental yield<sup>4</sup> normalized to the correspond-

ing 1-D yields (open circles) for the four target configurations: 20- $\mu\text{m}$ -thick, 15-atm-fill; 20- $\mu\text{m}$ -thick, 3-atm-fill; 27- $\mu\text{m}$ -thick, 15-atm-fill; and 27- $\mu\text{m}$ -thick, 3-atm-fill. Each point is this quantity averaged over many OMEGA shots. The error bars are the one-standard-deviation variation over these shots. All simulated values (solid symbols) compare well with observations.

Simulated neutron-averaged shell areal densities normalized to the 1-D values (solid) are shown in Fig. 102.44, comparing favorably with the experimentally inferred val-

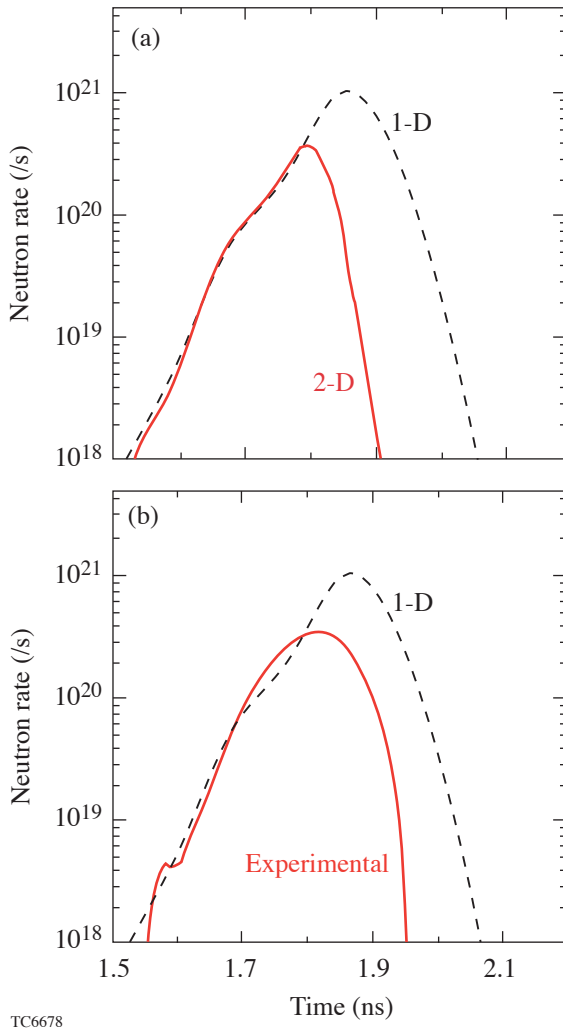


Figure 102.42 (a) Simulated neutron-production rates for the 20- $\mu\text{m}$ -thick, 3-atm-fill implosion: 2-D (solid) and 1-D (dashed). Burn truncation is evident even though the shell is significantly distorted during acceleration because of the absence of a “clean” core early during deceleration. (b) Comparison of the 1-D simulation with measured neutron-production rate (shot 22864). The same trend of burn truncation is observed in experiment.

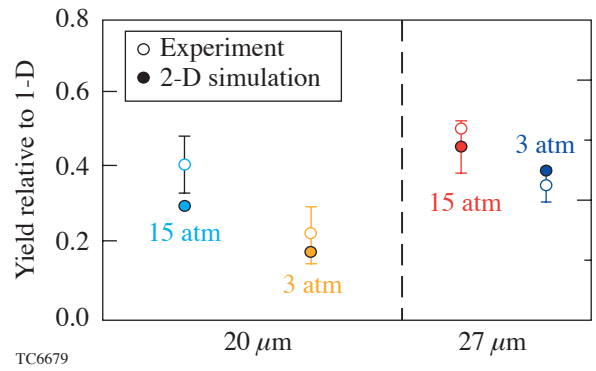


Figure 102.43 Yields relative to 1-D for four cases: 20- $\mu\text{m}$ -thick, 15-atm-fill; 20- $\mu\text{m}$ -thick, 3-atm-fill; 27- $\mu\text{m}$ -thick, 15-atm-fill; and 27- $\mu\text{m}$ -thick, 3-atm-fill (measured: open circles; 2-D: closed circles). Good agreement is obtained between experiment and simulation.

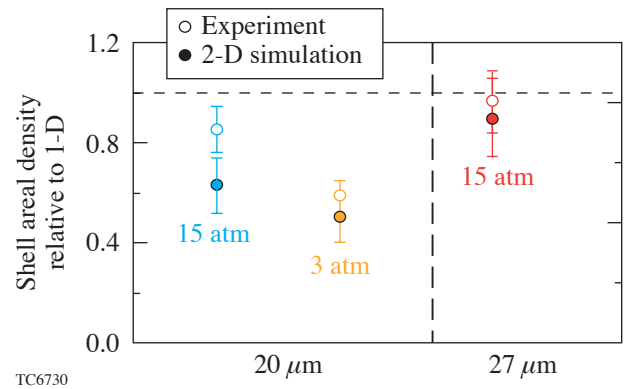


Figure 102.44 Neutron-averaged shell areal density relative to 1-D for the same four targets as in Fig. 102.43. Simulations are shown as the solid symbols. The “error bar” in the 2-D results is the one standard deviation in the variation in the polar angle areal density.

ues<sup>15</sup> (open). The error bars associated with the simulation points are the one-standard-deviation polar-angle variation in the areal density. There is no data for the 27- $\mu\text{m}$ -thick, 3-atm-fill implosion.

Experimental neutron-averaged ion temperatures<sup>4</sup> inferred from neutron time of flight are shown in Fig. 102.45 (open circles). Experimentally inferred ion temperatures are systematically higher than those simulated (solid). Reasons for this systematic deviation are being investigated currently. Ion temperatures from the measured DD neutron to D<sup>3</sup>He proton yield ratios<sup>15</sup> are also shown in Fig. 102.45 (open squares) for the cases where data are available. This temperature shows better agreement with simulation results.

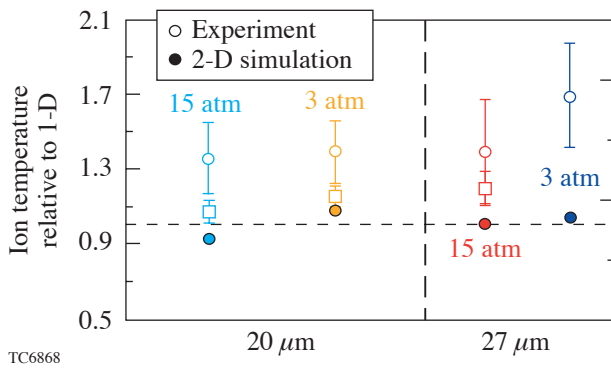


Figure 102.45

Neutron-averaged ion temperatures relative to 1-D for the four target configurations as in Fig. 102.43. Inferred ion temperatures from neutron time-of-flight (open circles) are systematically higher than simulated ion temperatures (solid circles). The ion temperatures inferred from the DD neutron to D<sup>3</sup>He proton yield ratios (open squares) are also shown.

The significant influence of low and intermediate wavelengths on thick shells is consistent with observations of neutron yields using the newer SG4 phase plates<sup>14</sup> on the OMEGA laser beams. The improvement in the on-target laser nonuniformity between the SG3 and the SG4 phase plates has been modeled to be primarily in the low- and intermediate-mode ranges [Fig. 102.46(a)].<sup>14</sup> The ratio of the calculated rms nonuniformity with the SG3 phase plates relative to the SG4 phase plates is shown in Fig. 102.46(a). In Fig. 102.46(b), the measured yield relative to 1-D is shown for both shell thicknesses. Significant improvement in the 27- $\mu\text{m}$ -thick shell's performance is measured [Fig. 102.46(b)].

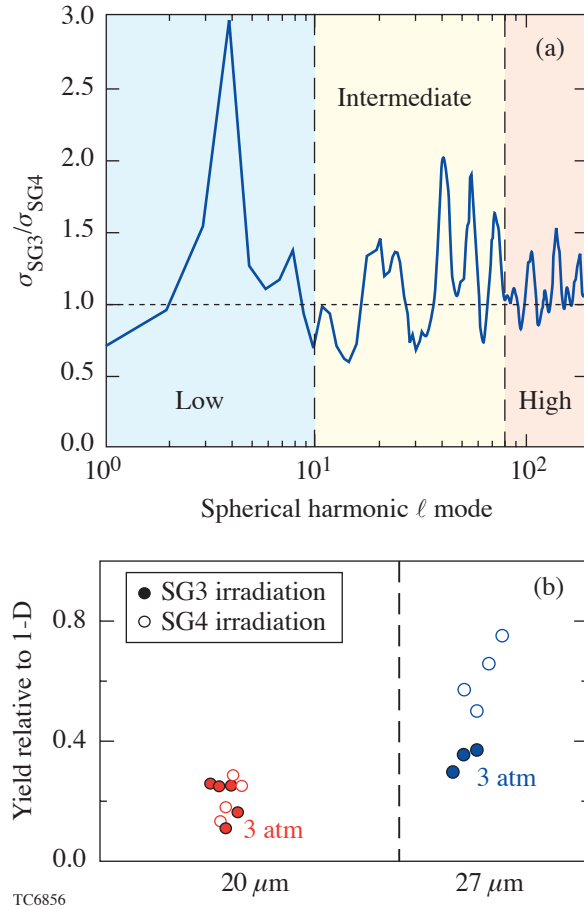


Figure 102.46

(a) Ratio of the modeled on-target laser nonuniformity due to the SG3 and SG4 phase plates (see text). Significant improvements in the uniformity of low and intermediate wavelengths have been modeled, whereas marginal improvements in the uniformity of short wavelengths are calculated. (b) Measured yields relative to 1-D for the SG3 phase plates (solid) and the SG4 phase plates (open) for 20- $\mu\text{m}$ -thick and 27- $\mu\text{m}$ -thick CH shells with 3-atm fills. Significant improvement is observed in target performance for the thicker shells unlike the thin shells. Thin-shell performance is dominated by the seeding of short-wavelength modes, which has marginally changed in the transition from SG3 to SG4 phase plates.

Lineouts from  $\sim 4.5$ -keV gated x-ray pinhole camera images of the core self-emission for the 20- $\mu\text{m}$ -thick CH shell are shown in Fig. 102.47. The results of Spect3D<sup>29</sup> post-processing of 2-D simulations (solid) with the 1-D results (dashed) are shown at peak neutron production [Fig. 102.47(a)] and at peak compression [Fig. 102.47(b)]. Each curve is normalized to the corresponding peak intensity. The postprocessed 1-D simulation shows a distinct limb corresponding to the fuel-shell interface position. The 2-D simulated emission in Figs. 102.47(a) and 102.47(b) is the polar angle average of the

emission from the target. The averaging process smears out the limb due to the nonuniformity of the fuel–shell interface. Further, peak simulated emission in 2-D occurs from the hot CH spikes, which are at a smaller radius than the 1-D fuel–shell interface (Fig. 102.39). As a result, the brightness profile in 2-D decreases rapidly at a smaller radius than in the 1-D emission profile. The more distorted shell also results in a more gradual decrease in the brightness compared to the 1-D profile. Comparisons of the measured azimuthally averaged curves<sup>18</sup> normalized to peak intensity and the corresponding 1-D simulations are shown at peak neutron production [Fig. 102.47(c)] and at peak compression [Fig. 102.47(d)]. Similar trends are observed in experiments; the limb is no longer evident, the decrease in brightness occurs at a smaller radius than in 1-D, and this decrease is more gradual than in the 1-D profile.

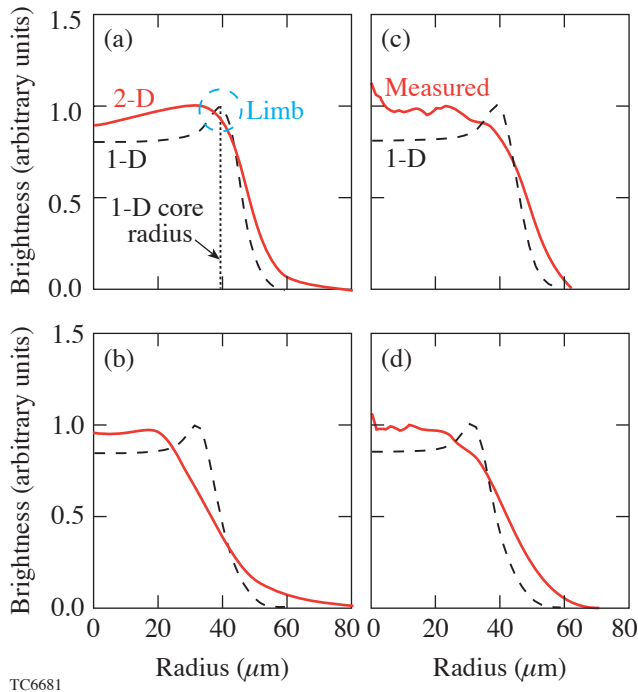


Figure 102.47

Brightness profile at  $\sim 4.5$  keV of the core normalized to peak intensity for the  $20\text{-}\mu\text{m}$ -thick CH shell. (a) Comparison of 1-D profiles (dashed) with the polar-averaged 2-D profile (solid) at peak neutron production. 1-D simulation indicates a prominent limb due to the fuel–shell interface. 2-D simulation indicates a smeared-out limb. (b) Same as (a) but at peak compression. (c) Azimuthally averaged brightness profile from measured pinhole camera images (shot 22546) at peak neutron production (solid line) compared to 1-D (dashed line). (d) Same as (c) but at peak compression. Good agreement is obtained between the 2-D profiles and the measured profiles including the absence of a significant limb and more gradual decrease in brightness relative to the 1-D profile.

In previous work, homogenous mixing of  $\text{D}_2$  and  $\text{CH}^{30-33}$  has been inferred from experimental observables such as secondary neutron ratios,<sup>30,31</sup> argon spectral lines,<sup>32</sup> and  $\text{D}^3\text{He}$  yields in  $^3\text{He}$ -filled CD shells.<sup>30,31</sup> These observables preferentially sample the turbulently mixed region of the target and are sensitive to mix. The primary neutron yields were not directly used to determine the presence of turbulence. These neutrons are produced in the bulk of the fuel; the reduced values of the primary yields relative to 1-D are instead due to the effects discussed in **Effect of Shell Stability on Observables** (p. 95).

An order-of-magnitude estimate of the small-scale mixing length can be obtained as follows: The turbulent mixing layer grows self-similarly with a mixing thickness  $h$ , given by Ref. 34,

$$h = \alpha A_T g t^2, \quad (1)$$

where  $\alpha$  is a dimensionless constant. Taking  $A_T = 0.18$  for the  $\text{D}_2$ –CH interface gives  $\alpha = 0.05$  (Ref. 34). The expression in Ref. 34 is for planar turbulent growth due to the presence of many modes. In the cases considered in this article, convergence effects play an important role. In addition, the return shock recompresses the mixing layer. Subsequent reshocking of the mixing layer can occur in implosions; therefore, this estimate of mixing lengths should be considered as an order-of-magnitude estimate. A hydrodynamics code, such as *DRACO*, cannot follow materials into the turbulent regime. Using  $\alpha = 0.05$  leads to  $h = 0.9\ \mu\text{m}$ ; therefore, if the simulated short-wavelength amplitude is considered to be a mix thickness, the value of  $\sim 1\ \mu\text{m}$  (Fig. 102.39) compares favorably with the estimated mix thickness. Larger mixing widths ( $\sim 17\ \mu\text{m}$ ) have been inferred based on spherically symmetric 1-D mix models.<sup>30,31</sup> Since 1-D mix models do not account for the increased volume due to long-wavelength distortions, it is very likely that they overestimate the mixing length.

## Conclusions

Two-dimensional simulations of imploding plastic shells are presented using the radiation hydrodynamic code *DRACO*. Shell instability through the growth of short-wavelength perturbations plays an important role in determining target performance for “thin” ( $\leq 20\text{-}\mu\text{m}$ -thick) CH shells. Target performance is dominated by long and intermediate wavelengths for thicker shells. Observables such as primary neutron yields, areal densities, temporal histories of neutron production, and x-ray images of self-emission compare very well with experimental

measurements. Neutron-averaged ion temperatures inferred from neutron time of flight are significantly higher than the calculated values. The reasons for this systematic discrepancy are under investigation. Calculated ion temperatures, however, are more consistent with values inferred from the ratios of DD neutron to D<sup>3</sup>He proton yield. The good agreement with experiment for most observables indicates that the modeling of nonuniformity seeds for instability growth and multidimensional implosion dynamics due to realistic laser and target asymmetries describe realistic direct-drive inertial confinement fusion implosions reasonably well.

#### ACKNOWLEDGMENT

This work was supported by the U.S. Department of Energy Office of Inertial Confinement Fusion under Cooperative Agreement No. DE-FC52-92SF19460, the University of Rochester, and the New York State Energy Research and Development Authority. The support of DOE does not constitute an endorsement by DOE of the views expressed in this article.

#### REFERENCES

1. J. Nuckolls *et al.*, *Nature* **239**, 139 (1972).
2. Lord Rayleigh, *Proc. London Math Soc.* **XIV**, 170 (1883); G. Taylor, *Proc. R. Soc. London Ser. A* **201**, 192 (1950).
3. C. P. Verdon, *Bull. Am. Phys. Soc.* **38**, 2010 (1993); P. W. McKenty, V. N. Goncharov, R. P. J. Town, S. Skupsky, R. Betti, and R. L. McCrory, *Phys. Plasmas* **8**, 2315 (2001).
4. D. D. Meyerhofer, J. A. Delettrez, R. Epstein, V. Yu. Glebov, V. N. Goncharov, R. L. Keck, R. L. McCrory, P. W. McKenty, F. J. Marshall, P. B. Radha, S. P. Regan, S. Roberts, W. Seka, S. Skupsky, V. A. Smalyuk, C. Sorce, C. Stoeckl, J. M. Soures, R. P. J. Town, B. Yaakobi, J. D. Zuegel, J. Frenje, C. K. Li, R. D. Petrasso, D. G. Hicks, F. H. Séguin, K. Fletcher, S. Padalino, M. R. Freeman, N. Izumi, R. Lerche, T. W. Phillips, and T. C. Sangster, *Phys. Plasmas* **8**, 2251 (2001).
5. P. B. Radha, V. N. Goncharov, T. J. B. Collins, J. A. Delettrez, Y. Elbaz, V. Yu. Glebov, R. L. Keck, D. E. Keller, J. P. Knauer, J. A. Marozas, F. J. Marshall, P. W. McKenty, D. D. Meyerhofer, S. P. Regan, T. C. Sangster, D. Shvarts, S. Skupsky, Y. Srebro, R. P. J. Town, and C. Stoeckl, *Phys. Plasmas* **12**, 032702 (2005).
6. T. R. Boehly, D. L. Brown, R. S. Craxton, R. L. Keck, J. P. Knauer, J. H. Kelly, T. J. Kessler, S. A. Kumpan, S. J. Loucks, S. A. Letzring, F. J. Marshall, R. L. McCrory, S. F. B. Morse, W. Seka, J. M. Soures, and C. P. Verdon, *Opt. Commun.* **133**, 495 (1997).
7. J. D. Lindl, *Phys. Plasmas* **2**, 3933 (1995).
8. V. Lobatchev and R. Betti, *Phys. Rev. Lett.* **85**, 4522 (2000).
9. E. M. Campbell and W. J. Hogan, *Plasma Phys. Control. Fusion* **41**, B39 (1999).
10. W. R. Donaldson, R. Boni, R. L. Keck, and P. A. Jaanimagi, *Rev. Sci. Instrum.* **73**, 2606 (2002).
11. S. Skupsky, R. W. Short, T. Kessler, R. S. Craxton, S. Letzring, and J. M. Soures, *J. Appl. Phys.* **66**, 3456 (1989).
12. T. R. Boehly, V. A. Smalyuk, D. D. Meyerhofer, J. P. Knauer, D. K. Bradley, R. S. Craxton, M. J. Guardalben, S. Skupsky, and T. J. Kessler, *J. Appl. Phys.* **85**, 3444 (1999).
13. C. B. Burckhardt, *Appl. Opt.* **9**, 695 (1970); Y. Kato *et al.*, *Phys. Rev. Lett.* **53**, 1057 (1984); Laboratory for Laser Energetics LLE Review **65**, 1, NTIS document No. DOE/SF/19460-117 (1995). Copies may be obtained from the National Technical Information Service, Springfield, VA 22161.
14. S. P. Regan, J. A. Delettrez, V. Yu. Glebov, V. N. Goncharov, J. A. Marozas, F. J. Marshall, P. W. McKenty, D. D. Meyerhofer, P. B. Radha, T. C. Sangster, V. A. Smalyuk, C. Stoeckl, J. A. Frenje, C. K. Li, R. D. Petrasso, and F. H. Séguin, *Bull. Am. Phys. Soc.* **49**, 62 (2004).
15. C. K. Li, D. G. Hicks, F. H. Séguin, J. A. Frenje, R. D. Petrasso, J. M. Soures, P. B. Radha, V. Yu. Glebov, C. Stoeckl, D. R. Harding, J. P. Knauer, R. L. Kremens, F. J. Marshall, D. D. Meyerhofer, S. Skupsky, S. Roberts, C. Sorce, T. C. Sangster, T. W. Phillips, M. D. Cable, and R. J. Leeper, *Phys. Plasmas* **7**, 2578 (2000).
16. C. K. Li, F. H. Séguin, D. G. Hicks, J. A. Frenje, K. M. Green, S. Kurebayashi, R. D. Petrasso, D. D. Meyerhofer, J. M. Soures, V. Yu. Glebov, R. L. Keck, P. B. Radha, S. Roberts, W. Seka, S. Skupsky, C. Stoeckl, and T. C. Sangster, *Phys. Plasmas* **8**, 4902 (2001).
17. R. A. Lerche, D. W. Phillion, and G. L. Tietbohl, *Rev. Sci. Instrum.* **66**, 933 (1995).
18. S. P. Regan, J. A. Delettrez, R. Epstein, P. A. Jaanimagi, B. Yaakobi, V. A. Smalyuk, F. J. Marshall, D. D. Meyerhofer, W. Seka, D. A. Haynes, Jr., I. E. Golovkin, and C. F. Hooper, Jr., *Phys. Plasmas* **9**, 1357 (2002).
19. M. C. Richardson, G. G. Gregory, R. L. Keck, S. A. Letzring, R. S. Marjoribanks, F. J. Marshall, G. Pien, J. S. Wark, B. Yaakobi, P. D. Goldstone, A. Hauer, G. S. Stradling, F. Ameduri, B. L. Henke, and P. Jaanimagi, in *Laser Interaction and Related Plasma Phenomena*, edited by H. Hora and G. H. Miley (Plenum Press, New York, 1986), Vol. 7, pp. 179–211.
20. S. E. Bodner, *Phys. Rev. Lett.* **33**, 761 (1974); H. Takabe *et al.*, *Phys. Fluids* **28**, 3676 (1985); R. Betti, V. N. Goncharov, R. L. McCrory, P. Sorotokin, and C. P. Verdon, *Phys. Plasmas* **3**, 2122 (1996).
21. G. I. Bell, Los Alamos National Laboratory, Los Alamos, NM, Report LA-1321 (1951); M. S. Plesset, *J. Appl. Phys.* **25**, 96 (1954); D. L. Book and S. E. Bodner, *Phys. Fluids* **30**, 367 (1987); Laboratory for Laser Energetics LLE Review **94**, 81, NTIS document No. DOE/SF/19460-485 (2003). Copies of LLE Review **94** may be obtained from the National Technical Information Service, Springfield, VA 22161.
22. F. J. Marshall, J. A. Delettrez, R. Epstein, R. Forties, R. L. Keck, J. H. Kelly, P. W. McKenty, S. P. Regan, and L. J. Waxer, *Phys. Plasmas* **11**, 251 (2004).
23. K. A. Thorp, Laboratory for Laser Energetics, private communication (2004).

24. R. C. Cook, R. L. McEachern, and R. B. Stephens, *Fusion Technol.* **35**, 224 (1999).
25. V. N. Goncharov, S. Skupsky, T. R. Boehly, J. P. Knauer, P. McKenty, V. A. Smalyuk, R. P. J. Town, O. V. Gotchev, R. Betti, and D. D. Meyerhofer, *Phys. Plasmas* **7**, 2062 (2000).
26. R. Epstein, *J. Appl. Phys.* **82**, 2123 (1997).
27. V. N. Goncharov, P. McKenty, S. Skupsky, R. Betti, R. L. McCrory, and C. Cherfils-Clérouin, *Phys. Plasmas* **7**, 5118 (2000).
28. T. R. Boehly, V. N. Goncharov, O. Gotchev, J. P. Knauer, D. D. Meyerhofer, D. Oron, S. P. Regan, Y. Srebro, W. Seka, D. Shvarts, S. Skupsky, and V. A. Smalyuk, *Phys. Plasmas* **8**, 2331 (2001).
29. J. J. MacFarlane *et al.*, in *Inertial Fusion Sciences and Applications 2003*, edited by B. A. Hammel *et al.* (American Nuclear Society, La Grange Park, IL, 2004), pp. 457–460; Prism Computational Sciences, Inc., Madison, WI, 53711.
30. C. K. Li, F. H. Séguin, J. A. Frenje, S. Kurebayashi, R. D. Petrasso, D. D. Meyerhofer, J. M. Soures, J. A. Delettrez, V. Yu. Glebov, P. B. Radha, F. J. Marshall, S. P. Regan, S. Roberts, T. C. Sangster, and C. Stoeckl, *Phys. Rev. Lett.* **89**, 165002 (2002).
31. P. B. Radha, J. Delettrez, R. Epstein, V. Yu. Glebov, R. Keck, R. L. McCrory, P. McKenty, D. D. Meyerhofer, F. Marshall, S. P. Regan, S. Roberts, T. C. Sangster, W. Seka, S. Skupsky, V. Smalyuk, C. Sorce, C. Stoeckl, J. Soures, R. P. J. Town, B. Yaakobi, J. Frenje, C. K. Li, R. Petrasso, F. Séguin, K. Fletcher, S. Padalino, C. Freeman, N. Izumi, R. Lerche, and T. W. Phillips, *Phys. Plasmas* **9**, 2208 (2002).
32. S. P. Regan, J. A. Delettrez, V. N. Goncharov, F. J. Marshall, J. M. Soures, V. A. Smalyuk, P. B. Radha, B. Yaakobi, R. Epstein, V. Yu. Glebov, P. A. Jaanimagi, D. D. Meyerhofer, T. C. Sangster, W. Seka, S. Skupsky, C. Stoeckl, D. A. Haynes, Jr., J. A. Frenje, C. K. Li, R. D. Petrasso, and F. H. Séguin, *Phys. Rev. Lett.* **92**, 185002 (2004).
33. D. C. Wilson, C. W. Cranfill, C. Christensen, R. A. Forster, R. R. Peterson, H. M. Hoffman, G. D. Pollak, C. K. Li, F. H. Séguin, J. A. Frenje, R. D. Petrasso, P. W. McKenty, F. J. Marshall, V. Yu. Glebov, C. Stoeckl, G. J. Schmid, N. Izumi, and P. Amendt, *Phys. Plasmas* **11**, 2723 (2004).
34. G. Dimonte, *Phys. Plasmas* **6**, 2009 (1999).

---

# Effects of Temporal Density Variation and Convergent Geometry on Nonlinear Bubble Evolution in Classical Rayleigh–Taylor Instability

## Introduction

Rayleigh–Taylor (RT) instability develops in a large variety of physical systems, including an imploding shell during inertial confinement fusion experiments<sup>1</sup> and a supernovae explosion in astrophysics.<sup>2</sup> RT instability occurs at the interface between two fluids subject to an acceleration field pointing from the heavier to the lighter fluid.<sup>3</sup> Analytical modeling of such an instability, as well as many other physical phenomena, is based mainly on perturbation methods. In such methods, the equations describing both the physical laws and unknown physical quantities are expanded in a series of small parameters. This allows an approximate solution to otherwise mathematically intractable problems to be obtained. When the amplitude of the interface distortion  $\eta$  between fluids is much smaller than the perturbation wavelength  $\lambda$  (linear perturbation analysis), the small parameter of the perturbation method is  $k\eta$ , where  $k = 2\pi/\lambda$  is the wave number. The hydrodynamic equations in this case can be linearized, yielding an exponential in time perturbation growth.<sup>3</sup> When the distortions are amplified by RT instability to amplitudes comparable to the wavelength, the perturbation series based on  $k\eta$  expansion becomes divergent and the expansion breaks down. At such amplitudes a different expansion parameter is needed. It was first proposed in Ref. 4 to use a spatial variable along the fluid interface as a small parameter. The perturbation series in this case gives an approximate analytic solution to the nonlinear problem. Such a solution, however, is valid only locally at the tip of the bubble of the lighter fluid raising into the heavier fluid. Layzer's model, despite its simplicity, has been shown to work remarkably well in describing the nonlinear bubble evolution in classical RT instability.<sup>5–9</sup> Recently<sup>9</sup> the model was extended to arbitrary Atwood numbers  $A_T = (\rho_h - \rho_l)/(\rho_h + \rho_l)$ , where  $\rho_h$  and  $\rho_l$  are the densities of heavier and lighter fluids, respectively. The convergence effects have been included in Ref. 10 for cylindrical geometry and in Ref. 11 for spherical geometry in the case of self-similar flow. In addition to the Layzer's theory, other models have been successfully used to study the nonlinear RT evolution (see, for example, Refs. 12 and 13). This article presents a general scaling of the bubble evolution with the flow

parameters in planar and spherical geometries for arbitrary temporal density variations and shell trajectories.

The following sections (1) discuss the effects of the temporal density variation on the bubble evolution in the planar geometry and (2) describe the model that predicts the nonlinear perturbation evolution in a spherical geometry.

## Planar Geometry: Time-Dependent Density

We consider a fluid with time-dependent uniform density  $\rho(t)$  supported in a gravitational field  $\mathbf{g}(t)$  by a lighter fluid with density  $\rho_l \ll \rho$ . The effects of the finite density of the lighter fluid will be neglected in the analysis ( $A_T = 1$ ). The gravity is pointing in the negative  $z$  direction. The heavier fluid occupies the upper half of the space with  $z > 0$ . We choose the unperturbed fluid interface to lie in the  $(x,y)$  plane. The regions of the distorted interface where the lighter fluid rises into the heavier fluid are referred to as bubbles; regions where the heavier fluid protrudes into the lighter fluid are referred to as spikes. The standard Layzer's approach<sup>4</sup> deals with the flow at the tip of the bubbles where the vortex motion developed at large perturbation amplitudes has a small effect. Next, introducing a velocity potential  $\mathbf{v} = \nabla\Phi$ , the mass conservation equation is reduced to Poisson's equation:

$$\nabla^2\Phi = \partial_x^2\Phi + \partial_y^2\Phi + \partial_z^2\Phi = -\frac{\dot{\rho}}{\rho}. \quad (1)$$

The right-hand side of Eq. (1), neglected in the original Layzer's work,<sup>4</sup> is due to the temporal variation in the fluid density. Such a term, however, was retained previously in the analysis of the linear perturbation evolution.<sup>14,15</sup> In the unperturbed case, Eq. (1) yields the velocity field with the uniform spatial gradient  $v_z = z\dot{\rho}/\rho$ . One must keep in mind that the Layzer's model deals with flow in the proximity of the fluid interface; therefore, the actual flow is not required to have a uniform velocity gradient throughout the whole region. When the fluid interface is distorted, the perturbations start to grow due to RT instability. To find the perturbation evolution, the

fluid equations and hydrodynamic functions are expanded in powers of  $\bar{x}$  near the tip of the bubble (we assume that the center of the bubble is localized at  $\bar{x}=0$ ). Here,  $\bar{x}=x$  in two-dimensional perturbed flow and  $\bar{x}=r=\sqrt{x^2+y^2}$  in three-dimensional flow. The expansion of the position of the distorted interface  $\eta(\bar{x},t)$  gives  $\eta(\bar{x},t)=\eta_0(t)+\eta_2(t)\bar{x}^2+\dots$ , where  $\eta_0>0$  is the bubble amplitude, and  $\eta_2$  is related to the bubble curvature  $R$  as  $\eta_2=-1/(2R)$ . The solution of Eq. (1) expanded up to  $\bar{x}^2$  takes the form

$$\Phi=\frac{a(t)}{k}\left(1-\tilde{c}_g\frac{k^2\bar{x}^2}{4}\right)e^{-k(z-\eta_0)}-\frac{\dot{\rho}}{2\rho}z^2, \quad (2)$$

where  $k$  is the perturbation wave number and  $\tilde{c}_g=2$  and  $\tilde{c}_g=1$  for two- and three-dimensional geometries, respectively. Note that the standard Layzer's model keeps only terms up to  $\bar{x}^2$  in the expansion of hydrodynamic functions. It is sufficient, therefore, to retain only the fundamental harmonic in solution (2) to satisfy such accuracy. For higher-accuracy models, the higher harmonics must be included in the velocity potential.<sup>9</sup> The potential  $\Phi$  is subject to the following jump conditions at the interface  $z=\eta(\bar{x},t)$ :

$$\partial_t\eta+v_{\bar{x}}\partial_{\bar{x}}\eta=v_z, \quad (3)$$

$$\partial_t\Phi+\frac{v^2}{2}+g\eta=f(t). \quad (4)$$

Equation (3) is due to mass conservation and the incompressibility condition, and Eq. (4) is the Bernoulli's equation. Here,  $f(t)$  is an undetermined function of time and  $v^2=v_{\bar{x}}^2+v_z^2$  is the total fluid velocity. Substituting Eq. (2) into boundary conditions (3) and (4) and expanding the latter in powers of  $\bar{x}$  yields

$$\frac{d}{dt}(\rho\eta_2)=-\frac{d}{dt}(\rho\eta_0)\frac{\tilde{c}_g k}{4}\left(k+4\frac{\tilde{c}_g+1}{\tilde{c}_g}\eta_2\right), \quad (5)$$

$$\begin{aligned} &\frac{d}{dt}\left[\frac{1}{\rho}\frac{d}{dt}(\rho\eta_0)\right]+\frac{\tilde{c}_g k}{2\rho^2}\left[\frac{d}{dt}(\rho\eta_0)\right]^2 \\ &+\frac{4}{k\tilde{c}_g}(g+\ddot{\eta}_0)\eta_2=0. \end{aligned} \quad (6)$$

In the limit of a small perturbation amplitude when  $k\eta_0\ll 1$ , the nonlinear terms are negligible (linear regime) and Eqs. (5) and (6) reduce to a well-known limit,<sup>14,15</sup>  $\eta_2^{\text{lin}}=-\tilde{c}_g k^2\eta_0^{\text{lin}}/4$  and

$$\frac{d}{dt}\left[\frac{1}{\rho}\frac{d}{dt}(\rho\eta_0^{\text{lin}})\right]-\gamma^2\eta_0^{\text{lin}}=0, \quad (7)$$

where  $\gamma(t)=\sqrt{kg(t)}$  is the growth rate and the superscript "lin" denotes perturbed quantities in the linear regime. An approximate solution of Eq. (7) can be found in the limit  $\dot{\rho}/\rho\ll\gamma$  using the Wentzel-Kramers-Brillouin (WKB) method.<sup>16</sup> According to such a method, the solution is sought in the form  $\eta_0^{\text{lin}}=e^{\tilde{S}(t)/\epsilon}$ , where

$$\epsilon\sim\max\left[(\gamma t_\rho)^{-1},(\gamma t_\gamma)^{-1}\right]\ll 1$$

is a small parameter and  $t_\rho=\rho/\dot{\rho}$  and  $t_\gamma=\gamma/\dot{\gamma}$  are characteristic time scales of the density and growth-rate variation. Then, up to the first order in  $\epsilon$ , Eq. (7) has the solution

$$\frac{\tilde{S}(t)}{\epsilon}=\pm\gamma-\frac{1}{2}\left(\frac{\dot{\rho}}{\rho}+\frac{\dot{\gamma}}{\gamma}\right). \quad (8)$$

Using Eq. (8), the physical optics approximation of  $\eta_0$  becomes

$$\eta_0^{\text{lin}}=\sqrt{\frac{\rho(0)\gamma(0)}{\rho(t)\gamma(t)}}\left[c_1e^{\int_0^t\gamma(t')dt'}+c_2e^{-\int_0^t\gamma(t')dt'}\right], \quad (9)$$

where integration constants  $c_1$  and  $c_2$  depend on the initial amplitude  $\eta_0(0)$  and the initial bubble velocity  $\dot{\eta}_0(0)$ :

$$c_1=\frac{\eta_0(0)}{2}\left[1+\frac{1}{2\gamma}\left(\frac{\dot{\rho}}{\rho}+\frac{\dot{\gamma}}{\gamma}\right)\right]_{t=0}+\frac{\dot{\eta}_0(0)}{2\gamma(0)},$$

$$c_2=\frac{\eta_0(0)}{2}\left[1-\frac{1}{2\gamma}\left(\frac{\dot{\rho}}{\rho}+\frac{\dot{\gamma}}{\gamma}\right)\right]_{t=0}-\frac{\dot{\eta}_0(0)}{2\gamma(0)}.$$

When the perturbation amplitude becomes large enough,  $k\eta_0 > 1$ , the bubble growth slows down from the exponential [Eq. (9)] to a power-law dependence. At such amplitudes, the nonlinear terms cannot be neglected (nonlinear regime), and Eqs. (5) and (6) can be solved in the limit  $|\dot{\rho}|/\rho \ll \sqrt{kg}$  and  $|\dot{\eta}_0/\eta_0| \gg \dot{\rho}/\rho$ . The leading-order solution of Eq. (5) becomes  $\eta_2^{\text{nl}} = -\tilde{c}_g k/4(1+\tilde{c}_g)$ , where the superscript “nl” denotes the perturbations in the nonlinear regime. Substituting  $\eta_2^{\text{nl}}$  into Eq. (6) gives

$$\begin{aligned} & -\frac{2}{\tilde{c}_g+1}\dot{a}+ka^2-\frac{2}{\tilde{c}_g(1+\tilde{c}_g)}\left(\frac{\dot{\rho}}{\rho}a+g\right) \\ & =-\frac{2\rho\eta_0}{\tilde{c}_g(1+\tilde{c}_g)}\frac{d}{dt}\left(\frac{\dot{\rho}}{\rho^2}\right), \end{aligned} \quad (10)$$

where  $a(t) = -d_t(\rho\eta_0)/\rho$  is the amplitude of the velocity potential defined in Eq. (2). The perturbation growth in the nonlinear regime changes from the exponential to a power law; therefore,  $ka^2 \gg \dot{a}$  and the first term in Eq. (10) can be neglected. Then, keeping the terms up to order  $t_p^{-1}$  in Eq. (10) yields

$$\frac{d(\rho\eta_0^{\text{nl}})}{dt} = -\frac{\dot{\rho}}{2kC_g} + \frac{\rho\gamma(t)}{\sqrt{C_g k}}, \quad (11)$$

where  $C_g = \tilde{c}_g(1+\tilde{c}_g)/2$ . Integrating Eq. (11) leads to

$$\begin{aligned} \eta_0^{\text{nl}}(t) & = \frac{1}{\sqrt{C_g k \rho(t)}} \int_{t_s}^t \rho(t') \gamma(t') dt' \\ & + \eta_S \frac{\rho_s}{\rho(t)} + \frac{\rho_s/\rho(t)-1}{2C_g k}, \end{aligned} \quad (12)$$

where  $t_s$  is the saturation time,  $\rho_s = \rho(t_s)$ , and  $\eta_S = \eta_0(t_s)$  is the bubble amplitude at the saturation time (saturation amplitude). Following Ref. 4, the saturation amplitude can be estimated by equating the bubble velocities  $\dot{\eta}_0$  calculated in the linear and nonlinear regimes using Eqs. (9) and (11), respectively. The result takes the form

$$\eta_S = \frac{1}{\sqrt{C_g k}} \left\{ 1 + \frac{1}{2\gamma} \left[ \frac{\dot{\gamma}}{\gamma} - \frac{\dot{\rho}}{\rho} \left( 1 + \frac{1}{\sqrt{C_g}} \right) \right] \right\}_{t=t_s}. \quad (13)$$

Thus, to the lowest order,  $\eta_S = 1/\sqrt{C_g k}$  and Eq. (12) becomes

$$\begin{aligned} \eta_0^{\text{nl}}(t) & = \eta_S \frac{\rho_s}{\rho(t)} \left\{ \int_{t_s}^t \frac{\rho(t')}{\rho_s} \gamma(t') dt' \right. \\ & \left. + 1 + \frac{1}{2\sqrt{C_g}} \left[ 1 - \frac{\rho(t)}{\rho_s} \right] \right\} \\ & = \frac{1}{\rho(t)} \int_{t_s}^t \rho(t') U_L(t') dt' \\ & + \eta_S \left\{ \frac{\rho_s}{\rho(t)} + \frac{1}{2\sqrt{C_g}} \left[ \frac{\rho_s}{\rho(t)} - 1 \right] \right\}, \end{aligned} \quad (14)$$

where

$$U_L(t) = \sqrt{\frac{g(t)}{C_g k}} \quad (15)$$

is the Layzer velocity. It is convenient in many applications to express the nonlinear bubble evolution in terms of the linear perturbation growth.<sup>17</sup> For the large linear growth factors  $[\eta_0 \gg \eta_0(0)]$ , Eq. (9) can be rewritten as

$$\eta_0^{\text{lin}}(t) = \eta_S \sqrt{\frac{\rho_s \gamma(t_s)}{\rho(t) \gamma(t)}} e^{\int_{t_s}^t \gamma(t') dt'}. \quad (16)$$

Taking the logarithm of both sides in the last equation yields

$$\int_{t_s}^t \gamma(t') dt' = \ln \frac{\eta_0^{\text{lin}}(t)}{\eta_S} + \frac{1}{2} \ln \frac{\rho(t) \gamma(t)}{\rho_s \gamma(t_s)}. \quad (17)$$

The second term in the right-hand side of Eq. (17) is logarithmically small at large times with respect to the first term and can be neglected without a significant loss in accuracy. With the help of Eq. (17), the nonlinear bubble amplitude (14) can be rewritten in terms of the linear perturbation growth:

$$\eta_0^{\text{nl}} = \eta_S \left\{ \ln \frac{\eta_0^{\text{lin}}(t)}{\eta_S} - \int_{t_s}^t \ln \left[ \frac{\eta_0^{\text{lin}}(t')}{\eta_S} \right] \frac{\dot{\rho}(t')}{\rho(t')} dt' + \frac{\rho_s}{\rho(t)} + \frac{1}{2\sqrt{C_g}} \left[ \frac{\rho_s}{\rho(t)} - 1 \right] \right\}. \quad (18)$$

The saturation time  $t_s$  is easily obtained using Eq. (9):<sup>7</sup>

$$\int_0^{t_s} \gamma(t') dt' - \frac{1}{2} \ln \left[ \frac{\gamma(t_s) \rho_s}{\rho(0) \gamma(0)} \right] = \ln(\eta_S/c_1). \quad (19)$$

The second term in the left-hand side of Eq. (19) has a weak logarithmic time dependence and can therefore be neglected. Substituting  $c_1 \approx \eta_0(0)/2$ , Eq. (19) reduces to

$$\int_0^{t_s} \gamma(t') dt' \approx \ln \frac{2\eta_S}{\eta_0(0)}. \quad (20)$$

Equation (20) defines the saturation time  $t_s$  in terms of the initial amplitude  $\eta_0(0)$ .

Equation (11) shows that the temporal density variation modifies the asymptotic bubble velocity  $U_b$ :

$$U_b \equiv \dot{\eta}_0 \rightarrow U_L - \frac{\dot{\rho}}{\rho} \left( \eta_0 + \frac{1}{2C_g k} \right). \quad (21)$$

In the case of the decompression flow when the density decreases in time ( $\dot{\rho} < 0$ ), the bubble grows faster, and, in the case of compression ( $\dot{\rho} > 0$ ), the bubble grows slower than the classical Layzer velocity  $U_L = \sqrt{g/kC_g}$ .

Next, to validate the results of the analysis, we compare the bubble evolution in the three-dimensional geometry ( $\tilde{c}_g = 1$ )

calculated using the system (5)–(6) and the results of asymptotic analysis [Eqs. (9) and (14)]. The gravitational field is assumed in the form  $g = g_0 / [1 + (t/t_g)^{s_g}]$ . The fluid density changes in time as (a)  $\rho(t) = \rho_0 [1 + C_\rho (t/t_0)^{s_\rho}]$  and (b)  $\rho(t) = \rho_0 (1 + D_\rho \cos \Omega t)$ , where  $s_g$  and  $s_\rho$  are the power indexes for acceleration and fluid density, respectively, and  $C_\rho$ ,  $D_\rho$ ,  $t_0$ , and  $\Omega$  are the normalization constants. Figure 102.48 shows a plot of the bubble amplitude calculated for case (a) with  $g_0 = 10 \lambda/t_0^2$ ,  $t_g = t_0$ ,  $s_g = 1$ ,  $s_\rho = 2$ ,  $C_\rho = 0.25$  (solid line),  $C_\rho = 0$  (dashed line), and  $C_\rho = -0.15$  (dotted line). The initial conditions are  $\eta_0(0) = \lambda/200$  and  $\dot{\eta}_0(0) = \lambda/(200 t_0)$ . Thick lines represent the exact solutions of Eqs. (5) and (6); thin lines show the WKB solution for  $t < t_s$  and the asymptotic solution (14) after  $t = t_s$ . Note the larger amplification factor of the bubble amplitude in the decompression flow. Figure 102.49 plots the linear (thin lines) and nonlinear (thick lines) perturbation growth. Observe that the value of  $\eta_S$  calculated using

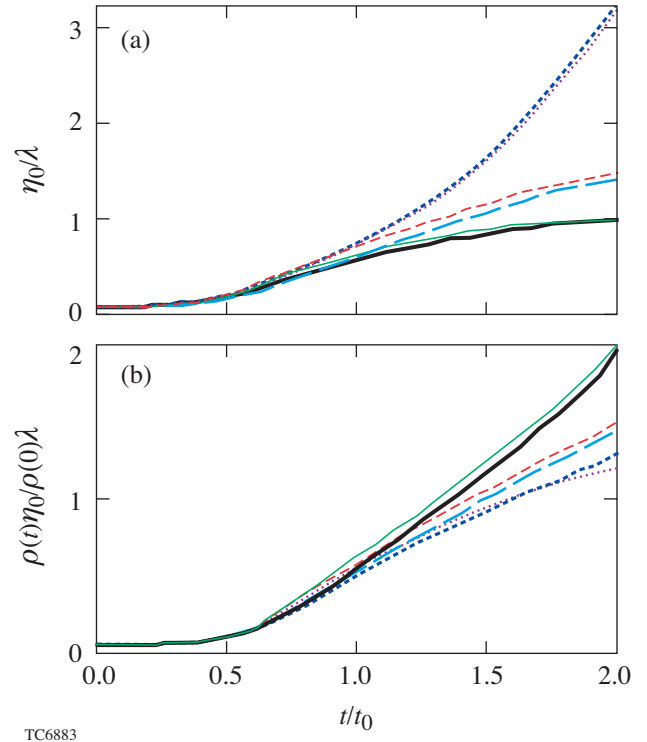


Figure 102.48

Plot of normalized bubble amplitude calculated using the exact numerical solution of Eqs. (5) and (6) (thick lines) and analytical solutions (9) and (14) (thin lines). The solid lines correspond to the fluid compression with  $C_\rho = 0.25$ , the dashed lines represent the constant density case (classical Layzer's model<sup>4</sup>), and the dotted lines are obtained for the decompression flow with  $C_\rho = -0.15$ .

Eq. (13) represents a good approximation to the saturation amplitude. The bubble evolution in case (b) is plotted in Fig. 102.50 for  $D_\rho = 0.3$  (solid line) and  $D_\rho = -0.3$  (dashed line). The initial conditions for this case are  $\eta_0 = \lambda/2 \times 10^{-3}$  and  $\dot{\eta}_0 = \Omega\lambda/2 \times 10^{-3}$  and  $t_g = 1/\Omega$ . A good agreement between the exact solution and the asymptotic formulas validates the accuracy of the performed analysis.

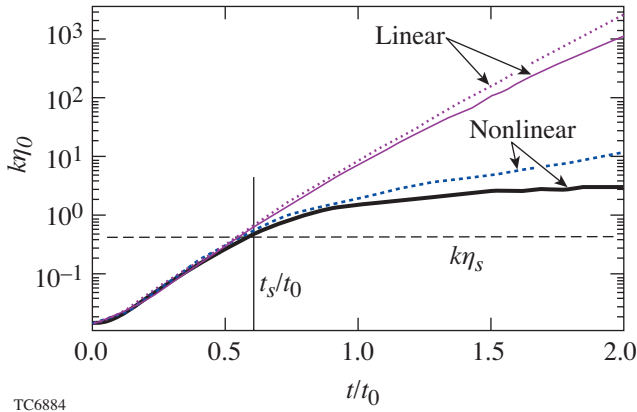


Figure 102.49

Plot of normalized bubble amplitude calculated using the exact numerical solution of Eqs. (5) and (6) with (thick lines) and without (thin lines) nonlinear terms. The solid and dotted lines correspond to  $C_\rho = 0.25$  and  $-0.15$ , respectively. The dashed line shows the saturation amplitude defined in Eq. (44).

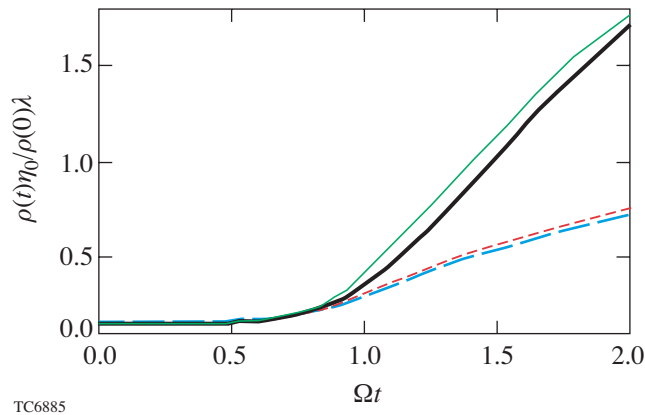


Figure 102.50

Plot of normalized bubble amplitude calculated using the exact numerical solution of Eqs. (5) and (6) (thick lines) and analytical solutions (9) and (14) (thin lines). The solid and dashed lines correspond to  $D_\rho = 0.3$  and  $-0.3$ , respectively.

To comment on the effects of temporal density variation on the asymptotic behavior of the Richtmyer–Meshkov (RM) instability, such an instability occurs when a shock passes through a corrugated interface between two fluids. As opposed to RT instability, the instability drive in this case has a finite duration (of the order of the sound-wave propagation across the perturbation wavelength). Thus, the asymptotic evolution of the bubble amplitude can be found using Eq. (10) with  $g = 0$ . When the fluid density does not change with time ( $\dot{\rho} = 0$ ), the sum of the first two terms in Eq. (10) must be zero. This yields a decay in time velocity<sup>5,7</sup>

$$\dot{\eta}_0^{\text{RM}} \rightarrow U_L^{\text{RM}} = 2/[(\tilde{c}_g + 1)kt]$$

and logarithmically growing bubble amplitude  $\eta_0^{\text{RM}} \sim \ln t$ . For a finite density derivative, one can attempt to generalize Eq. (14) to RM instability by replacing  $U_L$  with  $U_L^{\text{RM}}$ :

$$\eta_0^{\text{RM}} \rightarrow \frac{2}{k(\tilde{c}_g + 1)\rho(t)} \int^t \frac{\rho(t')}{t'} dt'. \quad (22)$$

Equation (22) is the result of balancing the first two terms in Eq. (10) and neglecting its right-hand side. It is easy to show, however, that, opposed to the RT instability, the right-hand side of Eq. (10) cannot be considered small in the RM instability at all times, regardless of the value of  $\dot{\rho}/\rho$ . Indeed, substituting the constant-density solution into Eq. (10) shows that the first two terms decrease in time ( $\sim 1/t^2$ ), while the right-hand side has a factor of  $\ln t$ . Thus, even a small density variation can significantly change the asymptotic behavior of the bubble velocity in the RM instability. Although Eq. (22) predicts correctly the trend of the effect, the accuracy of such a scaling is inadequate. To illustrate a strong dependence on the density variation, Fig. 102.51 plots the bubble velocity calculated for densities  $\rho = \rho_0$  (dashed line) and  $\rho = \rho_0 [1 - \epsilon(t/t_0)^2]$  (solid line), where  $\epsilon = 5 \times 10^{-4}$ . The velocities are plotted up to the time when the density difference between two cases is only 10%. The bubble velocity, however, is twice as large with the time-dependent density. The approximate solution (22), shown by the dotted line, gives only half of the decompression effect. For a more accurate estimate, the right-hand side of Eq. (10) must be retained. The solution in this case, however, cannot be written in a closed analytical form for an arbitrary density variation.

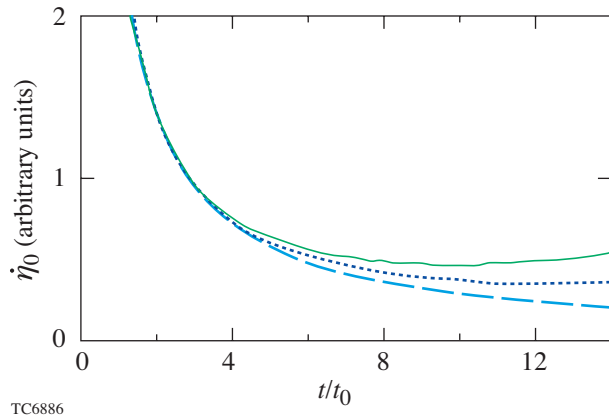


Figure 102.51

The asymptotic bubble velocity for RM instability. The dashed line represents the constant-density solution ( $\sim 1/t$ ), the solid line is the result of the exact solution of Eqs. (5) and (6) with time-dependent density  $\rho = \rho_0 [1 - 5 \times 10^{-4} (t/t_0)^2]$ , and the dotted line shows scaling defined in Eq. (22).

### Bubble Growth in Spherical Geometry

In a spherical shell of uniform density  $\rho$  with an outer radius  $r_0$  and inner radius  $r_1$ , the fluid density outside the shell is assumed to be much smaller than  $\rho$  ( $A_T = 1$ ). The shell interfaces are distorted with a single-mode perturbation of the mode number  $\ell$ . To simplify the analysis, a short-wavelength limit was used when the perturbation wavelength was much smaller than the shell thickness  $\ell(r_0 - r_1)/r_0 \gg 1$  or  $\ell \gg 1$ . The perturbations at the inner and outer surfaces in such an approximation are decoupled and can be treated separately. One must keep in mind, however, that even though only a single interface is considered, the product  $\rho r_0^3$  is not a constant. If the outer shell boundary is considered, the points where the shell interface has the maximum radii correspond to the perturbation spikes and the points of the minimum radii correspond to the perturbation bubbles. Following Layzer's approach, only the bubble evolution is described. In addition, similar to the analysis in the previous section, the effects due to the surface tension and thermal conduction are neglected.

A bubble is assumed to be symmetric with respect to the polar angle  $\phi$ . The axis of symmetry is along  $z$  direction. Solution of the Poisson's equation

$$\nabla^2 \Phi = \frac{1}{r^2} \frac{\partial}{\partial r} \left( r^2 \frac{\partial \Phi}{\partial r} \right) + \frac{1}{r^2 \sin \theta} \frac{\partial}{\partial \theta} \left( \sin \theta \frac{\partial \Phi}{\partial \theta} \right) = -\frac{\dot{\rho}}{\rho} \quad (23)$$

can be written in the form

$$\Phi = \frac{r_0}{\ell} \left[ a(t) \left( \frac{r}{r_0} \right)^\ell + b(t) \left( \frac{r_0}{r} \right)^{\ell+1} \right] P_\ell(\cos \theta) - \frac{c(t)}{r} - \frac{\dot{\rho} r^2}{\rho 6}, \quad (24)$$

where  $P_\ell$  is the Legendre polynomial,  $\theta$  is the azimuthal angle,  $a(t)$  and  $b(t)$  are undetermined functions of time, and function  $c(t)$  is defined by the unperturbed flow condition  $\partial_r \Phi(r_0) = \dot{r}_0$ ,

$$c(t) = r_0^2 \left( \dot{r}_0 + \frac{r_0 \dot{\rho}}{3 \rho} \right). \quad (25)$$

Here,  $\dot{r}_0$  is the velocity of the outer shell boundary. Since terms up to  $\theta^2$  are retained in the analysis, only the fundamental harmonic is kept in Eq. (24). In what follows an imploding shell with the unstable outer interface is considered. Thus,  $b(t) = 0$  must satisfy the boundary condition at  $(r/r_0)^\ell \rightarrow 0$ . The case of the expanding shell ( $a = 0$ ) can be treated in a similar fashion and will not be described in detail in this article. Solution (24) must satisfy the boundary condition at  $r = r_0 + \eta(t, \theta)$ , where  $\eta$  is the interface distortion. The first condition is easily derived from the mass conservation equation

$$\dot{\eta} + \frac{v_\theta}{r_0 + \eta} \partial_\theta \eta = v_r - \dot{r}_0. \quad (26)$$

Then, assuming a uniform density inside the shell, the momentum equation is integrated to yield Bernoulli's equation

$$-\frac{p}{\rho} = \partial_t \Phi + \frac{1}{2} v^2 - f(t), \quad (27)$$

where  $p$  is the pressure,  $v^2 = v_r^2 + v_\theta^2$  is the total velocity, and  $f(t)$  is an undetermined function of time. Pressure must be continuous across the boundary; therefore, Eq. (27) reduces to

$$\partial_t \Phi + \frac{1}{2} v^2 = \tilde{f}(t), \quad (28)$$

where  $\tilde{f}(t) = f(t) - p_a(t)/\rho$  and  $p_a(t)$  is the drive pressure. To find the distortion amplitude  $\eta$ , the boundary conditions

(26) and (28) and the potential (24) are expanded near the tip of the bubble in series of azimuthal angle  $\theta$ :

$$\begin{aligned}\eta(t, \theta) &= \eta_0 + \eta_2 \theta^2 + O(\theta^4), \\ P_\ell(\cos \theta) &= 1 - \frac{\ell(\ell+1)}{4} \theta^2 + O(\theta^4).\end{aligned}\quad (29)$$

Note that  $\eta_0 < 0$  at the bubble. The resulting system of differential equations takes the form

$$\begin{aligned}3 \frac{d}{dt} (\rho r_0^2 \eta_2) - \frac{2\eta_2}{r_0} \frac{d(\rho r_0^3)}{dt} \left[ 1 - \left( \frac{r_0}{r_0 + \eta_0} \right)^3 \right] \\ = \left( \frac{r_0}{r_0 + \eta_0} \right)^2 \frac{d}{dt} \rho \left[ (r_0 + \eta_0)^3 - r_0^3 \right] \\ \times \left[ \frac{2\ell}{r_0 + \eta_0} \eta_2 - \frac{\ell(\ell+1)}{4} \right],\end{aligned}\quad (30)$$

$$\begin{aligned}\frac{d}{dt} \left\{ \frac{1}{3\rho(r_0 + \eta_0)} \frac{d}{dt} \rho \left[ (r_0 + \eta_0)^3 - r_0^3 \right] \right\} \left( \frac{\eta_2}{r_0 + \eta_0} - \frac{\ell+1}{4} \right) \\ + \frac{1}{3\rho(r_0 + \eta_0)^2} \frac{d}{dt} \rho \left[ (r_0 + \eta_0)^3 - r_0^3 \right] \\ \times \left\{ \frac{1}{3\rho(r_0 + \eta_0)^2} \frac{d}{dt} \rho \left[ (r_0 + \eta_0)^3 - r_0^3 \right] \right. \\ \times \left[ \frac{(\ell+1)^2}{8} - \frac{\eta_2}{r_0 + \eta_0} \right] - \frac{\eta_2}{\rho(r_0 + \eta_0)^3} \frac{d(\rho r_0^3)}{dt} \left. \right\} \\ + \frac{\eta_2}{(r_0 + \eta_0)^2} \left\{ r_0^2 \ddot{\eta}_0 + \left[ (r_0 + \eta_0)^3 - r_0^3 \right] \right. \\ \times \left. \left[ \frac{2r_0^3}{9(r_0 + \eta_0)^3} \left( \frac{d_t \rho r_0^3}{\rho r_0^3} \right)^2 + \frac{4}{9} \left( \frac{\dot{\rho}}{\rho} \right)^2 - \frac{\ddot{\rho}}{3\rho} \right] \right\} = 0.\end{aligned}\quad (31)$$

Although the system (30)–(31) can be easily integrated numerically for a given trajectory  $r_0(t)$  and shell density  $\rho(t)$ , it is difficult to get a physical insight on the convergence effects from this rather cumbersome system. To obtain a scaling of the asymptotic nonlinear bubble amplitude with the flow parameters, the equations can be significantly simplified by assuming that the bubble amplitude is much smaller than the shell radius  $|\eta_0| \ll r_0$  (a combination  $\ell|\eta_0|/r_0$ , however, can be arbitrarily large since  $\ell \gg 1$ ). Simple calculations reduce Eqs. (30) and (31) in this case to

$$\frac{d}{dt} (\rho r_0^2 \eta_2) = -\frac{\ell(\ell+1)}{4} \frac{d}{dt} (\rho r_0^2 \eta_0) \left( 1 - \frac{8}{\ell+1} \frac{\eta_2}{r_0} \right), \quad (32)$$

$$\begin{aligned}\frac{d}{dt} \left[ \frac{d_t (\rho r_0^2 \eta_0)}{\rho r_0} \right] - \frac{\ell+1}{2} \left[ \frac{d_t (\rho r_0^2 \eta_0)}{\rho r_0^2} \right]^2 - \frac{4\eta_2}{\ell+1} (\ddot{\eta}_0 + \ddot{\eta}_0) \\ = -(\ell+1) \frac{\eta_0^2}{r_0^2} \frac{d_t (\rho r_0^2 \eta_0)}{\rho r_0} \frac{d_t (\rho r_0^3)}{\rho r_0^3}.\end{aligned}\quad (33)$$

The term in the right-hand side of Eq. (33) is retained for the high-convergence-ratio implosions.

When  $\ell|\eta_0|/r_0 \ll 1$ , the nonlinear terms can be neglected, leading to  $\eta_2^{\text{lin}} = -\eta_0^{\text{lin}} \ell(\ell+1)/4$ . Equation (33) recovers, in this limit, the results of Refs. 15, 18, and 19,

$$\frac{d}{dt} \left( \frac{r_0^2 \xi_0^{\text{lin}}}{m} \right) + \ell \frac{\ddot{\eta}_0 r_0}{m} \xi_0^{\text{lin}} = 0, \quad (34)$$

where  $\xi_0 = \rho(t) r_0^2(t) \eta_0$ ,  $m(t) = \rho(t) r_0^3(t)$ , and the dot denotes the time derivative. The new function  $\xi_0$  can be related to a very important parameter characterizing the shell stability. In comparing performances of different implosions with respect to the shell breakup, it is not the bubble amplitude itself, but the ratio of the amplitude  $\eta_0$  to the in-flight shell thickness  $\Delta$  that must be considered. The parameter  $\Upsilon = |\eta_0|/\Delta$  is referred to as an instability factor. Multiplying the denominator and numerator in  $\Upsilon$  by  $\rho r_0^2$ , we obtain  $\Upsilon = 4\pi |\xi_0|/M_{\text{sh}}$ , where  $M_{\text{sh}} = 4\pi \rho r_0^2 \Delta$  is the shell mass. Thus, divided by the shell mass,  $|\xi_0|$  shows how close the imploding shell is to

breaking up. If  $|\xi_0|/M_{\text{sh}} \simeq (4\pi)^{-1}$ , the shell integrity is compromised by the instability growth.

An approximate solution of Eq. (34) can be found in the limit  $\ell \gg 1$  using the WKB method. Writing the solution as  $\xi_0^{\text{lin}} = e^{S/\epsilon}$  ( $\epsilon \ll 1$  is a small parameter), Eq. (34) becomes

$$\dot{S}^2 + \epsilon \left[ \ddot{S} + \left( 2 \frac{\dot{r}_0}{r_0} - \frac{\dot{m}}{m} \right) \dot{S} \right] + \epsilon^2 \ell \frac{\ddot{r}_0}{r_0} = 0. \quad (35)$$

To satisfy Eq. (35) we must require  $\epsilon = 1/\sqrt{\ell}$ . Then, expanding  $S$  in powers of  $\epsilon$ , the solution up to the first order in  $\epsilon$  takes the form

$$S = \pm \int^t \sqrt{-\frac{\ddot{r}_0(t')}{r_0(t')}} dt' + \frac{\epsilon}{2} \ln \left( \frac{m}{r_0^2} \sqrt{-\frac{r_0}{\ddot{r}_0}} \right). \quad (36)$$

The WKB solution (36) is valid if the shell acceleration  $\ddot{r}_0$  does not go to zero during the implosion. With the help of Eq. (36),  $\xi_0^{\text{lin}}$  becomes

$$\xi_0^{\text{lin}} = \frac{\sqrt{m(t)m(0)}}{r_0(t)} \sqrt{\frac{\Gamma(0)}{\Gamma(t)}} \times \left[ C_1 e^{\int_0^t \Gamma(t') dt'} + C_2 e^{-\int_0^t \Gamma(t') dt'} \right], \quad (37)$$

where

$$\Gamma(t) = \sqrt{-\ell \frac{\ddot{r}_0(t)}{r_0(t)}},$$

and the integration constants  $C_1$  and  $C_2$  depend on the initial bubble amplitude  $\eta_0(0)$  and bubble velocity  $\dot{\eta}_0(0)$ ,

$$C_1 = \frac{\eta_0(0)}{2} \left\{ 1 + \frac{1}{2\Gamma(0)} \left[ \frac{\dot{m}(0)}{m(0)} + \frac{\dot{\Gamma}(0)}{\Gamma(0)} \right] \right\} + \frac{\dot{\eta}_0(0)}{2\Gamma(0)},$$

$$C_2 = \frac{\eta_0(0)}{2} \left\{ 1 - \frac{1}{2\Gamma(0)} \left[ \frac{\dot{m}(0)}{m(0)} + \frac{\dot{\Gamma}(0)}{\Gamma(0)} \right] \right\} - \frac{\dot{\eta}_0(0)}{2\Gamma(0)}.$$

In the limit of  $\ell \gg 1$ , coefficients  $C_1$  and  $C_2$  in the leading order reduce to  $C_1 = C_2 \simeq \eta_0(0)/2$ . The perturbations grow according to Eq. (37) until the nonlinear effects become important and the bubble growth slows down (nonlinear saturation). To find the perturbation amplitude  $\eta_S$  at which the transition from linear to nonlinear growth occurs, we must first determine the bubble evolution in the nonlinear regime. Then, equating the linear and nonlinear bubble velocities will define an approximate saturation amplitude.<sup>4</sup>

We begin the nonlinear analysis with Eq. (32), which can be rewritten in the limit  $\ell \gg 1$  as

$$\dot{\xi}_0 \left( 1 - 8\epsilon^2 \frac{\eta_2}{r_0} \right) = -4\epsilon^4 \frac{d}{dt} (\rho r_0^2 \eta_2), \quad (38)$$

where  $\epsilon = 1/\sqrt{\ell}$ . The left-hand side of Eq. (38) is of the order of  $\epsilon^0 \xi_0$ ; the right-hand side is of the order of  $\epsilon^4 \eta_2$ . It can be shown that to satisfy Eq. (38), we must order  $\eta_2^{\text{nl}}/r_0 \sim \epsilon^{-2}$ . Here, the superscript “nl” denotes the functions in the nonlinear regime. To the lowest order in  $\epsilon$ , the latter ordering gives  $\eta_2^{\text{nl}}/r_0 = \ell/8$ . Keeping the higher-order terms in  $\eta_2^{\text{nl}}$  yields

$$\frac{\eta_2^{\text{nl}}}{r_0} = \frac{\ell}{8} + \frac{\dot{m}(t)}{16 \dot{\xi}_0^{\text{nl}}}. \quad (39)$$

For a decreasing  $m(t)$  (which is almost always the case in a converging shell),  $\eta_2$  reaches an asymptotic value that is slightly larger than  $r_0 \ell/8$  (keep in mind that the bubble amplitude  $\eta_0$  is negative). The difference between  $\eta_2/r_0$  and  $\ell/8$  decays in time in the case of growing  $|\xi_0|$ . When the ratio  $\eta_0/r_0$  cannot be neglected compared to unity, the solution (39), according to Eq. (30), is multiplied by a factor  $(1 + \eta_0^{\text{nl}}/r_0)$ :

$$\frac{\eta_2^{\text{nl}}}{r_0} = \left[ \frac{\ell}{8} + \frac{\dot{m}(t)}{16 \dot{\xi}_0^{\text{nl}}} \right] \left( 1 - \frac{|\eta_0^{\text{nl}}|}{r_0} \right). \quad (40)$$

Such a factor further reduces the asymptotic value of  $\eta_2^{\text{nl}}$  at the large bubble amplitudes. A detailed comparison with the

exact numerical solution of Eqs. (30) and (31) shows that  $\eta_2^{\text{nl}}$  can be replaced by  $r_0\ell/8$  in Eq. (33) without significant loss in accuracy. This yields

$$\begin{aligned} & \ell \left( \dot{\xi}_0^{\text{nl}} \right)^2 - \dot{\xi}_0^{\text{nl}} \dot{m} \left[ 1 + 2\ell \left( \frac{\xi_0^{\text{nl}}}{m} \right)^2 \right] + 2m\dot{\xi}_0^{\text{nl}} \frac{\dot{r}_0}{r_0} + \frac{\ddot{r}_0}{r_0} m^2 \\ &= \frac{m^2}{r_0^2} \frac{d}{dt} \left( \frac{\dot{\xi}_0^{\text{nl}}}{\rho r_0} \right) + \xi_0^{\text{nl}} \frac{m^2}{r_0} \frac{d}{dt} \left( \frac{\dot{\rho}}{\rho^2 r_0^2} \right). \end{aligned} \quad (41)$$

As in the planar geometry case,  $\dot{a}(t)$  can be neglected with respect to  $\ell a^2(t)$  in the nonlinear regime, where  $a = \dot{\xi}_0/\rho r_0^2$  is the amplitude in the velocity potential defined in Eq. (24). Furthermore, we also drop the second term in the right-hand side of Eq. (41). This term is identically zero at a constant density; if  $\dot{m} = 0$  (solid sphere implosion), the term is equal to  $-3m^2(\ddot{r}_0/r_0)(\eta_0^{\text{nl}}/r_0)$ , which is smaller by a factor  $\eta_0^{\text{nl}}/r_0$  compared to the last term in the left-hand side of Eq. (41). Next, solving the second-order algebraic equation for  $\dot{\xi}_0^{\text{nl}}$  yields

$$\begin{aligned} \dot{\xi}_0^{\text{nl}} &= \dot{m} \left[ \frac{1}{2\ell} + \left( \frac{\xi_0^{\text{nl}}}{m} \right)^2 \right] \\ &= \sqrt{\dot{m}^2 \left[ \frac{1}{2\ell} + \left( \frac{\xi_0^{\text{nl}}}{m} \right)^2 \right]^2 - \frac{2\dot{m}\dot{r}_0}{\ell r_0} \xi_0^{\text{nl}} - \frac{\ddot{r}_0}{r_0} \frac{m^2}{\ell}}. \end{aligned} \quad (42)$$

As mentioned earlier, the approximate value of the saturation amplitude  $\eta_S$  can be obtained by equating  $\dot{\xi}_0$  in the linear and nonlinear regimes. In the linear case, using the WKB solution (37), we write  $\dot{\xi}_0 = \sqrt{\ell} \dot{S}(t) \xi_0$ . This gives

$$\dot{\xi}_0 = \xi_0 \left[ \Gamma(t) + \frac{1}{2} \left( \frac{\dot{m}}{m} - 2 \frac{\dot{r}_0}{r_0} - \frac{\dot{\Gamma}}{\Gamma} \right) \right]. \quad (43)$$

Substituting Eq. (43) into Eq. (42) and neglecting terms with  $\xi_0^2$  (shell convergence ratio is assumed to be not very large at the time of the bubble saturation, so the terms with  $\xi_0^2$  are

small) yields the saturation amplitude

$$\frac{|\eta_S|}{r_0(t_s)} = \frac{|\xi_S|}{m_s} = \frac{1}{\ell} \left[ 1 + \frac{1}{\Gamma} \left( \frac{\dot{\Gamma}}{2\Gamma} + \frac{\dot{r}_0}{r_0} - \frac{\dot{m}}{m} \right) \right]_{t=t_s}, \quad (44)$$

where  $t_s$  is the saturation time,  $m_s = m(t_s)$ ,  $\eta_S = \eta_0(t_s)$ , and  $\xi_S = \xi_0(t_s)$ . Since  $\Gamma \sim \sqrt{\ell}$ , the bubble saturation amplitude, to the lowest order in  $\ell^{-1}$ , is  $|\eta_S| \sim r_0(t_s)/\ell$ . To find the bubble evolution after the saturation, we solve Eq. (42) in the limit of  $\ell \gg 1$ , expanding the solution  $\xi_0^{\text{nl}} = \xi_{00} + \xi_{01} + \dots$ , where  $\xi_{00}/\xi_{01} \sim \sqrt{\ell} \gg 1$ . Keeping the lowest-order terms in Eq. (42) gives

$$\xi_{00} = -\frac{1}{\ell} \int_{t_s}^t \Gamma(t') m(t') dt' + c_0, \quad (45)$$

where  $c_0$  is an integration constant. Substituting  $\xi_{00}$  back into Eq. (42) and retaining the terms of the order  $1/\ell$  yields  $\xi_{01}$ . Combining  $\xi_{00}$  and  $\xi_{01}$  and using the saturation condition  $\xi_0(t_s) = -m_s/\ell$  leads to

$$\begin{aligned} \xi_0^{\text{nl}} &= -m(t) I(t) + \frac{m(t) - 3m_s}{2\ell} \\ &+ \int_{t_s}^t \dot{m} \left[ I(t')^2 - I(t') \frac{\dot{r}_0}{r_0 \Gamma} \right] dt', \end{aligned} \quad (46)$$

where

$$\begin{aligned} I(t) &= \frac{1}{\ell m(t)} \int_{t_s}^t \Gamma(t') m(t') dt' \\ &= \frac{1}{m(t)} \int_{t_s}^t U_L^{\text{sp}}(t') \frac{m(t')}{r_0(t')} dt' \end{aligned}$$

and

$$U_L^{\text{sp}} = \sqrt{-\frac{\ddot{r}_0(t) r_0(t)}{\ell}}.$$

Equation (46) can be further simplified by taking the integral by parts,

$$\begin{aligned} & \int_{t_s}^t \dot{m} \left[ I(t')^2 - I(t') \frac{\dot{r}_0}{r_0 \Gamma} \right] dt' \\ &= m(t) \ln \left[ \frac{m(t)}{m_s} \right] \left( I^2 - I \frac{\dot{r}_0}{\Gamma r_0} \right) \\ & \quad - \int_{t_s}^t \ln \frac{m(t')}{m_s} \frac{d}{dt'} \left[ m(t') \left( I^2 - I \frac{\dot{r}_0}{\Gamma r_0} \right) \right] dt', \end{aligned} \quad (47)$$

and neglecting the second integral in the right-hand side of Eq. (47). This gives a relatively simple scaling with  $\sim 20\%$  error. Substituting Eq. (47) into Eq. (46) and replacing

$$1 + \left( \frac{\dot{r}_0}{r_0 \Gamma} - I \right) \ln \frac{m(t)}{m_s} \approx \left[ \frac{m(t)}{m_s} \right]^{\dot{r}_0 / r_0 \Gamma - I}$$

yields

$$\begin{aligned} \xi_0^{\text{nl}} & \approx -m(t) I(t) \left[ \frac{m(t)}{m_s} \right]^{\dot{r}_0 / (r_0 \Gamma) - I} + \frac{m(t) - 3m_s}{2\ell} \\ & \approx \xi_s \left\{ \left[ \frac{m(t)}{m_s} \right]^{\dot{r}_0 / (r_0 \Gamma) - I} \int_{t_s}^t \Gamma(t') \frac{m(t')}{m_s} dt' \right. \\ & \quad \left. + \frac{3 - m(t)/m_s}{2} \right\} \\ & = - \left[ \frac{m(t)}{m_s} \right]^{\dot{r}_0 / (r_0 \Gamma) - I} \int_{t_s}^t U_L^{\text{sp}}(t') \rho(t') r_0^2(t') dt' \\ & \quad + \xi_s \frac{3 - m(t)/m_s}{2}. \end{aligned} \quad (48)$$

To use Eq. (48), one must specify the saturation time  $t_s$ . The latter can be easily obtained with the help of Eq. (37). At the time of bubble saturation, the following equality must be satisfied:

$$\frac{m_s}{\ell} \approx |C_1| \frac{\sqrt{m_s m(0)}}{r_0(t_s)} \sqrt{\frac{\Gamma(0)}{\Gamma(t_s)}} e^{\int_0^{t_s} \Gamma(t') dt'}, \quad (49)$$

which leads to

$$\int_0^{t_s} \Gamma(t') dt' \approx \ln \left[ \frac{r_0(t_s)}{\ell |C_1|} \sqrt{\frac{m_s \Gamma(t_s)}{m(0) \Gamma(0)}} \right]. \quad (50)$$

It is sufficient in many cases to keep only the lowest-order terms in Eq. (50). This gives

$$\int_0^{t_s} \Gamma(t') dt' \approx \ln \left[ \frac{r_0(0)}{\ell |C_1|} \right] \approx \ln \left[ \frac{2r_0(0)}{\ell |\eta_0(0)|} \right]. \quad (51)$$

To obtain a more accurate value of  $t_s$ , one must solve Eq. (50).

It is interesting to note that the perturbation growth factors are smaller in a “compact” shell with a larger density than in a decompressed, lower-density shell [ $\eta_0 \sim 1/\sqrt{m}$  before and  $\eta_0 \sim m^{-I - \dot{r}_0 / (\Gamma r_0)}$  after the saturation]. The shell thickness  $\Delta$ , however, is inversely proportional to  $m$ ; therefore, the ratio  $\Upsilon = |\eta_0|/\Delta$  is larger in the higher-density shell [ $\Upsilon \sim \xi_0 \sim \sqrt{m(t)}$  in the linear regime and  $\Upsilon \sim m(t)$  in the nonlinear regime]. Thus, for the same shell trajectory, the thinner shell is more unstable.

As a next step, the nonlinear bubble evolution is expressed in terms of the linear perturbation growth. The linear growth can be calculated, for example, using the stability postprocessor described in Ref. 15. When the perturbation amplitude is much larger than the initial amplitude  $\eta_0(0)$ , Eq. (37) can be rewritten as

$$\eta_0^{\text{lin}} \approx \eta_s \sqrt{\frac{m_s \Gamma(t_s)}{m(t) \Gamma(t)}} e^{\Psi(t)}, \quad \Psi(t) = \int_{t_s}^t \Gamma(t') dt', \quad (52)$$

where  $\eta_S \simeq -r_0(t_s)/\ell$  is the saturation amplitude. Then,

$$\Psi(t) = \ln \frac{\eta_0^{\text{lin}}}{\eta_S} + \frac{1}{2} \ln \left[ \frac{\Gamma(t)m(t)}{\Gamma(t_s)m_s} \right]. \quad (53)$$

The linear RT growth is exponential; thus, assuming that  $\Gamma(t)$  and  $m(t)$  grow slower than  $\eta_0^{\text{lin}}$ , the second logarithm in the right-hand side of Eq. (53) can be neglected. Function  $I(t)$  in Eq. (48) can be rewritten in terms of the function  $\Psi(t)$ :

$$\ell I(t) = \Psi(t) - \frac{1}{m(t)} \int_{t_s}^t \Psi(t') \dot{m}(t') dt'.$$

With the help of the latter relation and substituting  $\ell \simeq -r_0(t_s)/\eta_S$ , Eq. (48) becomes

$$\begin{aligned} \eta_0^{\text{nl}}(t) = \eta_S \frac{r_0(t)}{r_0(t_s)} & \left\{ \left[ \ln \frac{\eta_0^{\text{lin}}(t)}{\eta_S} \right. \right. \\ & \left. \left. - \frac{1}{m(t)} \int_{t_s}^t \ln \frac{\eta_0^{\text{lin}}(t')}{\eta_S} \dot{m}(t') dt' \right] \left[ \frac{m_s}{m(t)} \right]^{\alpha_m(t)} \right. \\ & \left. + \frac{3}{2} \frac{m_s}{m(t)} - \frac{1}{2} \right\}, \quad (54) \end{aligned}$$

where

$$\begin{aligned} \alpha_m(t) = & -\frac{\dot{r}_0 \eta_0^{\text{lin}}(t)}{r_0 \dot{\eta}_0^{\text{lin}}} \\ & + \frac{|\eta_S|}{r_0(t_s)} \left[ \ln \frac{\eta_0^{\text{lin}}(t)}{\eta_S} - \frac{1}{m(t)} \int_{t_s}^t \ln \frac{\eta_0^{\text{lin}}(t')}{\eta_S} \dot{m}(t') dt' \right]. \end{aligned}$$

Equation (54) is especially simple in the case of a solid-sphere implosion when  $m = \rho r_0^3 = \text{const}$ ,

$$\eta_0^{\text{nl}}(t) \Big|_{\rho r_0^3 = \text{const}} = \eta_S \frac{r_0(t)}{r_0(t_s)} \left[ \ln \frac{\eta_0^{\text{lin}}(t)}{\eta_S} + 1 \right]. \quad (55)$$

Except for the factor  $r_0(t)/r_0(t_s)$ , Eq. (55) reproduces the asymptotic formula proposed in Ref. 17.

To validate the accuracy of the derived results, we compare the bubble evolution calculated using the exact system [Eqs. (30) and (31)] with the analytical scaling [Eqs. (37) and (48)]. Figure 102.52(a) plots the bubble amplitude for mode numbers  $\ell = 100$  and  $\ell = 200$ . The outer shell radius changes according to a power law  $r_0 = R_0(1-t/t_0)^{1/3}$ , where  $0 \leq t < t_0$ . The density is inversely proportional to the trajectory,

$$\rho(t) = \rho_0 [R_0/r_0(t)].$$

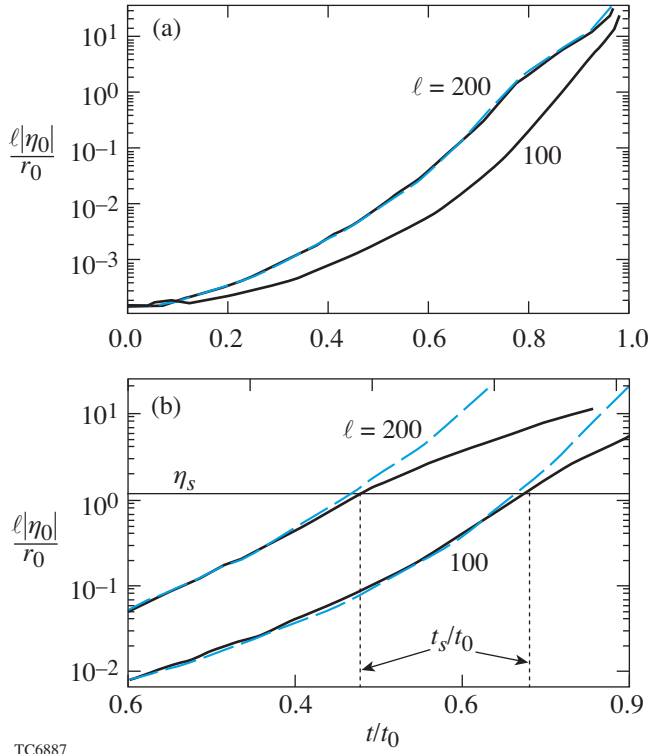
The initial conditions are

$$\eta_0 = -2 \times 10^{-4} R_0 / \ell$$

and

$$\dot{\eta}_0 = 2 \times 10^{-4} R_0 / \ell t_0.$$

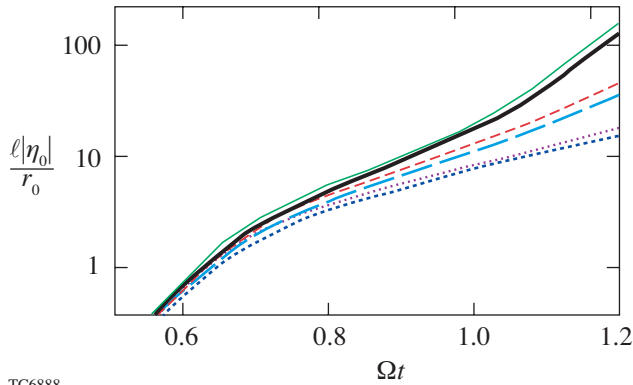
The solid lines represent the exact solution of Eqs. (30) and (31), and dashed lines are obtained using Eq. (37) for  $t < t_s$  and Eq. (48) for  $t > t_s$ . The saturation time  $t_s$  is defined as the time of intersection of the linear amplitude [Eq. (37)] with the saturation amplitude [Eq. (44)]. Figure 102.52(b) plots the normalized amplitudes with (solid curves) and without (dashed curves) the nonlinear effects. Observe that the saturation value defined by Eq. (44) reproduces very well the bubble amplitude at which the growth slows down and becomes nonlinear. Figure 102.53 plots the bubble evolution for the shell with  $r_0 = R_0 \cos \Omega t$  ( $0 \leq \Omega t < \pi/2$ ) and mode number  $\ell = 200$ . The initial conditions for the perturbations are the same as in the previous case ( $\Omega = 1/t_0$ ). The density is assumed to follow a power law of the radius,  $\rho(t) = \rho(0) [R_0/r_0(t)]^s$ . The thick lines represent the exact numerical solution of Eqs. (30) and (31), and the thin lines are the results of the asymptotic analysis. The solid, dashed, and dotted lines in Fig. 102.53



TC6887

Figure 102.52

(a) Plot of normalized bubble amplitude calculated using the exact numerical solution of Eqs. (30) and (31) (solid lines) and analytical solutions (37) and (48) (dashed lines). (b) Plot of the normalized bubble amplitude with (solid lines) and without (dashed lines) nonlinear terms.



TC6888

Figure 102.53

Bubble amplitude calculated using the exact numerical solution of Eqs. (30) and (31) (thick lines) and analytical solutions (37) and (48) (thin lines) for  $\rho = \text{const}$  (solid lines),  $\rho \sim 1/r_0$  (dashed lines), and  $\rho \sim 1/r_0^2$  (dotted lines).

correspond to  $s_\rho = 0, 1$ , and  $2$ , respectively. Note that the bubble growth factors decrease with increasing density. Good agreement between the exact solution and the analytic scaling confirms the accuracy of the asymptotic analysis.

In summary, Layzer's model to study the nonlinear bubble evolution in classical RT instability has been extended to include the temporal density variation and spherical convergence effects. The bubble amplitude in planar geometry with the time-dependent density  $\rho(t)$  was shown to asymptote to  $\int^t U_L(t')\rho(t')dt'/\rho(t)$ , where  $U_L = \sqrt{g/C_g k}$  and  $C_g = 3$  and  $C_g = 1$  for two- and three-dimensional geometries, respectively. The model applied to the spherical geometry predicted the nonlinear bubble amplitude

$$\eta \sim \bar{\eta}(t) \left[ m(t)/m_s \right]^{-|\dot{r}_0|/\ell U_L^{\text{SP}} - \bar{\eta}/r_0},$$

where  $r_0$  is the outer shell radius,

$$\bar{\eta}(t) = \int^t U_L^{\text{SP}}(t')\rho(t')r_0^2(t')dt'/\rho(t)r_0^2(t),$$

$$U_L^{\text{SP}}(t) = \sqrt{-\ddot{r}_0(t)r_0(t)/\ell},$$

$$m(t) = \rho(t)r_0^3(t),$$

$$m_s = m(t_s),$$

$t_s$  is the saturation time, and  $\ell$  is the mode number.

#### ACKNOWLEDGMENT

This work was supported by the U.S. Department of Energy Office of Inertial Confinement Fusion under Cooperative Agreement No. DE-FC52-92SF19460, the University of Rochester, and the New York State Energy Research and Development Authority. The support of DOE does not constitute an endorsement by DOE of the views expressed in this article.

#### REFERENCES

1. J. D. Lindl, *Inertial Confinement Fusion: The Quest for Ignition and Energy Gain Using Indirect Drive* (Springer-Verlag, New York, 1998); S. Atzeni and J. Meyer-ter-Vehn, *The Physics of Inertial Fusion: Beam Plasma Interaction, Hydrodynamics, Hot Dense Matter*, International Series of Monographs on Physics (Clarendon Press, Oxford, 2004).
2. B. A. Remington *et al.*, Phys. Plasmas **7**, 1641 (2000).

3. Lord Rayleigh, in *Scientific Papers* (Cambridge University Press, Cambridge, England, 1900), Vol. II, pp. 200–207.
4. D. Layzer, *Astrophys. J.* **122**, 1 (1955).
5. D. Oron *et al.*, *Phys. Plasmas* **8**, 2883 (2001); U. Alon *et al.*, *Phys. Rev. Lett.* **74**, 534 (1995); G. Dimonte, *Phys. Plasmas* **7**, 2255 (2000); G. Dimonte and M. Schneider *et al.*, *Phys. Fluids* **12**, 304 (2000).
6. G. Dimonte, *Phys. Rev. E* **69**, 056305 (2004); G. Dimonte *et al.*, *Phys. Fluids* **16**, 1668 (2004).
7. K. O. Mikaelian, *Phys. Rev. Lett.* **80**, 508 (1998); K. O. Mikaelian, *Phys. Rev. E* **67**, 026319 (2003).
8. Q. Zhang, *Phys. Rev. Lett.* **81**, 3391 (1998).
9. V. N. Goncharov, *Phys. Rev. Lett.* **88**, 134502 (2002).
10. Y. Yedwab *et al.*, presented at the 6th International Workshop on the Physics of Compressible Turbulent Mixing, Marseille, France, 18–21 June 1997, pp. 528–533.
11. D. Clark and M. Tabak, *Bull. Am. Phys. Soc* **49**, 281 (2004).
12. N. A. Inogamov and S. I. Abarzhi, *Physica D* **87**, 339 (1995); S. I. Abarzhi, *Phys. Rev. E* **59**, 1729 (1999).
13. G. Hazak, *Phys. Rev. Lett.* **76**, 4167 (1996); A. L. Velikovich and G. Dimonte, *Phys. Rev. Lett.* **76**, 3112 (1996).
14. G. I. Bell, Los Alamos National Laboratory, Los Alamos, NM, Report LA-1321 (1951).
15. V. N. Goncharov, P. McKenty, S. Skupsky, R. Betti, R. L. McCrory, and C. Cherfils-Clérouin, *Phys. Plasmas* **7**, 5118 (2000).
16. C. M. Bender and S. A. Orszag, *Advanced Mathematical Methods for Scientists and Engineers* (McGraw-Hill, New York, 1978), p. 484.
17. S. W. Haan, *Phys. Rev. A, Gen. Phys.* **39**, 5812 (1989).
18. R. Epstein, *Phys. Plasmas* **11**, 5114 (2004).
19. P. Amendt *et al.*, *Phys. Plasmas* **10**, 820 (2003).

---

## Publications and Conference Presentations

---

### Publications

---

- V. Bagnoud, "A Front End for Multipetawatt Lasers Based on a High-Energy, High-Average-Power Optical Parametric Chirped-Pulsed Amplifier," in *Frontiers in Optics 2004* (Optical Society of America, Rochester, NY, 2004), Paper FMM2.
- V. Bagnoud, M. J. Guardalben, J. Puth, J. D. Zuegel, T. Mooney, and P. Dumas, "High-Energy, High-Average-Power Laser with Nd:YLF Rods Corrected by Magnetorheological Finishing," *Appl. Opt.* **44**, 282 (2005).
- R. Betti, K. Anderson, J. Knauer, T. J. B. Collins, R. L. McCrory, P. W. McKenty, and S. Skupsky, "Theory of Laser-Induced Adiabatic Shaping in Inertial Confinement Fusion Implosions: The Relaxation Method," *Phys. Plasmas* **12**, 042703 (2005).
- C. Bouvier, J. C. Lambropoulos, and S. D. Jacobs, "Fracture Toughness of ULE, Zerodur, Astrosital and Corning 9600," in *Frontiers in Optics 2004*, OSA Technical Digest (Optical Society of America, Rochester, NY, 2004), Paper OTuA4.
- J. Carpenter and S. D. Jacobs, "In the Mood for Science," SPIE's *oemagazine*, March 2005, 35.
- J. E. DeGroote, S. N. Shafir, J. C. Lambropoulos, and S. D. Jacobs, "Surface Characterization of CVD ZnS Using Power Spectral Density," in *Frontiers in Optics 2004*, OSA Technical Digest (Optical Society of America, Rochester, NY, 2004), Paper OTuC2.
- V. Yu. Glebov, C. Stoeckl, T. C. Sangster, S. Roberts, R. A. Lerche, and G. J. Schmid, "NIF Neutron Bang Time Detector Prototype Test on OMEGA," *IEEE Trans. Plasma Sci.* **33**, 70 (2005).
- J. E. Goldston, E. Quataert, and I. V. Igumenshchev, "Synchrotron Radiation from Radiatively Inefficient Accretion Flow Simulations: Applications to Sagittarius A\*," *Astrophys. J.* **621**, 785 (2005).
- G. N. Gol'tsman, A. Korneev, I. Rubtsova, I. Milostnaya, G. Chulkova, O. Minaeva, K. Smirnov, B. Voronov, W. Slysz, A. Pearlman, A. Verevkin, and R. Sobolewski, "Ultrafast Superconducting Single-Photon Detectors for Near-Infrared-Wavelength Quantum Communications," *Phys. Stat. Sol. C* **2**, 1480 (2005).
- P. A. Jaanimagi, R. Boni, D. Butler, S. Ghosh, W. R. Donaldson, and R. L. Keck, "The Streak Camera Development Program at LLE," in the *26th International Congress on High-Speed Photography and Photonics*, edited by D. L. Paisley, S. Kleinfelder, D. R. Snyder, and B. J. Thompson (SPIE, Bellingham, WA, 2005), Vol. 5580, pp. 408–415.
- S. D. Jacobs, "Innovations in Optics Manufacturing," in *Frontiers in Optics 2004*, OSA Technical Digest (Optical Society of America, Rochester, NY, 2004), Paper OMA1.
- J. Keck, J. B. Oliver, V. Gruschow, J. Spaulding, and J. Howe, "Process Tuning of Silica Thin-Film Deposition," in *Frontiers in Optics 2004*, OSA Technical Digest (Optical Society of America, Rochester, NY, 2004), Paper OMB4.
- T. Z. Kosc, K. L. Marshall, A. Trajkovska-Petkoska, E. Kimball, and S. D. Jacobs, "Progress in the Development of Polymer Cholesteric Liquid Crystal Flakes for Display Applications," *Displays* **25**, 171 (2004).
- I. A. Kozhinova, H. J. Romanofsky, S. D. Jacobs, W. I. Kordonski, and S. R. Gorodkin, "Polishing of Pre-Polished CVD ZnS Flats with Altered Magnetorheological (MR) Fluids," in *Frontiers in Optics 2004*, OSA Technical Digest (Optical Society of America, Rochester, NY, 2004), Paper OMD2.

V. A. Smalyuk, V. N. Goncharov, T. R. Boehly, J. A. Delettrez, D. Y. Li, J. A. Marozas, D. D. Meyerhofer, S. P. Regan, and T. C. Sangster, "Angular Dependence of Imprinting Levels in Laser-Target Interactions on Planar CH Foils," to be published in *Physics of Plasmas*.

Y. Wang and H. Yang, "Synthesis of CoPt Nanorods in Ionic Liquids," to be published in the *Journal of the American Chemical Society*.

D. Wang, A. Verevkin, R. Sobolewski, R. Adam, A. van der Hart, and R. Franchy, "Magneto-Optical Kerr Effect Measurements and Ultrafast Coherent Spin Dynamics in Co Nano-Dots," to be published in *IEEE Transactions on Nanotechnology*.

---

### Conference Presentations

---

H. L. Helfer, "The Dark Matter of Galactic Halos," 205th Meeting of the American Astronomical Society, San Diego, CA, 9–13 January 2005.

R. Betti, K. Anderson, J. P. Knauer, and V. N. Goncharov, "Hydrodynamics of Inertial Confinement Fusion Implosions: What's Next?" 25th International Workshop on Physics of High Density in Matter, Hirschegg, Austria, 30 January–4 February 2005.

K. L. Marshall, T. Z. Kosc, A. Trajkovska-Petkoska, E. Kimball, and S. D. Jacobs, "Polymer Cholesteric Liquid Crystal (PCLC) Flake/Fluid Host Electro-Optic Suspensions and Their Applications in Flexible Reflective Displays," 4th Annual Flexible Microelectronics and Displays Conference, Phoenix, AZ, 1–3 February 2005.

P. B. Radha, "Direct-Drive Inertial Confinement Fusion: Status and Future," AAAS Annual Meeting, Washington, DC, 17–21 February 2005.

The following presentations were made at JOWOG 37, Albuquerque, NM, 21–25 February 2005:

D. D. Meyerhofer, B. Yaakobi, T. R. Boehly, T. J. B. Collins, H. Lorenzana, B. A. Remington, P. G. Allen, S. M. Pollaine, J. J. Rehr, and R. C. Albers, "Dynamic EXAFS Probing of Laser-Driven Shock Waves and Crystal Phase Transformations."

T. C. Sangster, T. R. Boehly, D. D. Meyerhofer, T. J. B. Collins, P. M. Celliers, G. W. Collins, J. H. Eggert, and D. G. Hicks, "Recent Results from EOS Experiments of Low-Density Foams and D<sub>2</sub>."

R. L. McCrory, D. D. Meyerhofer, S. J. Loucks, S. Skupsky, J. M. Soures, R. Betti, T. R. Boehly, M. J. Bonino, R. S. Craxton, T. J. B. Collins, J. A. Delettrez, D. H. Edgell, R. Epstein, V. Yu. Glebov, V. N. Goncharov, D. R. Harding, R. L. Keck, J. H. Kelly, J. P. Knauer, L. D. Lund, D. Jacobs-Perkins, J. R. Marciante, J. A. Marozas, F. J. Marshall, A. V. Maximov, P. W. McKenty, S. F. B. Morse, J. Myatt, S. G. Noyes, P. B. Radha, T. C. Sangster, W. Seka, V. A. Smalyuk, C. Stoeckl, K. A. Thorp, M. D. Wittman, B. Yaakobi, J. D. Zuegel, K. A. Fletcher, C. Freeman, S. Padalino, J. A. Frenje, C. K. Li, R. D. Petrasso, and F. H. Séguin, "Direct-Drive Inertial Confinement Fusion Research at the Laboratory for Laser Energetics," 6th Symposium on Current Trends in International Fusion Research: A Review, Washington, DC, 7–11 March 2005.

- A. P. Küng, A. Agarwal, D. F. Grosz, S. Banerjee, and D. N. Maywar, "Analytical Solution of Transmission Performance Improvement in Fiber Spans With Forward Raman Gain and Its Application to Repeaterless Systems," *J. Lightwave Technol.* **23**, 1182 (2005).
- S. Kurebayashi, J. A. Frenje, F. H. Séguin, J. R. Rygg, C. K. Li, R. D. Petrasso, V. Yu. Glebov, J. A. Delettrez, T. C. Sangster, D. D. Meyerhofer, C. Stoeckl, J. M. Soures, P. A. Amendt, S. P. Hatchett, and R. E. Turner, "Using Nuclear Data and Monte Carlo Techniques to Study Areal Density and Mix in  $D_2$  Implosions," *Phys. Plasmas* **12**, 032703 (2005).
- J. C. Lambropoulos and R. Varshneya, "Glass Material Response to the Fabrication Process: Example from Lapping," in *Frontiers in Optics 2004*, OSA Technical Digest (Optical Society of America, Rochester, NY, 2004), Paper OTuA1.
- J. R. Marciante, J. I. Hirsh, D. H. Raguin, and E. T. Prince, "Polarization-Insensitive, High-Dispersion TIR Diffraction Gratings," in *Frontiers in Optics 2004*, OSA Technical Digest (Optical Society of America, Rochester, NY, 2004), Paper DMA1.
- J. R. Marciante, J. I. Hirsh, D. H. Raguin, and E. T. Prince, "Polarization-Insensitive High-Dispersion Total Internal Reflection Diffraction Gratings," *J. Opt. Soc. Am. A* **22**, 299 (2005).
- A. E. Marino, K. Spencer, J. E. DeGroot, and S. D. Jacobs, "Chemical Durability of Phosphate Laser Glasses," in *Frontiers in Optics 2004*, OSA Technical Digest (Optical Society of America, Rochester, NY, 2004), Paper OTuA7.
- M. J. Moran, V. Yu. Glebov, C. Stoeckl, R. Rygg, and B.-E. Schwartz, "PROTEX: A Proton-Recoil Detector for Inertial Confinement Fusion Neutrons," *Rev. Sci. Instrum.* **76**, 023506 (2005).
- F. H. Mrakovcic, J. A. Randi, J. C. Lambropoulos, and S. D. Jacobs, "Subsurface Damage in Single-Crystal Sapphire," in *Frontiers in Optics 2004* (Optical Society of America, Rochester, NY, 2004), Paper OTuA6.
- J. B. Oliver, "Thin-Film-Optics Design and Manufacturing Challenges for Large-Aperture High-Peak-Power, Short-Pulse Lasers," in *Frontiers in Optics 2004* (Optical Society of America, Rochester, NY, 2004), Paper OMB1.
- S. Papernov and A. W. Schmid, "High-Spatial-Resolution Studies of UV-Laser-Damage Morphology in  $SiO_2$  Thin Films with Artificial Defects," in *Laser-Induced Damage in Optical Materials: 2004*, edited by G. J. Exarhos, A. H. Guenther, N. Kaiser, K. L. Lewis, M. J. Soileau, and C. J. Stolz (SPIE, Bellingham, WA, 2005), Vol. 5647, pp. 141–155.
- P. B. Radha, V. N. Goncharov, T. J. B. Collins, J. A. Delettrez, Y. Elbaz, V. Yu. Glebov, R. L. Keck, D. E. Keller, J. P. Knauer, J. A. Marozas, F. J. Marshall, P. W. McKenty, D. D. Meyerhofer, S. P. Regan, T. C. Sangster, D. Shvarts, S. Skupsky, Y. Srebro, R. P. J. Town, and C. Stoeckl, "Two-Dimensional Simulations of Plastic-Shell, Direct-Drive Implosions on OMEGA," *Phys. Plasmas* **12**, 032702 (2005).
- R. Rey-de-Castro, D. Wang, A. Verevkin, A. Mycielski, and R. Sobolewski, " $Cd_{1-x}Mn_xTe$  Semimagnetic Semiconductors for Ultrafast Spintronics and Magneto-optics," *IEEE Trans. Nanotech.* **4**, 106 (2005).
- A. Rigatti, "Cleaning Process Versus Laser Damage Threshold of Coated Optical Components," in *Frontiers in Optics 2004* (Optical Society of America, Rochester, NY, 2004), Paper OMB3.
- A. L. Rigatti, "Cleaning Process Versus Laser-Damage Threshold of Coated Optical Components," in *Laser-Induced Damage in Optical Materials: 2004*, edited by G. J. Exarhos, A. H. Guenther, N. Kaiser, K. L. Lewis, M. J. Soileau, and C. J. Stolz (SPIE, Bellingham, WA, 2005), Vol. 5647, pp. 136–140.
- J. Sanz and R. Betti, "Analytical Model of the Ablative Rayleigh–Taylor Instability in the Deceleration Phase," *Phys. Plasmas* **12**, 042704 (2005).
- S. N. Shafirir, J. C. Lambropoulos, and S. D. Jacobs, "Loose Abrasive Lapping of Optical Glass with Different Lapping Plates and Its Interpretation," in *Frontiers in Optics 2004* (Optical Society of America, Rochester, NY, 2004), Paper OMC4.
- A. Trajkovska-Petkoska, R. Varshneya, T. Z. Kosc, K. L. Marshall, and S. D. Jacobs, "Enhanced Electro-Optic Behavior for Shaped Polymer Cholesteric Liquid-Crystal Flakes Made Using Soft Lithography," *Adv. Funct. Mater.* **15**, 217 (2005).

N. G. Usechak and G. P. Agrawal, "Semi-Analytic Technique for Analyzing Mode-Locked Lasers," *Opt. Express* **13**, 2075 (2005).

T. Yasuda, K. Fujita, T. Tsutsui, Y. Geng, S. W. Culligan, and S. H. Chen, "Carrier Transport Properties of Monodisperse Glassy-Nematic Oligofluorenes in Organic Field-Effect Transistors," *Chem. Mater.* **17**, 264 (2005).

J. D. Zuegel, V. Bagnoud, T. Corso, P. Drew, G. J. Quarles, P. Dumas, J. T. Mooney, and S. D. O'Donohue, "Wavefront Correction Extends the Capabilities of Large-Aperture Nd:YLF Laser Rods," *Laser Focus World* **41**, 133 (2005).

### Forthcoming Publications

V. Bagnoud, I. A. Begishev, M. J. Guardalben, J. Puth, and J. D. Zuegel, "A 5-Hz, 250-mJ Optical Parametric Chirped-Pulse Amplifier at 1053 nm with New Ideal Performance," to be published in *Optics Letters*.

D. Clay, D. Poslunsky, M. Flinders, S. D. Jacobs, and R. Cutler, "Effect of  $\text{LiAl}_5\text{O}_8$  Additions on the Sintering and Optical Transparency of LiAlON," to be published in the *Journal of European Ceramic Society*.

T. J. B. Collins, A. Poludnenko, A. Cunningham, and A. Frank, "Shock Propagation in Deuterium-Tritium-Saturated Foam," to be published in *Physics of Plasmas*.

S. Costea, S. Pisana, N. P. Kherani, F. Gaspari, T. Koteski, W. T. Shmayda, and S. Zukotynski, "The Use of Tritium in the Study of Defects in Amorphous Silicon," to be published in the *Journal of Fusion Science and Technology*.

R. S. Craxton and D. W. Jacobs-Perkins, "The Saturn Target for Polar Direct Drive on the National Ignition Facility," to be published in *Physical Review Letters*.

R. S. Craxton, F. J. Marshall, M. J. Bonino, R. Epstein, P. W. McKenty, S. Skupsky, J. A. Delettrez, I. V. Igumenshchev, D. W. Jacobs-Perkins, J. P. Knauer, J. A. Marozas, P. B. Radha, and W. Seka, "Polar Direct Drive: Proof-of-Principle Experiments on OMEGA and Prospects for Ignition on the National Ignition Facility," to be published in *Physics of Plasmas* (invited).

V. N. Goncharov and D. Li, "Effects of Temporal Density Variation and Convergent Geometry on Nonlinear Bubble in Classical Rayleigh-Taylor Instability," to be published in *Physical Review E*.

L. Guazzotto, R. Betti, J. Manickam, S. Kaye, and J. L. Gauvreau, "Magnetohydrodynamics Equilibria with Toroidal and Poloidal Flow," to be published in *Physics of Plasmas* (invited).

D. R. Harding, F.-Y. Tsai, E. L. Alfonso, S. H. Chen, A. K. Knight, and T. N. Blanton, "Properties of Vapor-Deposited Polyimide Films," to be published in the *Journal of Adhesion Science and Technology* (invited).

J. Kitaygorsky, J. Zhang, A. Verevkin, A. Sergeev, A. Korneev, V. Matvienko, P. Kouminov, K. Smirnov, B. Voronov, G. Gol'tsman, and R. Sobolewski, "Origin of Dark Counts in Nanostructured NbN Single-Photon Detectors," to be published in *IEEE Transactions on Applied Superconductivity*.

J. P. Knauer, K. Anderson, P. B. Radha, R. Betti, T. J. B. Collins, V. N. Goncharov, P. W. McKenty, D. D. Meyerhofer, S. P. Regan, T. C. Sangster, and V. A. Smalyuk, "Improved Target Stability Using Picket Pulses to Increase and Shape the Ablator Adiat," to be published in *Physics of Plasmas* (invited).

A. Korneev, V. Matvienko, O. Minaeva, I. Milostnaya, I. Rubtsova, G. Chulkova, K. Smirnov, V. Voronov, G. Gol'tsman, W. Slysz, A. Pearlman, A. Verevkin, and R. Sobolewski, "Quantum Efficiency and Noise Equivalent Power of Nanostructured, NbN, Single-Photon Detectors in the Wavelength Range from Visible to Infrared," to be published in *IEEE Transactions on Applied Superconductivity*.

T. Koteski, N. P. Kherani, W. T. Shmayda, S. Costea, and S. Zukotynski, "Nuclear Batteries Using Tritium and Thin-Film Hydrogenated Amorphous Silicon," to be published in the *Journal of Fusion Science and Technology*.

I. A. Kozhinova, H. J. Romanofsky, A. Maltsev, S. D. Jacobs, W. I. Kordonski, and S. R. Gorodkin, "Minimizing Artifact Formation in Magnetorheological Finishing of CVD ZnS Flats," to be published in *Applied Optics*.

X. Li, Y. Xu, S. Chromik, V. Strbík, P. Odier, D. De Barros, and R. Sobolewski, "Time-Resolved Carrier Dynamics in Hg-Based High-Temperature Superconducting Photodetectors," to be published in *IEEE Transactions on Applied Superconductivity*.

A. E. Marino, K. E. Spencer, J. E. DeGroot, K. L. Marshall, A. L. Rigatti, and S. D. Jacobs, "Chemical Durability of Phosphate Laser Glasses Polished with Pitch, Pads, or MRF," to be published in *Applied Optics*.

F. J. Marshall, R. S. Craxton, J. A. Delettrez, D. H. Edgell, L. M. Elasky, R. Epstein, V. Yu. Glebov, V. N. Goncharov, D. R. Harding, R. Janezic, R. L. Keck, J. D. Kilkenny, J. P. Knauer, S. J. Loucks, L. D. Lund, R. L. McCrory, P. W. McKenty, D. D. Meyerhofer, P. B. Radha, S. P. Regan, T. C. Sangster, W. Seka, V. A. Smalyuk, J. M. Soures, C. Stoeckl, S. Skupsky, J. A. Frenje, C. K. Li, R. D. Petrasso, and F. H. Séguin, "Direct-Drive, Cryogenic Target Implosions on OMEGA," to be published in *Physics of Plasmas* (invited).

R. L. McCrory, S. P. Regan, R. Betti, T. R. Boehly, R. S. Craxton, T. J. B. Collins, J. A. Delettrez, R. Epstein, V. Yu. Glebov, V. N. Goncharov, D. R. Harding, R. L. Keck, J. P. Knauer, S. J. Loucks, J. Marciante, J. A. Marozas, F. J. Marshall, A. Maximov, P. W. McKenty, D. D. Meyerhofer, J. Myatt, P. B. Radha, T. C. Sangster, W. Seka, S. Skupsky, V. A. Smalyuk, J. M. Soures, C. Stoeckl, B. Yaakobi, J. D. Zuegel, C. K. Li, R. D. Petrasso, F. H. Séguin, J. A. Frenje, S. Padalino, C. Freeman, and K. Fletcher, "Direct-Drive Inertial Confinement Fusion Research at the Laboratory for Laser Energetics: Charting the Path to Thermonuclear Ignition," to be published in *Nuclear Fusion*.

J.-R. Park, W. R. Donaldson, and R. Sobolewski, "Time-Resolved Imaging of a Spatially Modulated Laser Pulse," to be published in *SPIE's Proceedings of LASE 2004*.

S. Papernov and A. W. Schmid, "Two Mechanisms of Crater Formation in Ultraviolet-Pulsed, Laser-Irradiated SiO<sub>2</sub> Thin Films with Artificial Defects," to be published in the *Journal of Applied Physics*.

A. Pearlman, A. Cross, W. SBysz, J. Zhang, A. Verevkin, M. Currie, A. Korneev, P. Kouminov, K. Smirnov, B. Voronov, G. Gol'tsman, and R. Sobolewski, "Gigahertz Counting Rates of NbN Single-Photon Detectors for Quantum Communications," to be published in *IEEE Transactions on Applied Superconductivity*.

P. B. Radha, T. J. B. Collins, J. A. Delettrez, Y. Elbaz, R. Epstein, V. Yu. Glebov, V. N. Goncharov, R. L. Keck, J. P. Knauer, J. A. Marozas, F. J. Marshall, R. L. McCrory, P. W. McKenty, D. D. Meyerhofer, S. P. Regan, T. C. Sangster, W. Seka, D. Shvarts, S. Skupsky, Y. Srebro, and C. Stoeckl, "Multidimensional Analysis of Direct-Drive Plastic-Shell Implosions on OMEGA," to be published in *Physics of Plasmas* (invited).

J. A. Randi, J. C. Lambropoulos, and S. D. Jacobs, "Subsurface Damage in Single Crystalline Optical Materials," to be published in *Applied Optics*.

S. P. Regan, J. A. Marozas, R. S. Craxton, J. H. Kelly, W. R. Donaldson, P. A. Jaanimagi, D. Jacobs-Perkins, R. L. Keck, T. J. Kessler, D. D. Meyerhofer, T. C. Sangster, W. Seka, V. A. Smalyuk, S. Skupsky, and J. D. Zuegel, "Performance of a 1-THz-Bandwidth, 2-D Smoothing by Spectral Dispersion and Polarization Smoothing of High-Power, Solid-State Laser Beams," to be published in the *Journal of the Optical Society of America B*.

S. P. Regan, T. C. Sangster, D. D. Meyerhofer, K. Anderson, R. Betti, T. R. Boehly, T. J. B. Collins, R. S. Craxton, J. A. Delettrez, R. Epstein, O. V. Gotchev, V. Yu. Glebov, V. N. Goncharov, D. R. Harding, P. A. Jaanimagi, J. P. Knauer, S. J. Loucks, L. D. Lund, J. A. Marozas, F. J. Marshall, R. L. McCrory, P. W. McKenty, S. F. B. Morse, P. B. Radha, W. Seka, S. Skupsky, H. Sawada, V. A. Smalyuk, J. M. Soures, C. Stoeckl, B. Yaakobi, J. A. Frenje, C. K. Li, R. D. Petrasso, and F. H. Séguin, "Direct-Drive Inertial Confinement Fusion Implosions on OMEGA," to be published in *Astrophysics and Space Science*.

V. A. Smalyuk, J. A. Delettrez, S. B. Dumanis, R. Epstein, V. Yu. Glebov, D. D. Meyerhofer, P. B. Radha, T. C. Sangster, C. Stoeckl, N. C. Toscano, J. A. Frenje, C. K. Li, R. D. Petrasso, F. H. Séguin, and J. H. Koch, "Hot-Core Characterization of the Cryogenic D<sub>2</sub> Target at Peak Neutron Production in Direct-Drive Spherical Implosion," to be published in *Physics of Plasmas*.

V. A. Smalyuk, V. N. Goncharov, T. R. Boehly, J. A. Delettrez, D. Y. Li, J. A. Marozas, D. D. Meyerhofer, S. P. Regan, and T. C. Sangster, "Angular Dependence of Imprinting Levels in Laser-Target Interactions on Planar CH Foils," to be published in *Physics of Plasmas*.

Y. Wang and H. Yang, "Synthesis of CoPt Nanorods in Ionic Liquids," to be published in the *Journal of the American Chemical Society*.

D. Wang, A. Verevkin, R. Sobolewski, R. Adam, A. van der Hart, and R. Franchy, "Magneto-Optical Kerr Effect Measurements and Ultrafast Coherent Spin Dynamics in Co Nano-Dots," to be published in *IEEE Transactions on Nanotechnology*.

---

### Conference Presentations

---

H. L. Helfer, "The Dark Matter of Galactic Halos," 205th Meeting of the American Astronomical Society, San Diego, CA, 9–13 January 2005.

R. Betti, K. Anderson, J. P. Knauer, and V. N. Goncharov, "Hydrodynamics of Inertial Confinement Fusion Implosions: What's Next?" 25th International Workshop on Physics of High Density in Matter, Hirschegg, Austria, 30 January–4 February 2005.

K. L. Marshall, T. Z. Kosc, A. Trajkovska-Petkoska, E. Kimball, and S. D. Jacobs, "Polymer Cholesteric Liquid Crystal (PCLC) Flake/Fluid Host Electro-Optic Suspensions and Their Applications in Flexible Reflective Displays," 4th Annual Flexible Microelectronics and Displays Conference, Phoenix, AZ, 1–3 February 2005.

P. B. Radha, "Direct-Drive Inertial Confinement Fusion: Status and Future," AAAS Annual Meeting, Washington, DC, 17–21 February 2005.

The following presentations were made at JOWOG 37, Albuquerque, NM, 21–25 February 2005:

D. D. Meyerhofer, B. Yaakobi, T. R. Boehly, T. J. B. Collins, H. Lorenzana, B. A. Remington, P. G. Allen, S. M. Pollaine, J. J. Rehr, and R. C. Albers, "Dynamic EXAFS Probing of Laser-Driven Shock Waves and Crystal Phase Transformations."

T. C. Sangster, T. R. Boehly, D. D. Meyerhofer, T. J. B. Collins, P. M. Celliers, G. W. Collins, J. H. Eggert, and D. G. Hicks, "Recent Results from EOS Experiments of Low-Density Foams and D<sub>2</sub>."

R. L. McCrory, D. D. Meyerhofer, S. J. Loucks, S. Skupsky, J. M. Soures, R. Betti, T. R. Boehly, M. J. Bonino, R. S. Craxton, T. J. B. Collins, J. A. Delettrez, D. H. Edgell, R. Epstein, V. Yu. Glebov, V. N. Goncharov, D. R. Harding, R. L. Keck, J. H. Kelly, J. P. Knauer, L. D. Lund, D. Jacobs-Perkins, J. R. Marciante, J. A. Marozas, F. J. Marshall, A. V. Maximov, P. W. McKenty, S. F. B. Morse, J. Myatt, S. G. Noyes, P. B. Radha, T. C. Sangster, W. Seka, V. A. Smalyuk, C. Stoeckl, K. A. Thorp, M. D. Wittman, B. Yaakobi, J. D. Zuegel, K. A. Fletcher, C. Freeman, S. Padalino, J. A. Frenje, C. K. Li, R. D. Petrasso, and F. H. Séguin, "Direct-Drive Inertial Confinement Fusion Research at the Laboratory for Laser Energetics," 6th Symposium on Current Trends in International Fusion Research: A Review, Washington, DC, 7–11 March 2005.

UNIVERSITY OF  
ROCHESTER